Summer 2014

Early targeting of knee osteoarthritis : validation of computational methods

Tyler Joseph Stockman
University of Iowa

EARLY TARGETING OF KNEE OSTEOARTHRITIS:

VALIDATION OF COMPUTATIONAL METHODS

by

Tyler Joseph Stockman

A thesis submitted in partial fulfillment of
the requirements for the Master of Science
degree in Biomedical Engineering in the
Graduate College of
The University of Iowa

August 2014

Thesis Supervisor: Associate Professor Donald D. Anderson

Graduate College The
University of Iowa
Iowa City, Iowa

CERTIFICATE OF APPROVAL

MASTER'S THESIS

This is to certify that the Master's thesis of

Tyler Joseph Stockman

has been approved by the Examining Committee
for the thesis requirement for the Master of Science
degree in Biomedical Engineering at the August 2014 graduation.

Thesis Committee: _____
Donald D. Anderson, Thesis Supervisor

_____
Neil A. Segal

_____
Thomas Brown

ACKNOWLEDGMENTS

I would first and foremost like to thank my research supervisors Drs. Don Anderson and Neil Segal for their guidance during my time in the Orthopaedic Biomechanics Laboratory. Dr. Anderson's expertise and encouragement from both engineering and personal perspectives were crucial to my development as a graduate-level researcher, and provided direction during the development of my projects. Dr. Segal very kindly provided me with the opportunity to collaborate on a project for which we share a common interest. Furthermore he provided funding for my research through an Innovative Research Grant from the Arthritis Foundation (#18341800), and provided invaluable clinical perspectives during the development of my research.

Furthermore, I would like to extend my thanks to the members of the Orthopedic Biomechanics Lab, as many were involved with my orientation to lab procedure, education in the use of biomechanical technologies, and project development through constructive feedback. Special thanks to Andrew Kern for guidance in understanding and developing the registration and DEA algorithms, as well as continued coding assistance for a (previously) infrequent programmer. The work reported in this thesis builds upon precedent work in the University of Iowa Orthopedic Biomechanics Laboratory. The groundwork with which our group has been able to produce 3D model-to-2D image (hereafter referred to as 3D-2D) registrations and compute contact stress estimates using DEA for first the ankle and later the knee, was put in place by Andrew during his time as an M.S. research assistant in the lab. Thank you as well to Dr. Jessica Goetz for her valuable feedback regarding data presentation, and Mariah Bankert for model segmentation performed.

Finally, I would like to thank my family and fiancée for supporting me in whatever academic pursuit I should choose, and for teaching me the value of perseverance.

TABLE OF CONTENTS

LIST OF TABLES

LIST OF FIGURES

CHAPTER 1: INTRODUCTION AND BACKGROUND

1.1 Osteoarthritis and its Significance

Osteoarthritis (OA) is a disease of the joints manifested through degeneration of articular cartilage and the underlying bone structure. Such degradation has effects on the joint as a whole, often expressed as pain, stiffness and swelling. This debilitating disease currently reigns as the most prevalent among the world's populations, with symptomatic prevalence rates of 6% in the knee and 3% in the hip among adults age 30 or older. As of 2000, costs associated with arthritis as a whole were thought to have surpassed 2% of the GDP. By the year 2030, the disease is projected to affect nearly 9.3% of the US adult population. [1]

Pathological features of OA include the loss of articular cartilage, the development of osteophytes, other changes in bone structure, and joint inflammation. Diagnosis of symptomatic OA generally corresponds to reports of pain due to progression of these pathologies. [2, 3] Specific non-mechanical risk factors that are associated with the onset of OA involve an individual's nutrition and levels of oxidants and certain vitamins, as well as genetic predisposition to the disease. There are a host of biomechanical risk factors. Acute joint deformity, aberrant articular cartilage loading, sports participation, and occupational factors all contribute to the risk for OA onset. A demonstration of the interrelation of these biomechanical factors can be seen through the effect of knee alignment on OA progression. For example, excessive varus or valgus alignment of the knee can affect the contact area and load through the condyles, which can in turn affect cartilage structure and result in more excessive varus or valgus bone alignment. [4]

1.2 Anatomy of the Knee

The knee is the weight-bearing joint most commonly affected by OA. The knee involves three bones, which interface at two distinct articulations, as well as its numerous

surrounding ligaments and supporting structures. In a joint such as the hip, the bony geometry provides the majority of the stability through its ball and socket configuration. In the knee, the articulation lacks the congruence seen in the hip, so the knee depends much more on the surrounding soft tissue and ligaments for stability. The bones constituting the knee are the femur, tibia, and patella. The tibia and femur articulate in the tibiofemoral joint, through which passes the majority of forces associated with standing, knee flexion, and bipedal locomotion. The patella lies in the patellar groove on the anterior aspect of the femur and articulates in the patellofemoral joint. This joint is loaded by virtue of forces developing in the patellar tendon. Stabilization and protection of the knee are provided by the patellofemoral articulation, and it is instrumental in extending the knee. [5]

In the tibiofemoral joint, the distal end of the femur articulates with the proximal end of the tibia in a bicondylar contact. The flattened proximal end of the tibia has two distinct plateaus identified as medial and lateral, lying on either side of the tibial spine. This separates the knee into two compartments, with the largest articular area in the medial compartment, through which passes a larger portion of knee load in healthy knees. [6] At the periphery of each of these plateaus sits a fibrocartilaginous c-shaped meniscus, stabilizing the knee mediolaterally and anteroposteriorly by holding the femoral condyles within its “cup” shape (Figure 1-1, images from Blackburn et al. 1980 and Golblatt et al. 2003). Each meniscus has a crescent shape when viewed superior to inferior, creating the “rim” of the cup. The ends of the menisci, known as horns, attach centrally near or on the tibial spine via ligaments. Movement in this joint is primarily rotation about the mediolateral axis as the knee flexes and extends, but the joint also has a rotational aspect as the knee moves to an extended position. [7]

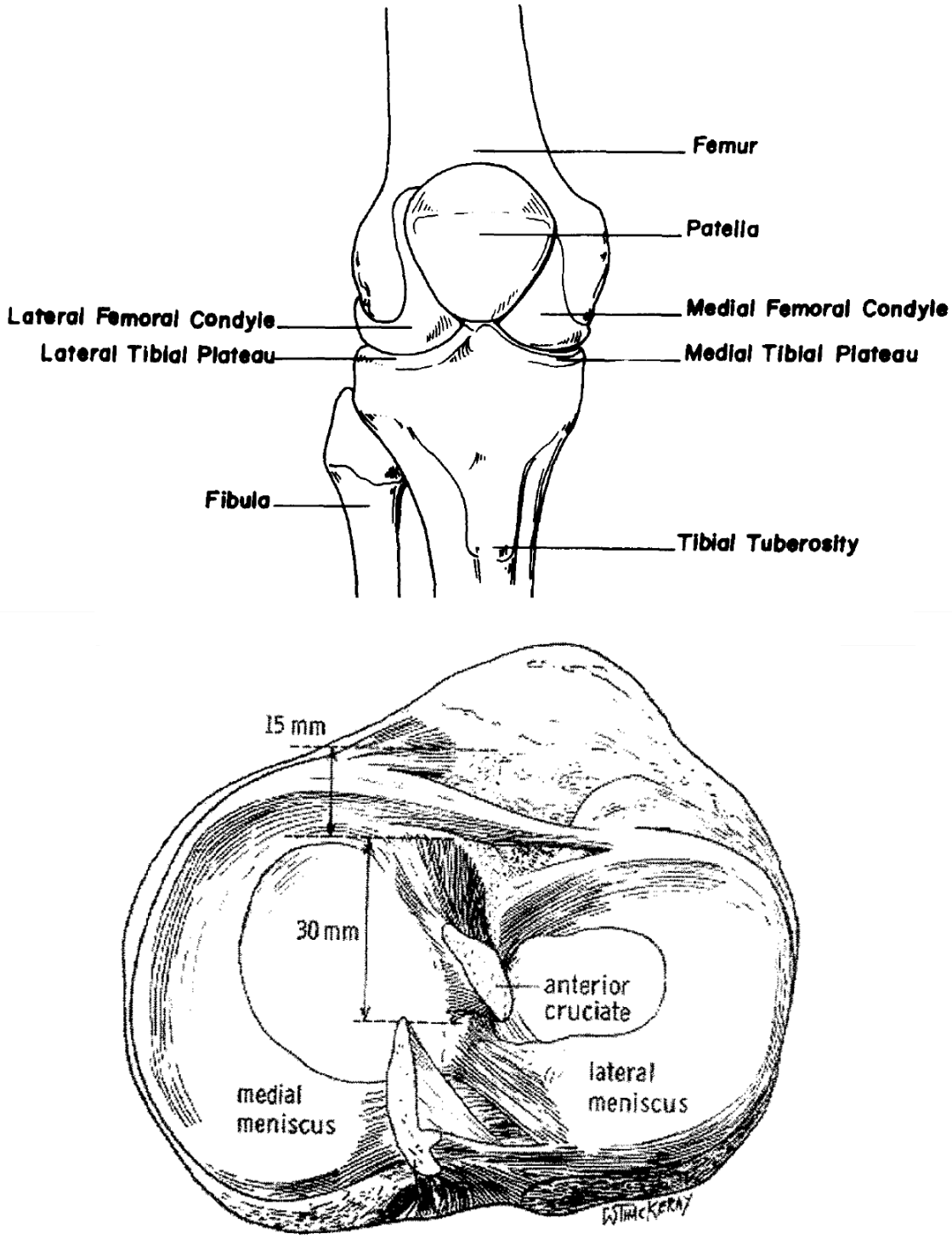

Figure 1-1 - Coronal plane view of the anterior knee and its structures (top), and transverse plane view of the tibial plateaus, menisci and attachment sites (bottom).

1.3 Knee OA and Contact Stress

1.3.1 Knee OA Risk Factors

The biomechanical factors relating to knee OA are a subject of considerable study. Knee OA is related to multiple biomechanical factors, all of which are complexly interrelated. These factors have been seen to produce varied effects on the structures of the knee. Generally, changes in joint loading and joint shape are manifested in cartilage degeneration and bone remodeling. This is indeed seen in cases where OA has been allowed to progress. An example of this lies in work linking bone marrow lesions (BMLs) to cartilage loss through altered bone shape and thus altered contact. [8] Segal et al. found a correlation between elevated tibiofemoral contact stress, BML development and cartilage loss. [8, 9] These associations align with another study reporting that 77.5% of subjects with BMLs reported knee pain. [10] Further work has indicated a strong relationship between osteophyte presence (a radiographic indicator of OA) and cartilage thickening in subjects with early radiographic OA. In that study, contralateral knees were also examined and found to have no similar increase in cartilage thickness. [11] Further changes to the structure of the joint, manifested as changes to the subchondral bone thickness, have been suggested as factors in developing OA. Though commonly seen along with the development of OA, no statistically significant trend was found to link subchondral bone thickness to knee OA directly. [12]

Focusing on a larger scale, many factors and scenarios are implicated in contact stress distribution variance. As previously mentioned, varus alignment in the human knee has been associated with increased OA progression in the medial compartment, just as valgus alignment has been shown to increase progression in the lateral compartment.[4] This is suspected to be due to shifting of the stress distribution in the knee. Furthermore, it was theorized that such alignments could result in a “vicious circle” in which alignment causes cartilage degradation, which in turn worsens alignment.[13] Another study

examined the relation of bone shape to the progression of knee OA, proposing that changes in bone shape can be used to track and predict progression. [14] Such a relationship could once again be described in terms of its effects on contact in the knee. Altered loading need not arise solely from injury, but is also seen through different flexion angles of the knee and different levels of knee resection. Not only are shifts in loading location present, but also contact area changes that directly influence stress levels. [15, 16] Brown & Shaw also mention the implications of altered loading in the onset and progression of OA. [17] Therefore it stands to reason that measurement of loading changes through various means could be definitively linked to OA onset and progression, as well as eventually provide a means for prevention.

1.3.2 Contact Stress in OA

Of the many biomechanical factors that contribute to OA onset and progression, it is quite reasonable to believe that contact stress in the knee might be used for OA risk prediction. In a longitudinal study conducted across multiple centers, baseline contact stress estimations obtained using a subject-specific computational modeling approach have been associated with onset of knee OA. Using this method to produce stress estimates on a subject-specific basis returned results that showed a 0.54±0.77 MPa higher peak stress value for knees that would later develop symptomatic OA. [18] Such findings warrant further study, as a link between elevated contact stress and OA onset and progression would provide a new metric for assessment and treatment of the disease.

1.3.3 Computational Stress Analysis Methods

1.3.3.1 Finite Element Analysis

In the realm of computational stress analysis in the human body, finite element analysis (FEA) has long been the standard. Introduced to the field of biomechanics in 1972, FEA revolutionized stress analysis in the human body. The complex shapes and

contacts of mechanical structures in the body can be defined as a set of elements in 2D or 3D, depending on the application. Particularly, stress analysis of musculoskeletal implants is performed, allowing companies to better design their products to avoid wear and improper joint articulation. This is one of the most common applications of FEA. [19, 20] Likewise, more and more research groups are currently pursuing viable ways to measure intra-articular contact stress in vivo. [21]

FEA modeling *for contact* can be considered as a series of interconnected nodes defined throughout the contact model. When one node is contacted, those in the vicinity deform in a manner that can be predicted based upon mathematical relationships prescribed by the material properties and element structure of the model. Such interconnection of calculations gives this type of modeling very comparable results with physical validations of the model. [22, 23] Patient-specific modeling is accomplished by applying a mesh to patient-specific models of biomechanical structures. Contemporary software has even been produced to make this meshing process easier, by providing a more hands-on system for defining the mesh. [24] FEA is also very useful where dynamic analysis is involved, as motion can be prescribed for bones comprising a joint, and complex boundary conditions can be established to constrain the model. [25] Although FEA is frequently used for contact applications, the interconnectivity of elements in a FE model allow for internal stress computation under complex loadings. This is a capability that cannot be utilized when employing simpler modeling techniques.

Using FEA to estimate contact stress in joints results in very accurate contact location and stress values, but its complexity limits the number of subjects that can be practically included in a study. The time devoted to meshing a model and in running the model are the primary factors in this respect. A large amount of manual computer time is required to produce a working finite element mesh, and the mesh may require further adjustment after initial runs. Such adjustments may be added to enhance mesh quality by fixing problem elements or further refining the mesh. [24]

1.3.3.2 Discrete Element Analysis

Discrete Element Analysis (DEA) provides an expeditious alternative to using FEA in articular joints, a class of problems for which reasonably accurate contact stress estimates may be obtained by treating the relatively thin layer of cartilage on bone as an elastically deformable material over a rigid substrate. Using 3D models of the bone and cartilage, cartilage deformation is computed based on the apparent overclosure of the articular surface models. Originally known as Rigid Body-Spring Modeling (RBSM), the DEA method is adapted from a civil engineering application. Using DEA, the collapse loading in beams of different materials, as well as deformation of underground tunnels could be computed accurately. [26, 27] One of the primary differences between FEA and DEA lies in the lack of interconnectivity of elements in DEA. DEA can be explained in simplified terms as a bed of springs that deform independently from one another. This type of modeling can be used effectively for analysis of the locations of the model that are in contact, but will not provide insight into how the surrounding areas are affected.

The ability of DEA to simplify the contact computations results in significant time savings and the ability to produce results for much larger subject sample sizes. Furthermore, *large numbers of patient-specific models* can be analyzed, limited primarily by the time required to manually generate bone models from MRI. Many groups have adopted DEA as a stress estimation method due to these benefits, and model complexity varies across these groups. The work done by Elias et al. to determine the patellofemoral contact pressure is indicative of these levels of complexity. That model uses the quadriceps and patellar tendon forces to press the patella against the PF groove at varying degrees of knee flexion. When validated using a cadaveric set-up, computational stress estimations were comparable to experimental values. [28] Likewise, Kwak, et al. have developed a model including muscle and ligament forces, and have completed validation work. [29] Li et al. were also able to produce similar results between FEA, DEA and

another stress analysis method known as simplified elasticity solution, reporting nearly identical stress distributions across these methods. [30]

Many studies that incorporate the ligaments surrounding the knee joint in their calculations afford a stability of the model not seen in others, while allowing more "settling" of the model into biomechanical equilibrium due to a fewer strictly constrained degrees of freedom. [31, 32] The meniscus is not always included in the DEA stress computation. Studies that attempt to model the meniscus are discussed later. It is known that the meniscus plays a part in load bearing, but is difficult to model in a DEA approach due to its higher translational mobility, whereas the articular cartilage-bone interfaces allow only for cartilage deformation that is more normal to the bone surface. [31] Shear has been implemented into a DEA model before, primarily for civil engineering applications, in which springs are essentially broken under enough shear and turned into smaller, more irregularly sized springs. [33]

It has been suggested that DEA, involving simpler calculations and reduced time cost, can eventually be used clinically, pre-operatively, and even intra-operatively to provide expedited contact stress feedback to surgeons and clinicians alike. [26, 28] Furthermore, DEA affords an unconditional numerical stability that is comparable to that of an explicit finite element solver. The robustness of the methodology produces results that will converge consistently. Use of an implicit finite element solver can result in an inability to converge on a solution for cases with more complex contact, something that is not seen using the simplified DEA model. The focus in this thesis is on the use of DEA to predict intra-articular contact stress in-vivo, and to pave the way for examining the relationship between these stresses and OA onset and progression.

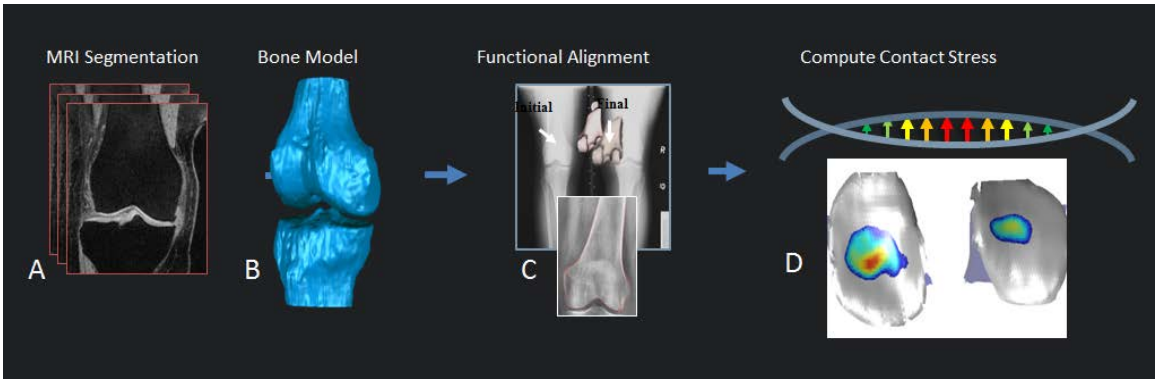

Figure 1-2 – Overview of the DEA process. This is a very simplified diagram describing the basic steps. First, slice by slice hand segmentation of MR images takes place (A). These slices are then used to produce a polygonal surface model in Geomagic (B). The bone model is then registered to a functional apposition provided by weight-bearing radiography (C). Lastly, contact stress is computed between the models given certain loading conditions (D).

1.4 DEA Implementation in Subject-Specific Modeling

The following explanation of the DEA implementation is simplified for the sake of brevity, but intended to give a reasonable overview to a reader not as familiar with the process of stress estimation in biomechanical models. For additional methodological detail, refer to Kern, A.M., 2011. [34]

1.4.1 Model Creation

To create a DEA model, the relevant anatomical structures for a subject are modeled from manual MRI segmentations obtained using OsiriX software (The OsiriX Foundation, Geneva, Switzerland) [35]. After exporting segmentations for each region of interest from OsiriX, point clouds are generated using MATLAB software (Mathworks) and imported to Geomagic (Geomagic, Inc.) for conversion to polygonal surface models. [36, 37] Using semi-automated segmentation algorithms, bone models have been efficiently segmented from CT with minimal user input. The intensity of bone in CT provides a distinct threshold for each subject that allows for discerning bone surfaces. Although this drastically reduces the time needed for bone model generation, CT

currently lacks the soft tissue resolution to accurately define cartilage and meniscus structures. MRI is still the standard for imaging soft tissues.

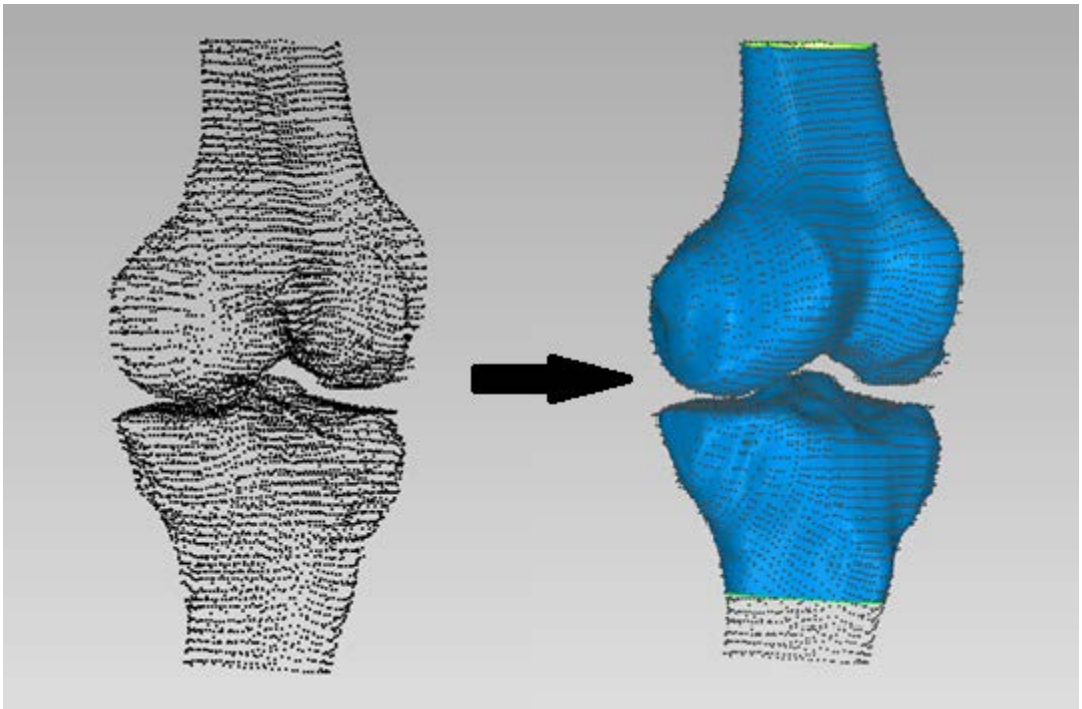

Figure 1-3 – Depiction of polygonal surface model creation from point cloud.

1.4.2 3D-2D Registration

Once models have been generated for the bones of the knee joint, they must be registered to a functional pose. This is because acquisition of the MR image is performed with the knee in a relaxed, semi-flexed position that is provided by a ~20° triangular wedge placed under the knee. In order to produce the most accurate stress estimation, the bone models must be aligned to a loaded apposition. This loaded apposition of the knee is at around 20° of knee flexion based on clinical standards used to radiographically determine joint space width in patients with OA, falling in the commonly accepted range of 15-20°. This range generally provides an optimum view of the joint space, and the

view can be adjusted based on radiographic source positioning. [38] After obtaining a 2D lateral and PA radiograph of the subject's knee in a functional pose, 3D bone models can be aligned to the functional pose in the radiograph by optimizing the alignment of a projective silhouette of the bone model to the bone shape depicted in the radiograph. This bone shape can be defined in a number of ways. In some cases, it is necessary to provide an edge tracing of the bone, which is produced in a semi-automated fashion, to assist in registration. This input guides the model to a user-defined bone edge selected from a binary image produced through Canny edge detection. [39-42] More recently, a gradient-based approach has been implemented that does not require edge tracings, but may still benefit from them. In this approach a gradient image is created from the radiograph to discern boundaries between bone and soft tissue. A gradient value for each pixel is first computed across the width (X) and down the height (Y) of the image. Next, the absolute value is taken to treat all gradients as positive, and the two gradient images are added together. The resulting image is a combination of the maximum X and Y gradients, especially highlighting edges that stand out in both directions. Essentially, these automated edge tracings have the same effect on registration, but require no manual user input. [39, 42, 43]

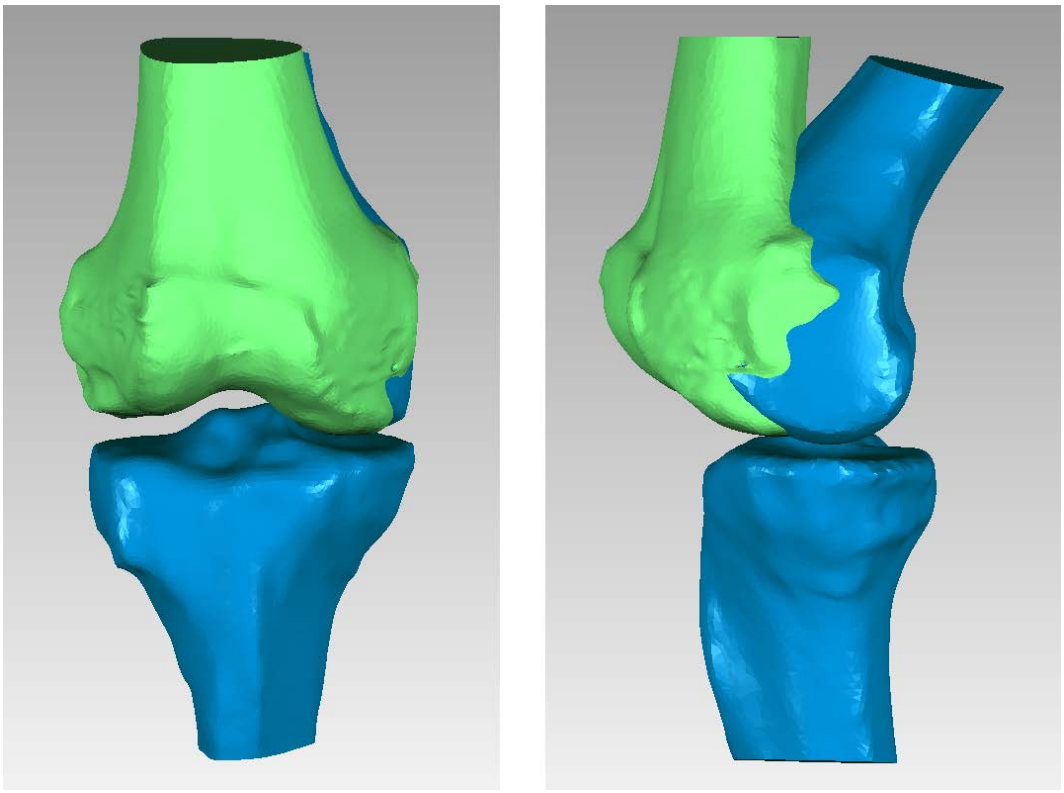

Figure 1-4 – Image of the change in femoral bone apposition from MRI relaxed (blue) position to CT loaded (green) position after registering the tibial models together.

In DICOM radiologic files, metadata are stored along with the image, providing information about things such as the scanner used, time of acquisition, acquisition sequence, or image size and dimensions. The 3D scene in which registration takes place is constructed from pieces of this metadata, specifically ones that reflect the details of the radiographic beam path and source/detector positioning. A coordinate system for each bone surface model is defined at the centroid of the model vertices, and directions are kept consistent with those of the MRI space. Cartilage surface models use the same centroid as their associated bone models so that the two move simultaneously. This provides a consistent method for recording model movements in terms of translations and rotations about a persistent origin. [44]

Optimization of the silhouette fit was performed using a covariance matrix adaptation evolution strategy (CMA-ES) that iterates through poses to find a "best-fit" for the model in 3D space based on its projection onto the radiograph. [45] No matter the registration method (edge tracing or gradient), a cost based on the distance between edge/gradient image and the bone model silhouette is associated with each iteration of the registration process. When this cost has been minimized, the algorithm considers the registration to be complete. In Figure 1-5 (image from Markelj et al.., 2012), a grid of currently used registration methods is shown. Our method uses the feature-based projection model seen in the upper left corner of the grid. This method was chosen because it is more easily implemented, and less time-expensive than the others. This feature-based projection model is shown throughout the CMA-ES optimization method in Figure 1-6 (image from Anderson et al., 2012). For this method, only ray-model edge intersections are required to produce the bone surface model silhouette. For others methods such as intensity and gradient-based, a ray-model edge intersection is computed for every pixel in the image. [42] More recent attempts at 3D-3D registration have produced a sinogram to sinogram registration method. When a CT is acquired, the raw data generated is in the form of a sinogram, or a collection of histograms generated for each slice based on the amount of x-ray attenuation at each point along a slice. Instead of reconstructing a 3D volume for registration purposes (and potentially losing accuracy), the raw data provides a means of registration based on local intensity gradients in the sinogram. This method works quite well for registration between CT images, but has not been attempted using MRI. [46]

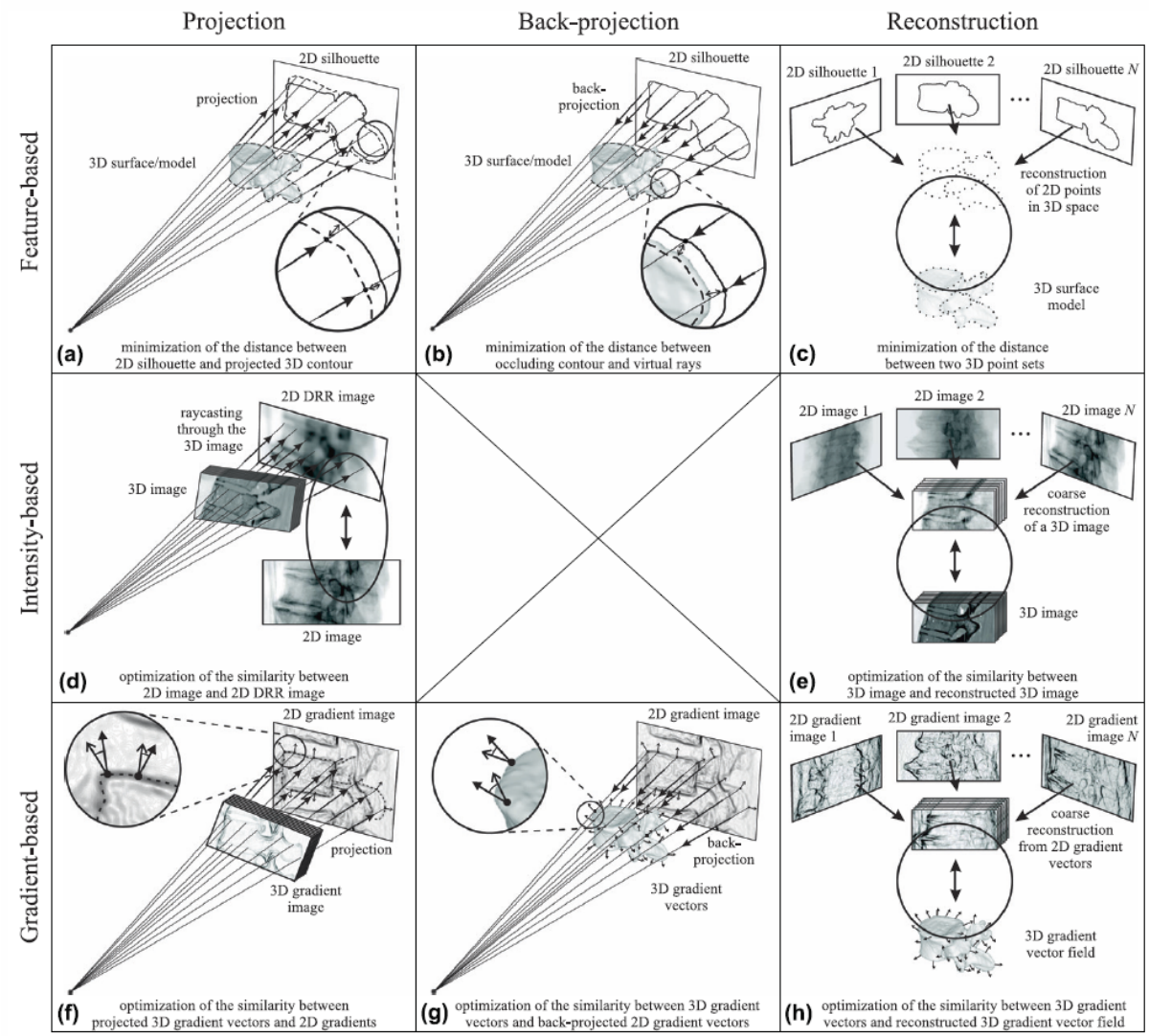

Figure 1-5 – Diagram of commonly implemented registration methods.

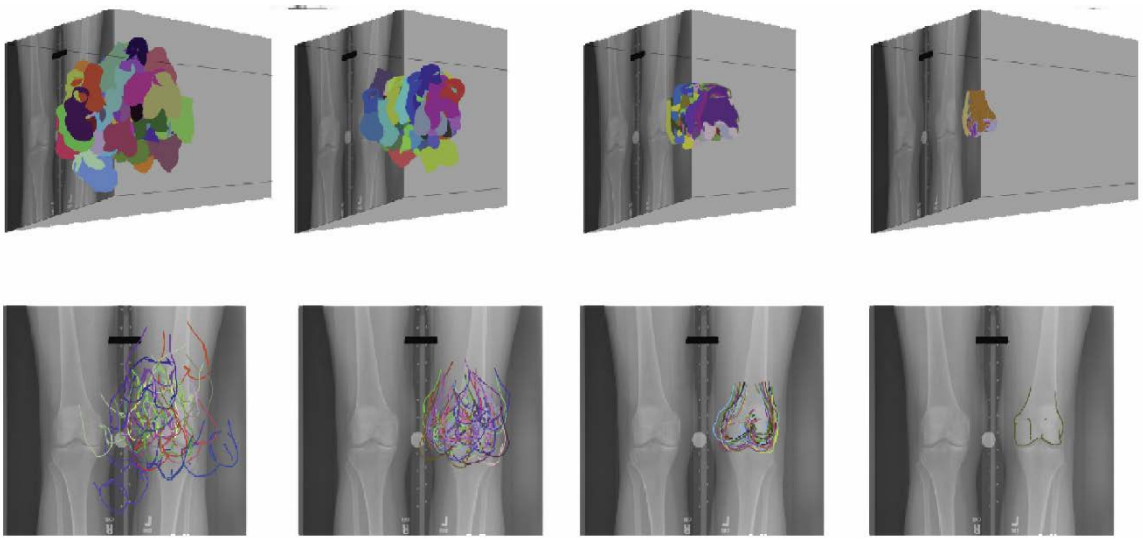

Figure 1-6 – Depiction of CMA-ES algorithm at work. From left to right, iterations of the optimizer produce families of results to choose from, and eventually narrow the search pool by minimizing the distance between projective bone silhouette and edge tracing or gradient image.

1.4.3 Boundary Conditions and Material Properties

In performing a stress computation given patient-specific bone and cartilage models, contacting surfaces are assigned material properties based on values reported in literature. For cartilage, a Young's modulus of 4 MPa was used alongside a Poisson's ratio of 0.42. [47, 48] Articular cartilage exhibits a poroelastic material behavior that depends upon the rate at which it is loaded. For the present work an "equilibrium modulus" is used to reflect the prolonged flexed-knee stance. Once registered to a load-bearing radiographic image, the paired bone and cartilage surface models are constrained rotationally (completely) and translationally (depending on the method of loading). The rotational constraints are imposed in order to give a result for static loading, since the knee has been registered to the position of interest. Two main methods can be employed for bringing the models into contact for stress computation, each of which will be discussed further in the next section. However, in terms of degrees of freedom, it should be noted that in load control, the femur is allowed to translate inferiorly/superiorly to

create the stress estimate. Other than this single DOF, all other movement is locked. In the second method, displacement control, all DOF's are locked. Load at this position is assumed to be transmitted vertically through the femur due to muscle and other soft tissue forces holding the femur in place. When bone model positioning is perfectly replicated, cartilage contact is defined by the overlap between the corresponding cartilage surfaces. Constraining the model so much in load control is reasonably assumed, as the soft tissue helps to direct forces directly vertically through the tibia.

1.4.4 Stress Analysis

Once the models are registered and boundary conditions applied, the DEA computation is performed. The cartilage surface model obtained via segmentation is assumed to be in an undeformed configuration, due to the relaxed position of the knee in MRI. The cartilage surface model is comprised of triangular facets that are each assigned a stiffness in the form of a spring constant relating to the material properties of cartilage, based on their distance from their corresponding bone surface (cartilage thickness). In essence, each facet has a spring normal to its surface that deforms when it contacts its nearest-neighboring spring on the opposite contact surface. [28, 49-54] Springs for each cartilage surface are defined and implemented in series after aligning the spring directions. (Figure 1-7)

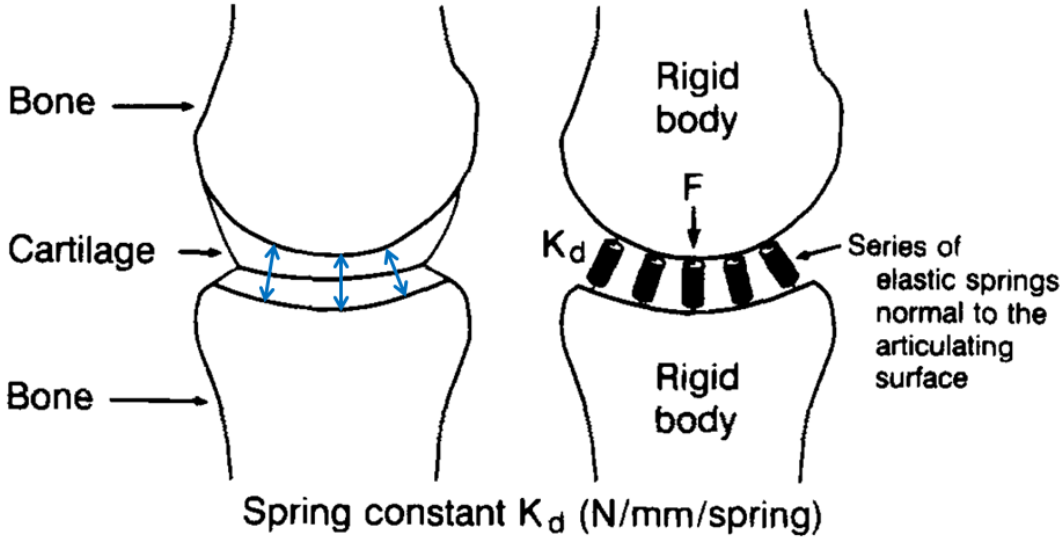

Figure 1-7 – Basic idea behind rigid multi-body analysis (DEA). Each surface is assigned springs normal to its element faces that deform when in contact with those of the opposing surface.

As the femoral cartilage model comes into contact with the tibial cartilage via applied load or displacement, the surfaces overclose and their springs deform based on this overclosure. [55] This overclosure is shown in Figure 1-8 (image from Bei et al., 2004). Based on the force engendered in each spring (computed based on spring stiffness and amount of overclosure), the stress can be computed over any given element's area. The equation below shows the relationship between pressure and overclosure (represented as spring deformation), where *v* is Poisson's ratio, *E* is Young's modulus, *d* is the spring deformation and *h* is the additive thickness of the cartilage areas in contact, depicted as blue arrows in Figure 1-7 (image from Schuind et al., 1995). [31, 56, 57]

$$pressure = \frac{(1-v)E}{(1+v)(1-2v)}\frac{d}{h}$$

Equation 1 – Pressure calculation for overclosure of rigid surface models.

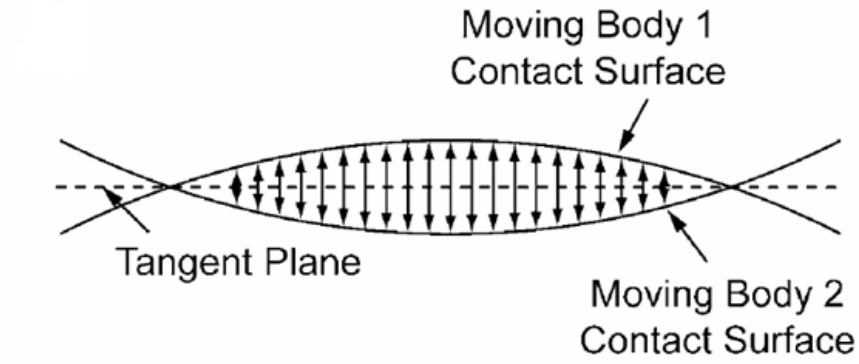

Figure 1-8 – Depiction of overclosure of two rigid body models and the distance of overclosure. This overclosure is analogous to spring deformation, and is utilized to compute engendered spring forces.

As previously mentioned, there are two main ways to bring the models into contact for this stress computation. If registration is assumed to have negligible error, displacement control may be used, and contact computed based solely on the registered position of the bone and cartilage surface models. This method assumes that cartilage deformation that is occurring will be captured by overlap of the cartilage models in this pose. Even slight registration errors (±0.1 mm or degree), especially in superior-inferior translation and varus-valgus rotation can produce substantial shifts in contact force, pressure, and area of up to 204, 100, and 117% respectively. [57] These shifts were seen in knees with implanted metal on polyethylene knee replacements, but the idea can be extrapolated (though maybe to a lesser degree) to healthy knee contact. When error in the registrations becomes an issue, the method of load control can be utilized to ensure contact between the models.

In load control, the femoral model is initially stepped vertically away from the tibia and then iterates into contact with the tibial cartilage until a percentage of the subject's body weight is recovered from the resulting stress map. Based on the subject's

knee flexion angle, a certain load can be assumed to pass through the joint. Intuition would suggest that 50% of a subject's body weight would pass through each knee, but this may be an oversimplification. When in a flexed stance, the muscle forces on the knee can create higher loads on the tibiofemoral joint than 50% based on the degree of flexion. [16] Based on this literature, we have opted to use 80% of a subject's body weight when running the DEA process if load control is used.

1.5 Gaps in DEA Functionality

1.5.1 Multi-planar imaging modalities

1.5.1.1 Weight-Bearing Imaging

Weight-bearing radiography has long been used in the diagnostic examination of the human knee. Features such as joint-space narrowing or varus/valgus deformity are more pronounced under load than in a traditional supine radiograph of the knee. Conventional techniques include obtaining a PA radiograph for such examination. [58] As previously mentioned, DEA uses a loaded pose radiograph to determine the position of the bone models. Previous methods used by our group have successfully performed registrations to single radiographic images. However, in registering a bone model to a radiographic image, intuition would suggest that multiple views of the same pose would provide better registration than just one. Typical errors using single-plane and bi-plane radiography have been measured at ±0.5 mm and ±0.1 mm, respectively. [57] Bi-planar radiography systems such as the EOS system provide two images obtained at the same point in time, allowing for simultaneous registration to two orthogonal views of the knee. Other groups have created custom multi-planar setups using their own single-plane radiography devices. [59, 60] Bi-planar radiography ensures a much more accurate registration along a direction coincident with the radiographic beam in single-plane radiography. Even if two views are obtained using single-plane radiography, unless

obtained simultaneously, it cannot be assumed that the two images depict the exact same knee position due to any knee motion between acquisitions.

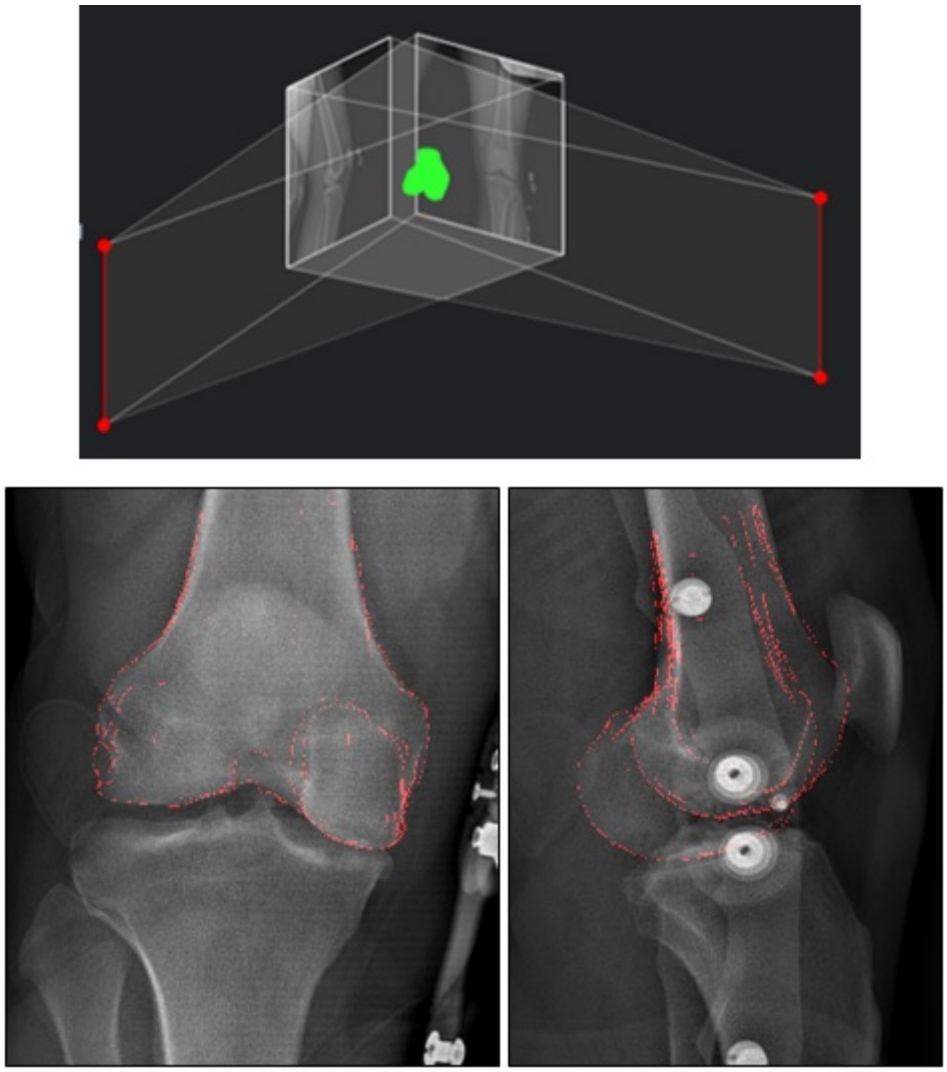

Figure 1-9 – Virtual space in which a model is registered to orthogonal bi-planar radiographs (top) and resulting bone model registration (bottom). Circles in the image are the joints of a brace designed for unicompartmenal unloading.

Beyond the realm of bi-planar weight-bearing registration lies the possibility of using weight-bearing CT or MRI. In one of these configurations, segmentation can be

performed directly from the image, without a need for registration. However, since CT currently does not provide the soft tissue resolution needed to segment the meniscus and cartilage surfaces, MRI imaging is required at some point to obtain the undeformed surface model geometries needed for DEA computation. The difficulty in imposing a load-bearing state on a joint in either of these 3D imaging modalities lies in the horizontal movement of the gantry. The knee must be loaded without the subject standing. This requires the construction of a device to load the knee that is strong enough to withstand force being transmitted through it, able to fit in or on the scanner, and compatible with the modality limitations (such as non-ferromagnetic in MRI). Various groups have used loading frames of this nature, with reasonable success. [61-63] Applications include successful measurement of patellofemoral contact area increase with knee flexion, as well as examination of patellar tilt under knee flexion.

Dynamic MRI techniques have also been suggested for motion and load-bearing imaging. [64] Upright, loaded MRI imaging is also in current use for tibiofemoral movement measurements as well as imaging of the spine under loading. Such imaging requires a machine capable of vertical scanning, and such machines are only just beginning to become available for research use. (Signa SPIO; General Electrical Medical Systems, Milwaukee, Wisconsin) [65] Lack of radiation exposure to the subject is of obvious advantage, as well as ability to discern between soft tissues. However, the higher resolution seen in MRI comes at a cost of time spent scanning. This extended image capture time in turn corresponds to the requirement of little to no movement to avoid risk of motion artifact. Scans taken in upright, load-bearing MRI are subject to lower resolution due to increased scan speed. [65-68]

1.5.1.2 New 3D Weight-bearing Imaging Capability

A novel method for obtaining loaded pose images has arisen for use in the research and clinical settings. A prototype weight-bearing CT (WBCT) scanner provided

by CurveBeam (Warrington, PA) was used in this thesis research to obtain fixed-flexion images at lower radiation levels than conventional CT. The advantages to the use of such a modality are both innovative and substantial. Using a cone-beam source rotating in sync with and opposite a detector panel, CT "slices" are obtained at 360 single degree intervals through one full rotation of the scanner. In essence, a registration that before used one or two views can now be performed using up to 360, increasing time to register but providing the bone surface model many more images to which it can register. Likewise, slices of the CT can be hand-picked based on image quality and level of artifact to provide the best possible registration. Future studies can now employ a more complete registration scene. Additionally, scan times are much shorter than that of MRI. The frequent availability and expanded capability of this scanner makes it perfect for obtaining images for the 3D-2D registration step in the DEA process, especially for validation purposes. Use of this technology for development of the 3D bone model-to-2D radiograph registration process is discussed in the following chapter.

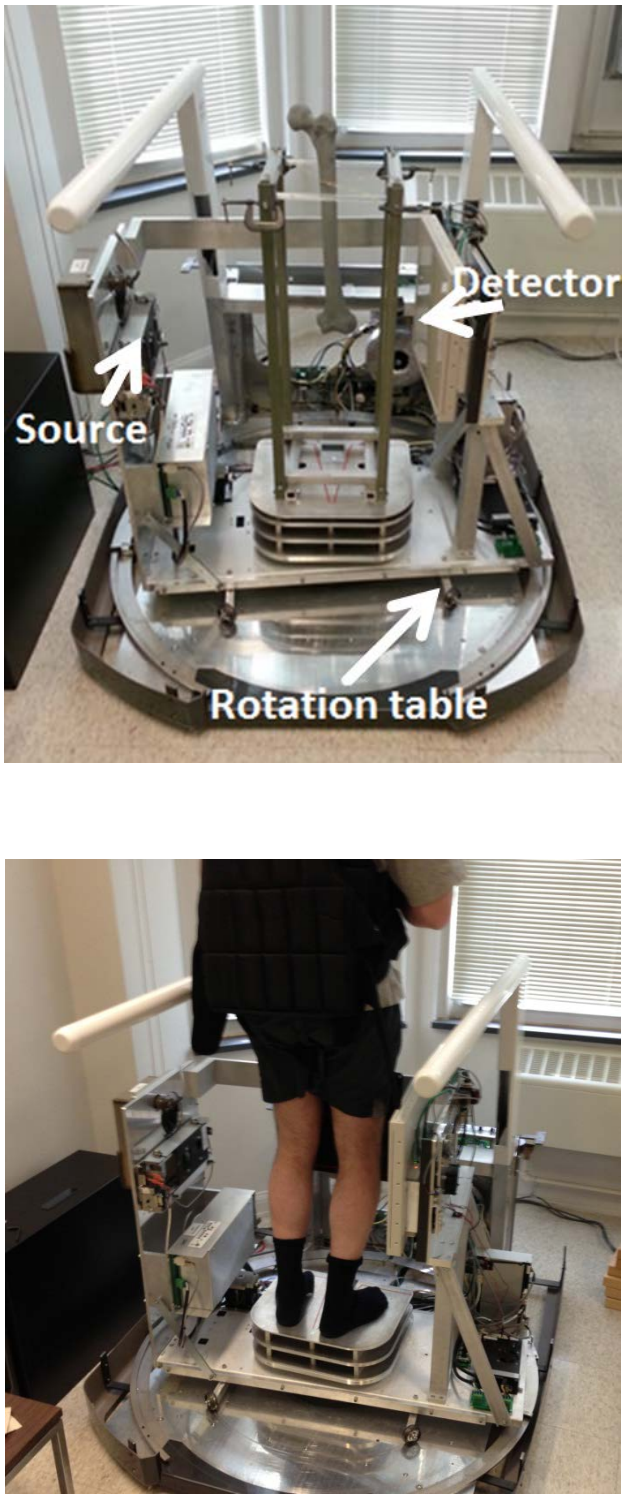

Figure 1-10 – Images of the prototype WBCT scanner with loading frame under development (top) and with subject in flexed-knee stance (bottom). The patient's knees rest against an anterior restraining plate.

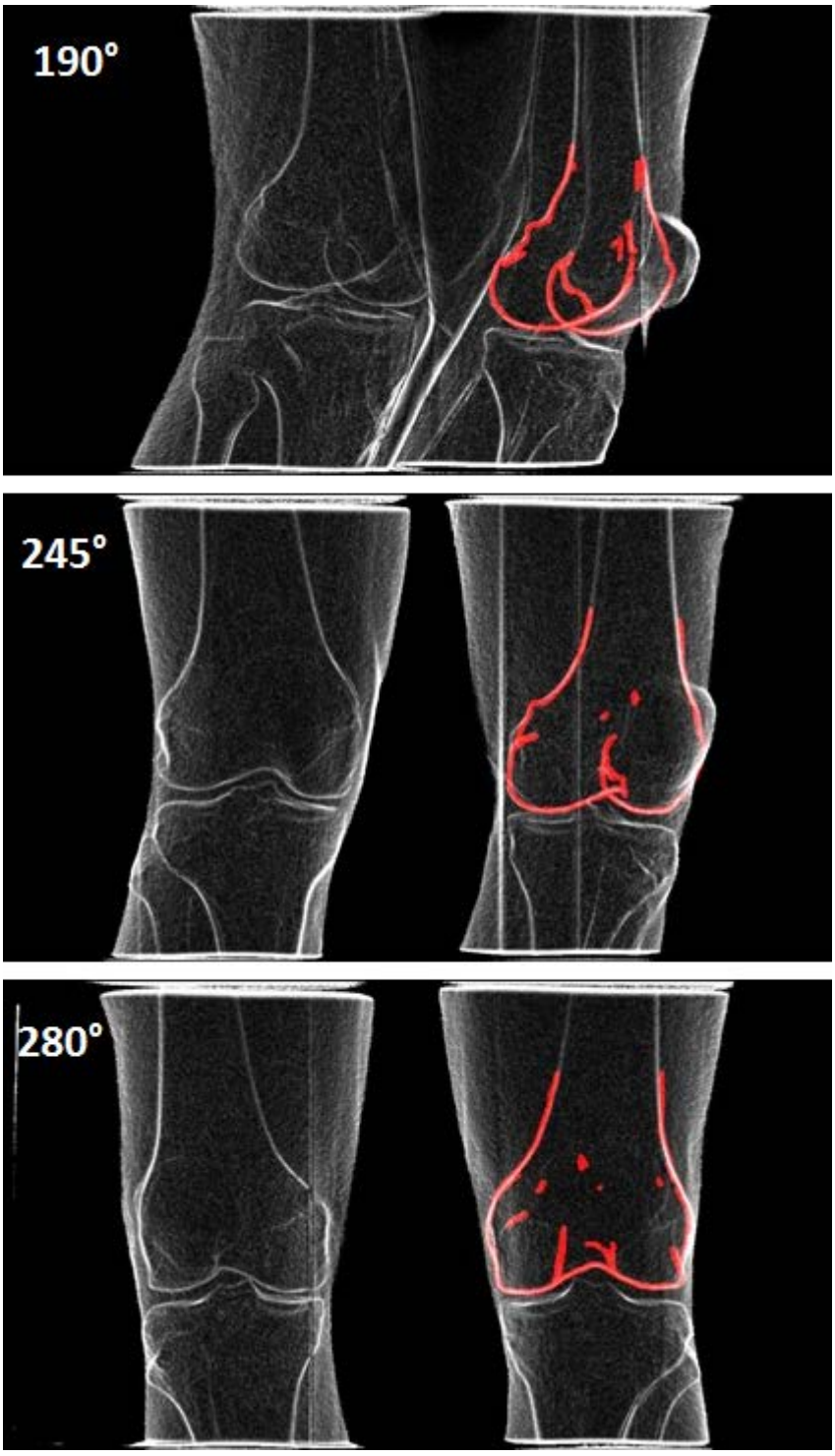

Figure 1-11 – Three slices taken from a WBCT scan. Up to 360 poses can be registered to simultaneously, but three are shown here as an example with the bone model silhouette shown in red, superimposed using MATLAB.

1.5.2 Need for Validation

As previously stated, prior research conducted using a DEA method for computing contact stress between bone-cartilage surfaces in both the knee and ankle has proven both expeditious and accurate. Furthermore, it has been observed that stress estimates using this method indicate higher stress in the cartilage of subjects that later develop OA of the knee. [18] The next logical step is to perform a validation to determine the usefulness of DEA methods for use in the tibiofemoral joint of the knee. Although correlation between contact stress and OA progression has been reported, a validation will lend support to the current methodology.

1.5.2.1 General Validation Methodology

In vivo measurement of knee contact stress would provide novel insights into loading under muscle and ligament forces, but obtaining this type of measurement is extremely invasive. Such a technique would involve an incision to access the capsule of the knee and subsequent placement of a sensor within the joint space. Even so, it has been performed at least once to detect unloading of knee compartments by bracing. [69] This is most certainly a novel approach and "technically feasible", but the reality is that widespread invasive measurement of joint contact stress is not realistic, even in a research setting. Therefore, cadaveric validation as a means to corroborate DEA stress calculations is widely accepted as the most reasonable approach. Although computational modeling methods can vary substantially across research groups, the means by which these models are validated generally do not. Cadaveric specimens are obtained and dissected, to provide room for sensor insertion into the joint space. There are two sensors that are seen most commonly in validation studies. Tekscan pressure sensors (Tekscan, Inc.) provide dynamic feedback during sensor positioning, and can be used to ensure that the sensor is in the best possible location for load recovery. [22] Fujifilm (Fujifilm Holdings) pressure-sensitive film is also frequently used for stress measurement in

orthopedic applications, such as hip joint stress measurement. [70] Once the sensor is in place, load is passed through the joint along specific axes of interest to the researchers. Given readings from the sensor, researchers can compare to results from their computational modeling methodology. Of particular interest in validations involving contact stress are peak and mean stress, contact patch shape and location, and amount of applied load that is recovered through the sensor. [17, 28, 57, 69, 71]

1.5.2.2 Prior Validation of Current DEA Method in the Ankle

The DEA method currently being employed has been validated within the human ankle using the bone morphologies and material properties from a previously validated FEA model. [22] A custom-built loading fixture was used to allow articulation in the tibiotalar joint while a 600N load was applied axially through the tibia. A Tekscan sensor was placed within the joint to measure contact stress. Very comparable results were found between physical, FEA, and DEA methods (Figure 1-12, image from Kern, 2011). It was shown, however, that DEA tended to overestimate contact stress in generally higher stress areas and underestimate in lower stress areas. This may be due to the cartilage models' non-deformable treatment in the DEA model, and thus their inability to adapt the shape of the contacting areas, as might be seen in vivo. [34] A validation was designed to test contact stress estimation in the knee using similar methods, in an attempt to obtain comparable validity as the ankle model.

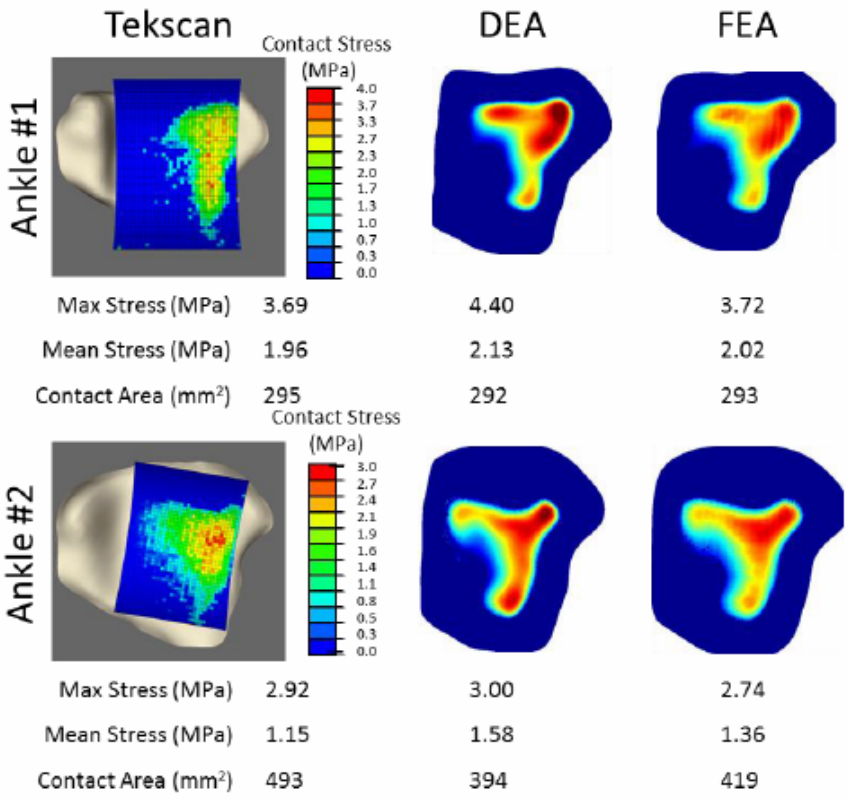

Figure 1-12 – Results from DEA validation study in the ankle. Results for both DEA and FEA are comparable to those in Tekscan readings. DEA tends to overestimate in areas of higher stress.

1.5.3 Meniscal Modeling

Modeling of loading in the human knee is much more challenging than in the ankle due to the presence of the meniscus. The necessity of including a meniscus in the DEA model requires a method for addressing the more deformable and mobile nature of the meniscal structure.

1.5.3.1 Meniscal Modeling Techniques

Multiple groups, especially those working in FEA, have performed biomechanical analyses of the knee with the meniscus included. The meniscus is stiffer in axial

compression between cartilage surfaces, and fairly mobile. This is attributed to its shape and position atop the tibial cartilage, as well as the ligamentous attachment of meniscus to bone. FEA, with its ability to handle complex deformation, can directly accommodate a meniscus. Studies focused solely on meniscus mechanics have been conducted that show the contact stress and area differences between torn and healthy menisci. Tears in the meniscus cause irregular contact patches when compared to the healthy meniscus, and full meniscectomy results in higher contact stress in the cartilage due to the smaller contact area. [72, 73] To account for the time-varying nature of the material properties for meniscus and articular cartilage, some models use a hyper-elastic deformation model such as Mooney-Rivlin. [74] DEA models have also integrated a meniscus into their stress computation. Guess et al. accomplished this by dividing the menisci radially into discrete elements. A stiffness matrix was then assigned between elements to determine capacity for deformation, and the model was allowed to deform outward under load. Results were comparable between their DEA method and traditional FEA methods (Figure 1-13, image from Guess et al., 2010). [75] The results produced from this method indicate that it is a very accurate way to model the deformability of the meniscus, and suggest that proper implementation will result in accurate meniscal DEA readings.

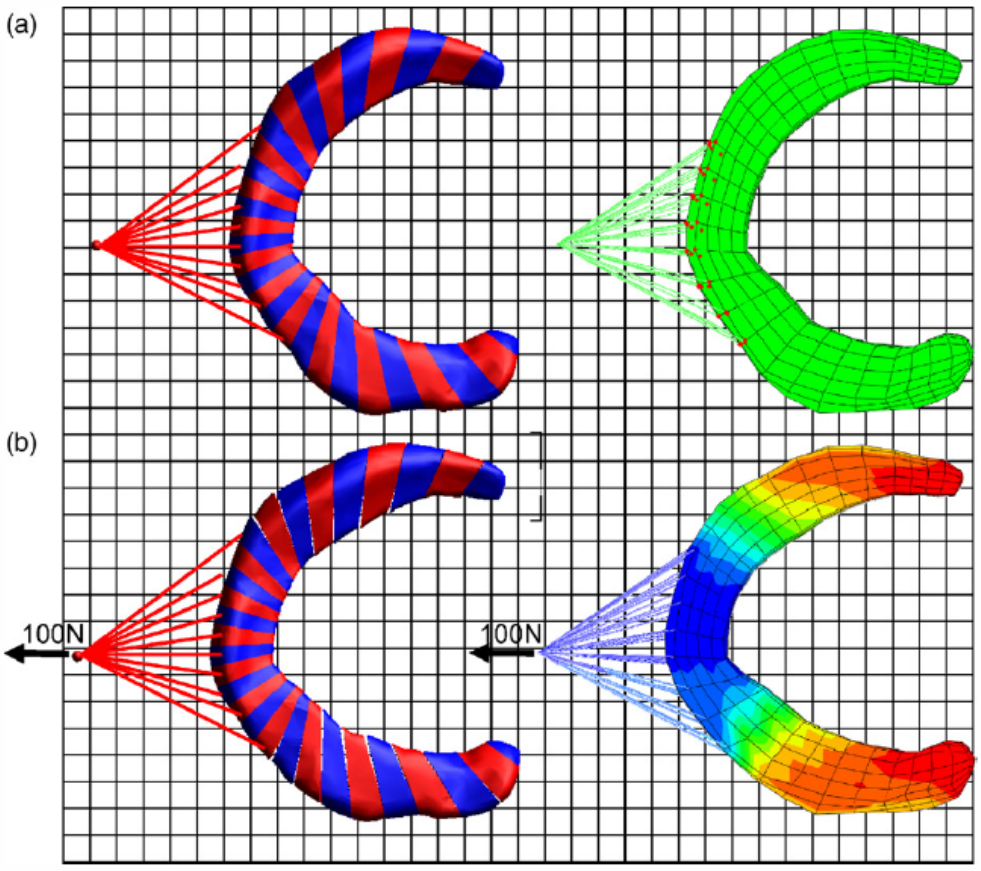

Figure 1-13 – Deformation of meniscus in a DEA model using radial partitioning of the meniscus. Each element is comprised of many individual DEA "springs" and connected using a 6x6 stiffness matrix. Red and blue labels are for distinguishing between alternating elements. The top row shows a relaxed meniscus for the DEA model (left) and an FEA comparison model of stresses between elements (right). The bottom row shows resulting meniscal shape under 100N of load.

This method takes into account much of the meniscal movement that would otherwise be excluded from a DEA model, as the menisci have been seen to deform substantially when the knee is flexed and extended while under load. In particular, the meniscus' anterior horn is seen to translate up to 9.5mm anteriorly, the posterior horn translates up to 5.6mm, and radial translation is seen of up to 3.7mm as the knee is flexed from full extension to 90° of flexion. [76] Thompson et al. found similar results that

displayed further excursion of the meniscus as the knee is flexed under load. [77] Figure 1-14 displays these results for both studies. (Images from Thompson et al., 1991 and Vedi et al., 1999) However, when a knee is held in a fixed degree of flexion and loaded, the motion of the meniscus from unloaded to loaded position is relatively small. Nonetheless, it is desirable to accommodate meniscal contact when using the DEA model for subjects with relatively healthy menisci.

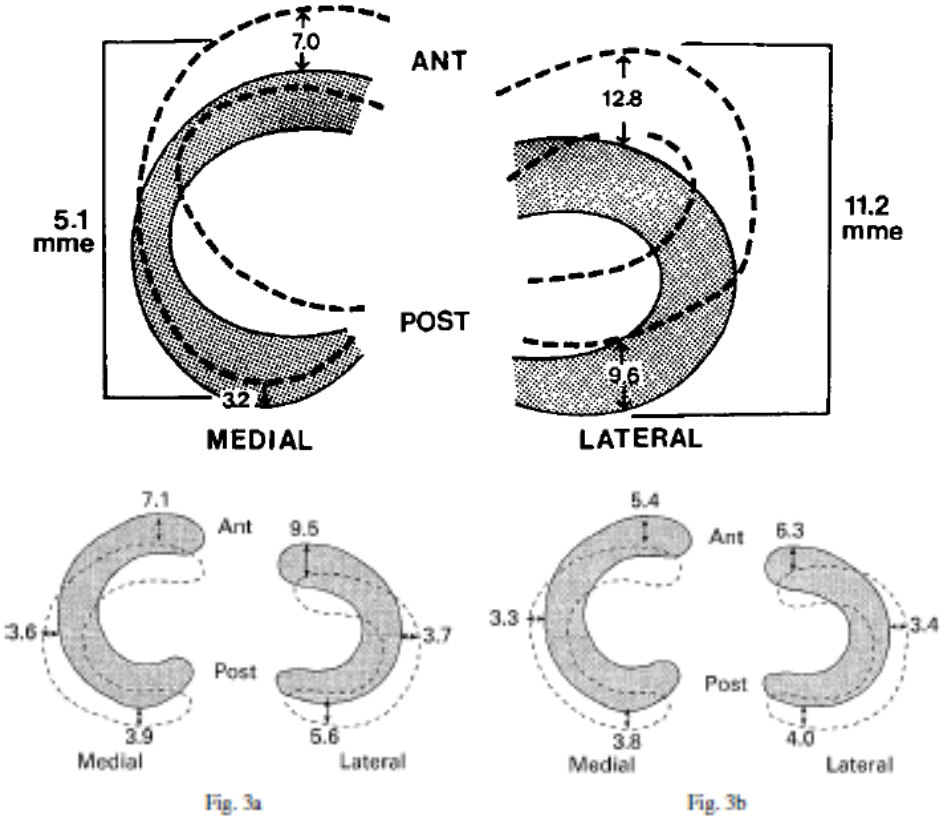

Figure 1-14 – Images depicting meniscal excursion in full extension (bottom left), relaxed sitting position (bottom right) and in flexion (top). Units are all in millimeters.

1.5.3.2 Proposed Implementation

Work by Anderson et al. introduced a method for incorporating an interposed meniscus in a DEA modeling schema. [54] Placing the meniscal surface model in series with other intra-articular surface models (in this case bone and articular cartilage), stress can be computed by combining stress through the meniscus with that in the cartilage. This method for computing contact stress with the meniscus requires segmentation of the superior and inferior meniscal surfaces to be included in the stress estimation. Using the two segmented meniscal surfaces, thickness of the meniscus is computed between nearest-neighbors on the opposing surfaces. This is identical to the method for finding cartilage thickness in the current DEA implementation. Next, nearest-neighbors are computed between the tibial cartilage surface and inferior meniscus in order to pair a cartilage thickness with each meniscal thickness. Because the paired cartilage and meniscus thicknesses can be given a composite spring stiffness value, contact of the femur with the meniscus/tibial cartilage layers can be treated as springs in series.

$$k_{composite} = [(1/k_{cartilage}) + (1/k_{meniscus})]^{-1}$$

Equation 2 – Equation for computing composite spring stiffness based on individual cartilage and meniscus stiffnesses.

In this same paper, 24 knees were chosen to test this theory. Knees were chosen based on the ability to segment the meniscus. [54] A Young's modulus of 80 MPa and Poisson's ratio of 0.3 were chosen for meniscus material properties based on values given by Donahue et al. [78] Using these values with the cartilage and meniscal thicknesses, a composite spring value can be computed for areas in which both cartilage and meniscus lie in series. Results from Anderson's study showed increased contact area due to the inclusion of the meniscus when the same model displacements were applied as in the

meniscus-free scenario. Only minor differences were observed between maximum contact stress values between femoral cartilage and superior meniscus, however. [54]

Based on the amount of meniscal movement reported by Thompson and Vedi, meniscal movement may need to be modeled in order to compute accurate stress estimates. This is a significant step in validating the use of the meniscus in knee DEA. Incorporating this novel measure, alongside the use of weight-bearing imaging technology, the DEA methodology once again needs to be proven valid in a physical setting. The remainder of this thesis focuses on validation of the DEA model as a whole, including the aspect of 3D-2D registration. Inclusion of a meniscus in the model will further inform decisions regarding knee contact stress measurement.

CHAPTER 2: VALIDATION OF DEA METHODS IN THE KNEE

2.1 Validation Goals

The purpose of this study was to validate three different aspects of the current DEA methodology used to model static flexed-knee loading. The primary goal was to determine validity of contact stresses predicted using a simplified surface contact model. This validation required direct intra-articular contact stress measurement within a knee loaded in a flexed pose and comparison of the measured stresses with those computed using DEA.

Secondly, the 3D-2D registration method needed further validation. Because model registration directly influences DEA contact stress computations, this step in the overall validation was of equivalent importance to the stress comparison. The ability of our registration algorithm to perform its intended task would need to be measured against some type of 3D-3D registration gold standard, best exemplified by a fiducial marker registration.

Lastly, in the course of examining the aforementioned aspects of the DEA implementation, it was proposed that movement of the meniscus under loading be studied. Meniscal contribution in loading of the knee had not previously been addressed using the current modeling approach, so an attempt at tracking deformability and mobility of the meniscus was deemed necessary. Such tracking of the meniscus could be accomplished by visual detection of the entire structure, or by placing some type of marker on easily tracked landmarks. Tracking meniscal movement and deformation was originally defined as a secondary goal whose purpose was to inform further research involving biomechanics of the knee. In the course of the validation, it was discovered that this movement was integral to the DEA component of the study involving a meniscus, and consequently it became a key area of focus.

2.2 Validation Methods

2.2.1 Design and Construction of Loading Frame

In order to address the first and third validation goals, a fixture for loading knee specimens in a flexed position was required. A custom frame for holding and loading cadaveric knee specimens was constructed for placement in the WBCT. Of primary importance, the frame was designed to fit within the volume circumscribed by the CT scan gantry. This corresponded to a cylindrical volume with a diameter of 15.25 inches. Secondly, material selection was considered in order to avoid excessive metal artifact and obstruction of the knees in the CT images. In order to meet these criteria and still maintain the structural integrity of the frame, structural fiberglass was chosen for its vertical members (low enough density to be seen minimally on CT). Aluminum cross-bracing was added to provide greater strength and stability to the frame. These members were designed to be outside the field of view of the scanner, so as to avoid unnecessary metal artifact.

Next, a method to secure a cadaveric knee in the frame was chosen to provide maximum rotational and translational freedom of the joint before being locked into its "settled" position. To allow the knee to reach this loaded position, a transverse plane translational table was implemented in series with features for varus-valgus rotation and axial displacement. The translational table was the only one of these features attached directly to the frame, with the others riding along. In positioning the knee, the tibia was potted within a PMMA block, which was then fixed within a steel sleeve protruding from the frame base at 10° from vertical. The femur was then also potted in PMMA, and attached to the upper carriage via an aluminum plate, bolt and lock washer. This attachment site was designed at an angle of 10° as well, resulting in an overall knee flexion angle of 20°. This angle was based on clinical standards used to radiographically determine joint space width in patients with OA. [38]

When attaching the femur to this fixture, slight toggle was allowed at the interface, as this also served as the varus-valgus degree of freedom. The joint was then subjected to a slight femoral pre-load (< 5 lbs) to induce soft tissue tension and alignment of congruent surfaces, and to reach its "settled" loaded position. Once settled, all degrees of freedom were locked via clamping collars, except for vertical translation of the load-bearing steel rod, which was allowed to move through a linear ball bearing. At the femoral end of this rod, a 10° angled plate was attached to provide the knee 10° of flexion beyond the tibial fixation. Through this angled plate, a rod allowing axial rotation was passed. Lastly, the attachment site for the plate in the femoral PMMA and varus-valgus rotational freedom was designed into the end of this rod. Once the degrees of freedom were locked down, load could be passed vertically through the joint by placing weights on top of the loading rod. The loading frame and its components are shown in Figure 2-1.

Although the frame was designed to be very rigid, supplemental bracing was added to avoid any shearing motion that could occur in the joint from frame or bone flexure. As the DEA formulation assumes rigid bones with load passing only vertically through the femur to the tibia, this was merely an additional measure to ensure no bone movement from frame or bone flexure. This extra bracing was designed in the form of adjustable anterior bracing panels. Once DOFs were locked for the frame, these panels were situated against the anterior aspects of both the tibia and femur prior to loading. An image of the anterior bracing panels is shown in Figure 2-2.

Figure 2-1 – Validation frame implementing all DoF's as designed. The position of components shown is similar to their position when attached to a knee and loaded. (left) Moveable components of the WBCT loading frame: (1) vertical load applicator, (2) transverse plane translation table, (3) axial bone rotation mechanism, (4) varus/valgus rotation mechanism. (Right) Not pictured on the right is the tibial angle fixation, which can be seen attached to the base on the left.[1]

[1] Frame design and material selection were items of collaboration between Thomas Baer, Jim Rudert, and Tyler Stockman. The X-Y table was adapted from a similar frame to one that would fit in the WBCT.

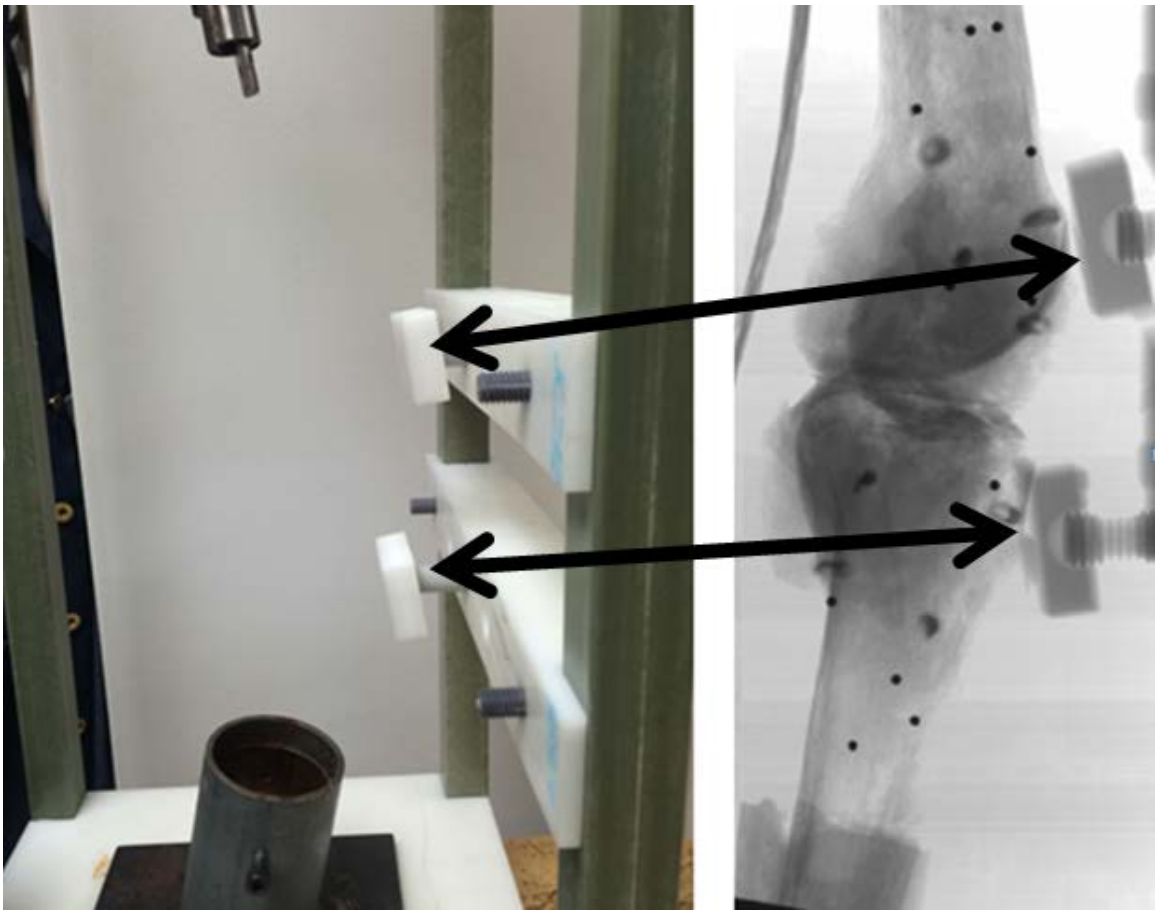

Figure 2-2 –Anterior bracing setup used during loading (left) and use in WBCT (right).

2.2.2 Specimen Selection and Initial Preparation

Two fresh-frozen cadaveric specimens were obtained from the University of Iowa Deeded Bodies program for validation testing. Each knee had been amputated near mid-femur and mid-tibia. The knees were intact and free from any surgical alterations. Although age and gender of the specimens were not known, it was noted during visual inspection by an orthopaedic surgeon that both exhibited slight cartilage and meniscal wear, and Knee 1 had patellar osteophytes. All surgical preparation described hereafter was performed by the surgeon (Dr. Yuki Tochigi) unless noted otherwise.

Preparation of the specimens proceeded in several stages, outlined in Figure 2-8. Initial preparation involved removal of soft tissue to just above and below the joint capsule, and potting of the distal tibia and the proximal femur in 2 inch diameter PMMA cylinders for attachment to the loading frame. Bones were potted with the bone axis aligned to the axis of the cylinder to allow later rotation. To attach the aluminum fixation plate to the femur, a notch was cut in the PMMA cylinder and the plate sandwiched between remaining PMMA. A hole was drilled through the layers and a bolt was passed through to fix the plate.

2.2.3 Data Collection

a first attempt at tracking meniscal movement was undertaken. One at a time, each knee was attached to the loading frame and Isovue contrast medium was injected into the joint space. This contrast medium is used *in vivo* to visualize the surfaces of the knee joint and is particularly useful in diagnosing meniscal tears. Using this method, an overall deformation of the meniscus was to be tracked using unloaded and loaded CT images. A WBCT scan was then taken of the unloaded knee to obtain an unloaded "starting" position A second WBCT scan was then taken to obtain an image of the loaded position.

After initial dissection and potting of the specimens, the specimens were prepared for assessment of our current 3D-2D registration algorithm. First, the joint capsule was removed. Prior dissection provided access to the menisci, cartilage surfaces, and bone surfaces near the joint. Fiducial markers in the form of 2.1mm diameter spherical tantalum beads were implanted just below the bony surface by drilling a pilot hole with a hand driver and press-fitting the bead into the resulting hole. Six markers for each bone (tibia and femur) were seated in this manner for tracking bone movement.

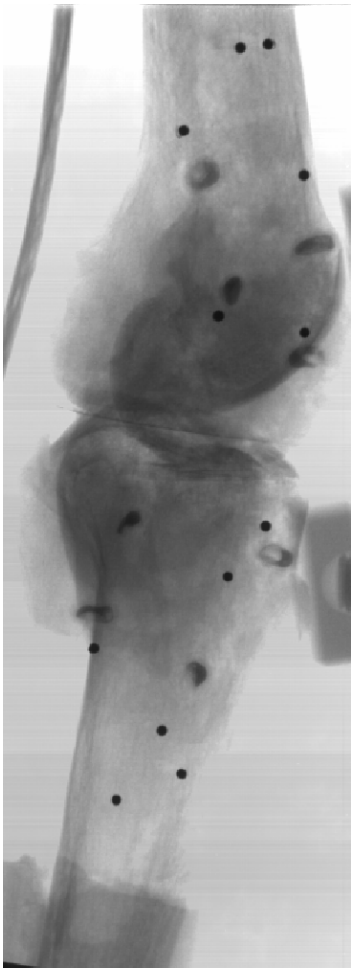

Figure 2-3 – Tantalum marker beads within the femur and tibia. Clarity of these markers in WBCT images provided easy identification and segmentation.

The last addition at this stage was a silastic tube filled with contrast solution (same solution as used previously) and sutured to the superior rims of the menisci. The contrast solution was chosen for its ability to be seen in both MR and CT modalities, which provided a convenient way to track positions of the meniscal tubes from fully relaxed (MRI) to both unloaded and loaded positions (CT). This was done to provide a secondary method of meniscal movement measurement, one that could more easily be quantified. Although more easily quantified, it would not provide complete meniscal movement data; only the superior rim of the meniscus could be tracked.

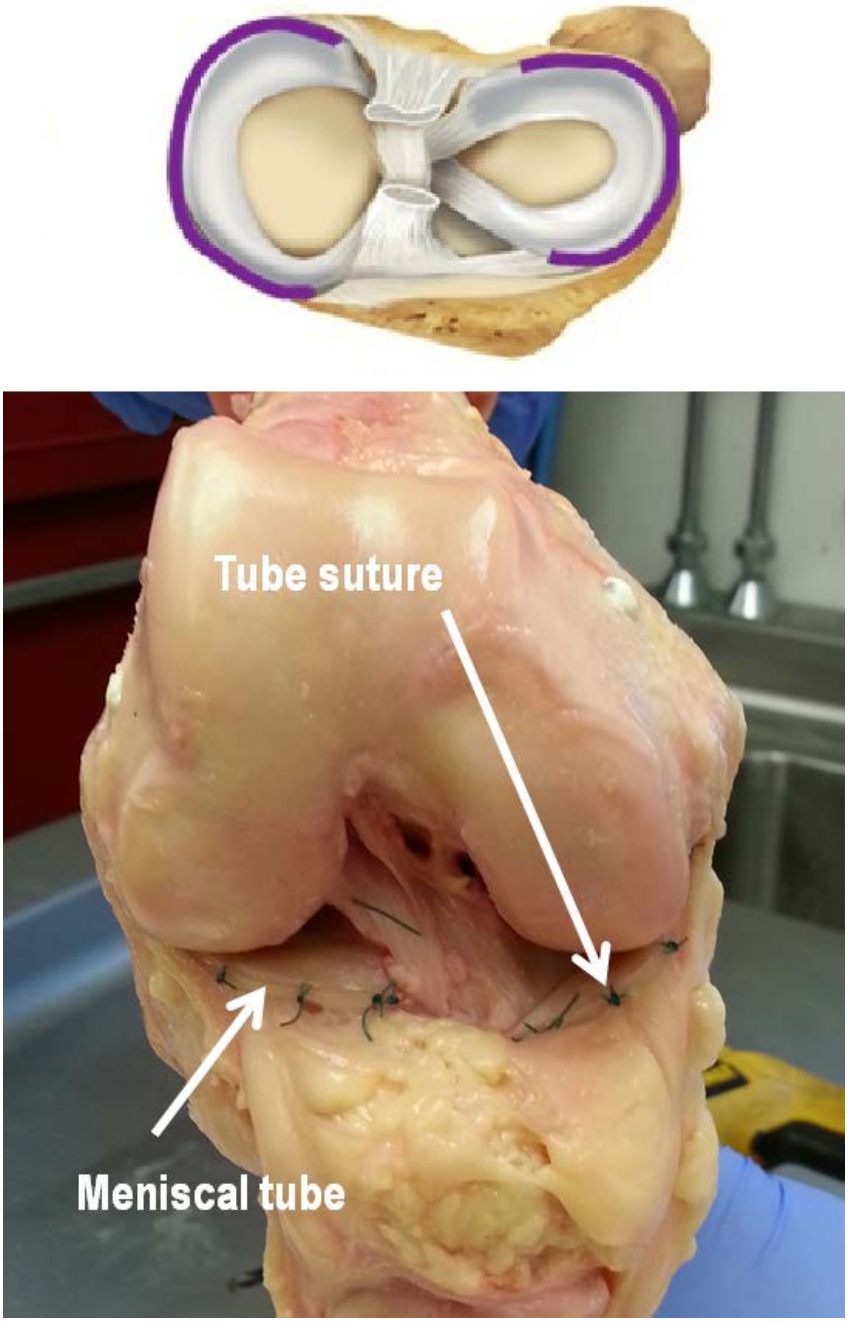

Figure 2-4 – Diagram of meniscal tube location in purple (top). Picture of meniscal tube implementation in cadaveric knee (bottom). Green strings in image are tube sutures.[2]

[2] Top image from http://www.sportklinik-germany.com/uploads/pics/meniscus_start_03

MRI images were first obtained using a 3 Tesla Siemens MRI machine. Bone, cartilage and meniscus geometries were segmented by hand from the MR images using OsiriX software. Furthermore, the fully relaxed position of the silastic tube was recorded via manual segmentation using ITK-SNAP software (Penn Image Computing and Science Laboratory (PICSL) at the Department of Radiology at the University of Pennsylvania).

After MRI scanning, specimens were placed in the WBCT, scanned, loaded, and scanned to acquire the unloaded and loaded positions of each bone (through its marker beads), as well as the position of the meniscal silastic tube. . The knee was loaded to 100 lbs, with load being transmitted vertically through the flexed joint. The magnitude of loading was chosen to produce a contact stress in the knee that would be visible on a Tekscan sensor, while accommodating knees that have undergone significant dissection. [16] In addition to bone marker beads, bone geometries were also segmented and models created for later use. This loaded CT scan provided the source data for meniscal movement, and was performed with use of Tekscan at this stage to capture contact locations and stress levels for comparison to the meniscal DEA model. Methods for obtaining stress measurements are outlined in the next section.

After this meniscal movement scan, a total meniscectomy was performed[3] on each knee and the process for obtaining WBCT scans and Tekscan readings was repeated. Due to lack of complete understanding of meniscal deformability and translational mobility, it was deemed prudent to obtain this data to compare to the simplified cartilage-only DEA model.

[3] Meniscectomy performed by Tyler Stockman by severing ligamentous attachments.

2.2.4 Contact Stress Measurement

The final step in our data collection was to obtain stress readings from within the knee using a Tekscan K-scan sensor (spatial resolution of 62 sensels/cm^2). Prior to any intra-articular data collection, the sensor was calibrated using an MTS loading machine. (Figure 2-5) The loading platen used had a rubber layer to interface with the sensor, preventing sensel damage and more closely simulating the stiffness of cartilage. Research performed by Hartmann, et al. shows that material of lower stiffness is more conforming to the geometric incongruities of the sensor layers. This causes contact area to be larger and not all load to pass directly through the sensing areas of the sensor. [79] A single square area was calibrated from 150 to 900N loads in 150N increments, and a calibration curve was computed for conversion of raw Tekscan values to stress in MPa.

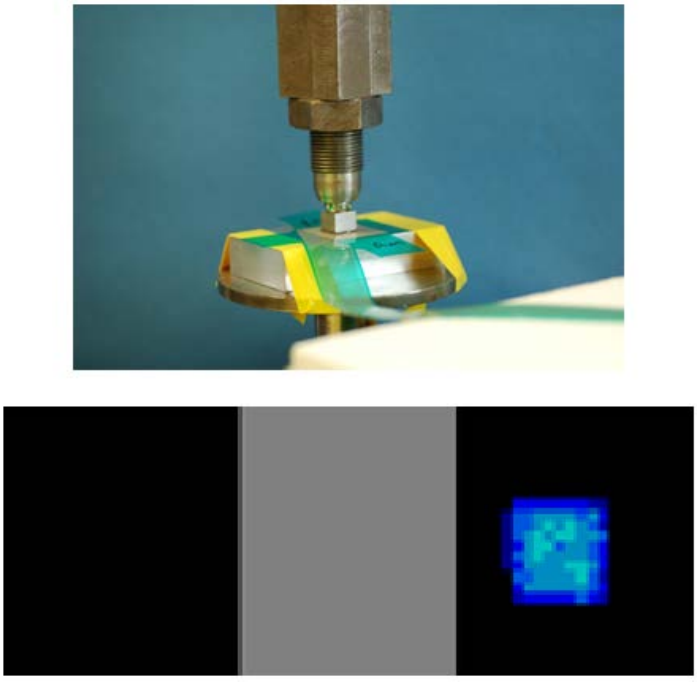

Figure 2-5 – Calibration setup using MTS loading machine (top) and Tekscan K-scan sensor and resulting Tekscan software readout (bottom). Gray space serves to separate readings for each of the two condylar sensors.

The desired location for sensor placement was under the meniscus in order to avoid the potential for wrinkling of the sensor due to condylar curvature. In order to insert the Tekscan sensor under the meniscus, further dissection of the knees was required. First, the menisci for all five knees were released anteriorly and posteriorly to attempt to fit the sensor under the meniscus. However, there was not enough space for the sensor to pass through without severe deformation of the sensels. Therefore, the sensor was coated in petroleum jelly and placed in the joint space between the superior meniscus and femoral articular cartilage, with an effort made to align the sensor's axes to the ML and AP axes of the knees, as well as with an effort to avoid wrinkles in the sensor that might damage it or introduce artifact in the measurements. Dynamic readings from the sensor allowed for optimal placement based on contact location. Each knee in turn was loaded once again to 100 lbs, and the Tekscan sensor was used to record intra-articular stresses. Five frames were obtained for each knee and averaged in order to remove any artifact arising from this dynamic measurement. While under this loading, a WBCT scan was taken to document the loaded positions of each bone (through their marker beads), as well as to localize the Tekscan sensor. The sensor produced a strong enough signal when surrounded by soft tissue to be segmented in a similar fashion as the silastic tubes. The combination of scanner resolution and sensor signal even allowed for the ability to sometimes discern individual sensels from the sensor grid.

Figure 2-6 – Knee in loading frame with Tekscan sensor in joint space prior to loading.

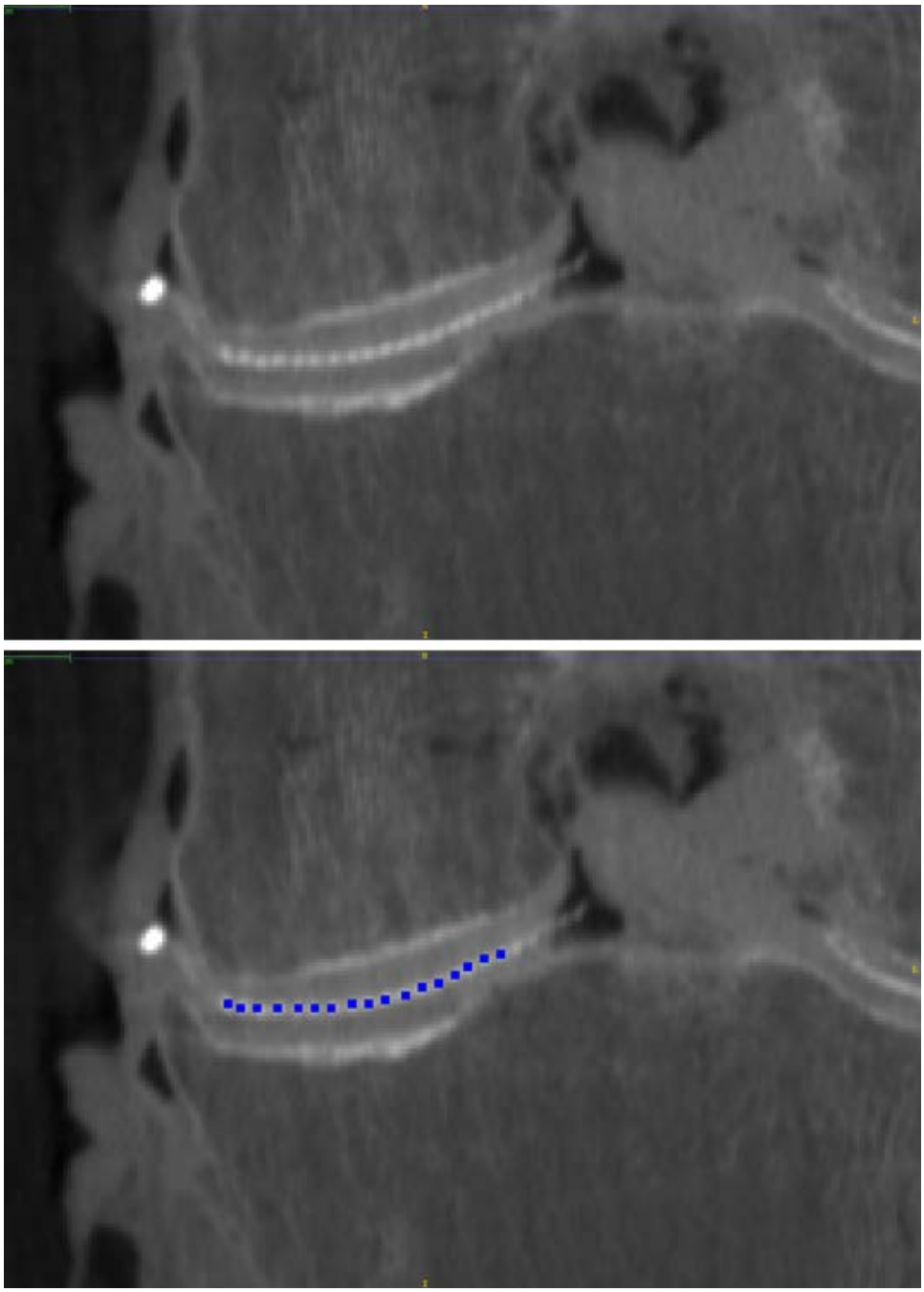

Figure 2-7 – Demonstration of sensor visibility within the WBCT scanner. Original image (top) and individually segmented sensels (bottom).

Figure 2-8 depicts a flowchart of the data collection process for the validation, divided into discrete surgical prep and imaging phases.

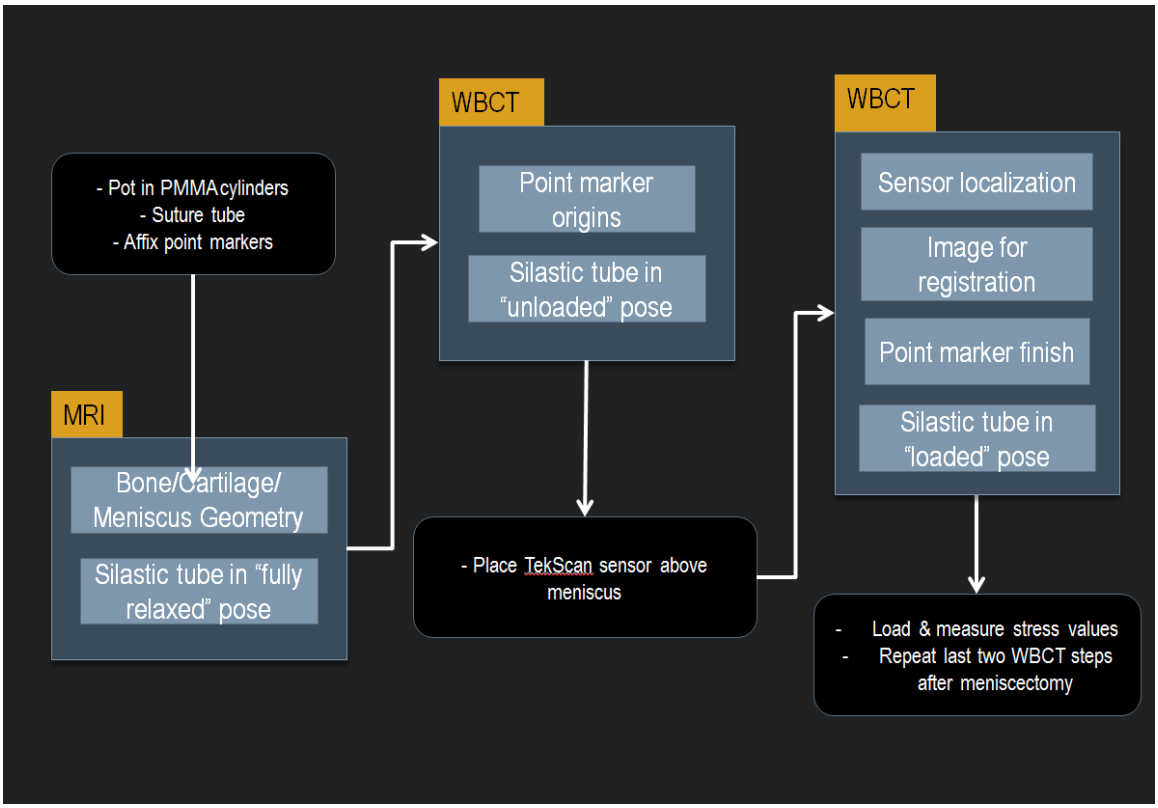

Figure 2-8 - Flowchart depicting the data collection process for cadaveric validation study. Black bubbles indicate manual user input, yellow boxes indicate imaging modality, and blue boxes indicate the information that was obtained at that step.

2.3 Analysis and Processing of Validation Data

2.3.1 WBCT Registration Development

Using WBCT for bone model registration allows for registration of a 3D bone model to up to 360 fluoroscopic images around a knee. Outputs from our prototype WBCT scanner include both raw and reconstructed images. The raw image comes in the form of a DICOM file composed of a stack of images of the specimen taken one degree apart, as the source rotates about the long axis of the frame. It is these images that we register the model to on an individual basis. In order to determine the best views to align the model to, each slice of the raw image can be previewed in a DICOM viewer to choose

those images with little or no obstruction (e.g., due to the loading frame), and clearest bone edges. Since the best possible registrations were desired, six images were manually selected from all 360 for each knee in order to get the best bone edges and minimal obstruction of the knee. Using this many images, registration took around five minutes.

Once the six raw CT (2D) images were chosen, gradient versions of these images were created for the registration procedure. For each slice, a user-defined edge tracing of the bones being registered to was created. These were required to offset the tendency to register to the large gradients created by the loading frame passing through air. These images were created in MATLAB by using methods described previously in section 1.4.2 3D-2D Registration). Within a virtual 3D scene defined by the scanner dimensions and beam path, the 3D bone model position is optimized to each 2D slice simultaneously using the same CMA-ES algorithm that has been used previously for single-plane and bi-planar techniques. [34] A higher cost is associated with larger distance between projective bone model silhouette and the edges detected in the gradient image. The bone silhouette cost for each chosen CT image is computed separately and then summed to give the overall cost function value. From here, the algorithm optimizes to reduce this cost value.

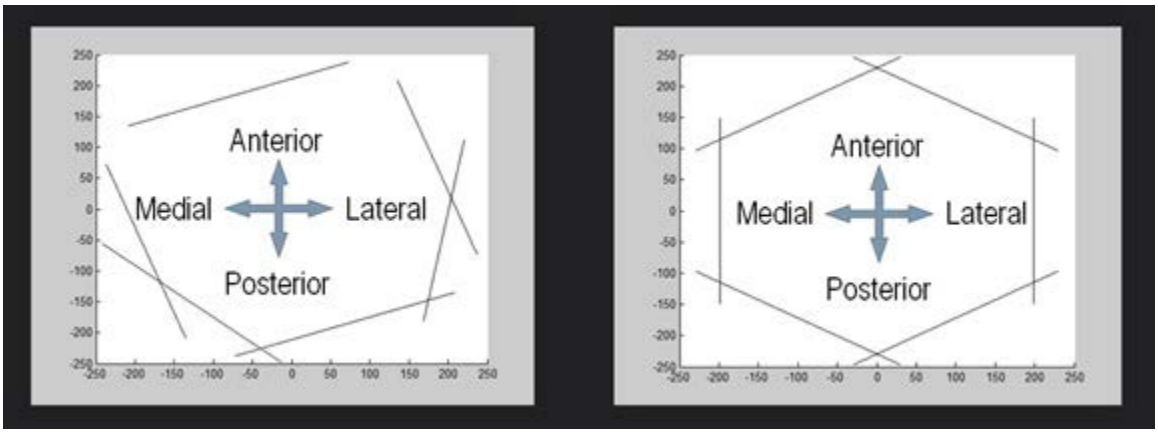

Figure 2-9 – WBCT detector positions from a superior-inferior perspective. Multiple slices can be registered to, which correspond to multiple detector positions. On the left, it is seen that unevenly spaced positions were used for registration to avoid posts of the validation loading frame. On the right is a depiction of equal-spacing positions, which at 60 degree increments essentially results in double registration to three different views. This is because the detector positions are diametrically opposed in three locations.

Figure 2-10 – Comparison of reconstructed CT slice (top) with single fluoroscopic image taken as part of the WBCT scan (bottom). This second image is what is used to compute a gradient image and perform 3D-2D registration.

2.3.2 Validation of Virtual Scene Using Direct Linear Transform

Direct Linear Transform (DLT) is used for tracking rigid body movement across image spaces. The virtual projection scene shown in Figure 2-9 is based upon dimensions of the WBCT scanner. Aside from the overall validation, a DLT was computed by

graduate researcher Steven Long for the scanner, in order to determine the transform from the 2D slice-image space to the 3D image volume. Assuming no image distortion, there exists a linear relationship between the two spaces that can be defined. To make this computation, two different views of the same scene are needed that encompass six reference points of known location in 3D space. To perform the space calibration by DLT, a device was constructed to hold fiducial markers with known centroid locations. These steel beads had a diameter of 6.35 mm and produced a very strong signal in the WBCT scanner. The 2D slice images were converted into edge images using Canny edge detection, and marker beads were discerned using the Hough Transform, as shown in Figure 2-11.

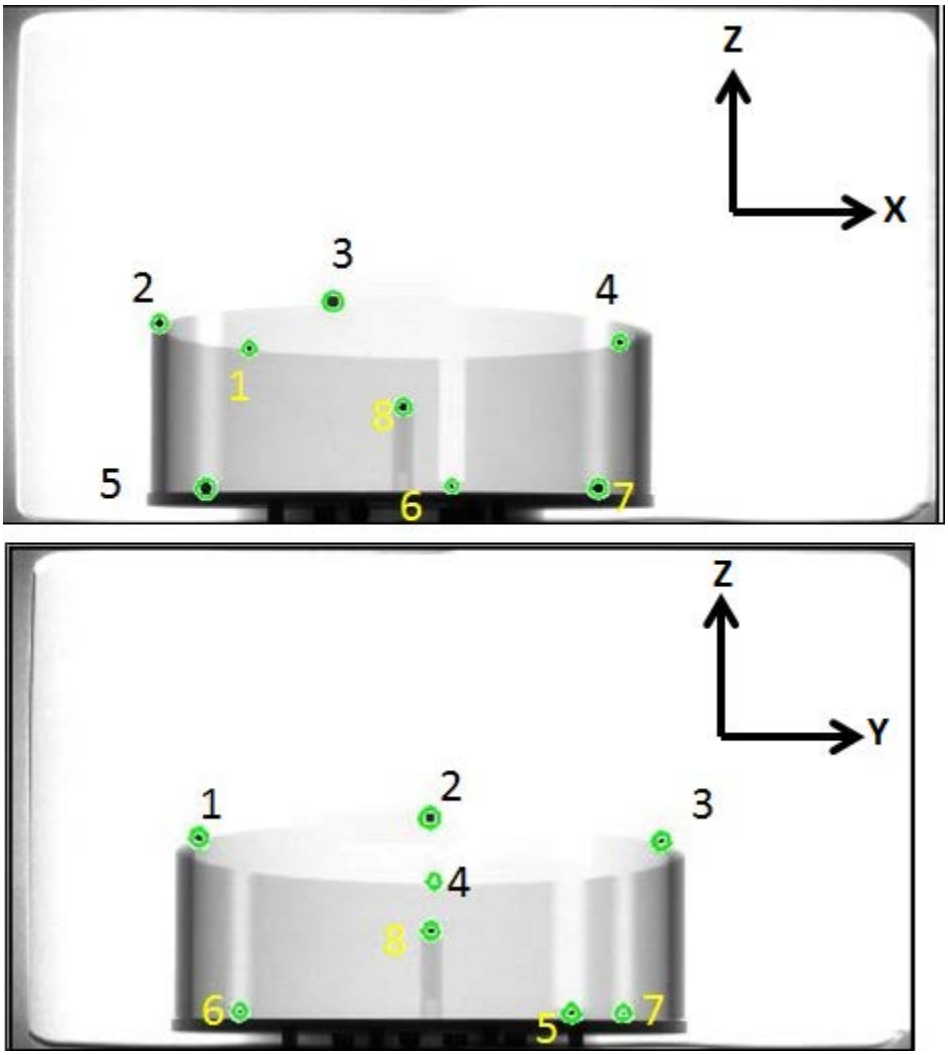

Figure 2-11 – Marker positioning apparatus that sits atop a Melles-Griot tower for translational and rotational movement. The top and bottom views are orthogonal to each other. In the top image, the Y-axis is pointing toward the viewer, and in the bottom image, the X-axis is pointing away from the viewer.

Once the DLT relationship is defined, locations in 3D space can be predicted from a selected point seen in a pair of 2D images. In order for this prediction capability to function at all, the "camera" viewing positions for the prediction image must be the same as the view from which the DLT was computed. Accuracy and image quality of the scanner can be assessed by moving the calibration setup by known amounts (translational or rotational) and attempting to predict the 3D locations from 2D images. To measure this

error, root mean square (RMS) errors were computed between the predicted locations and actual locations after movement.

Using a Melles-Griot tower, the device was translated and rotated in multiple combinations. This type of tower produces precise adjustments to translation and rotation on the order of microns. Specifically, translations are accurate within one micron, and rotations are accurate within 1/60 of a degree. Scans were obtained for translations of 2.5mm in the designated X direction, in the Y direction, and in the Z direction (vertical). Additional scans were obtained after 5° of rotation about the X axis, and 5° of rotation about the Y axis. Predicted locations for markers after these movements were produced using the DLT and compared with the known locations. Figure 2-12 is a graph of the average distance (error) between corresponding marker locations.

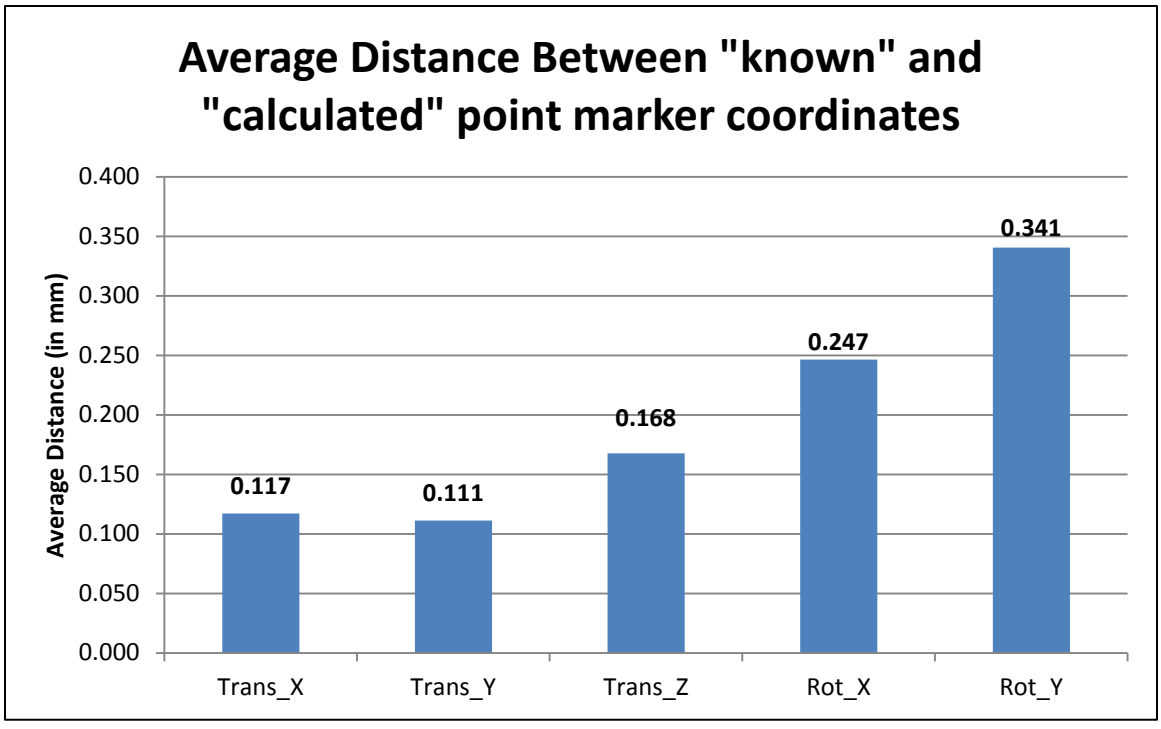

Figure 2-12 – Average Euclidian distance between marker coordinates in “known” and “calculated” positions.

It can be clearly seen that sub-mm errors were obtained, indicating that the DLT is accurate. In such an application, sub-millimeter accuracy is an acceptable and expected amount.

In order to further validate our registration algorithm, a polygonal surface model of the fiducial markers was registered to the CT using the 3D-2D registration algorithm. Multiple neutral position scans were taken to assess repeatability of the registration algorithm. The ability of the algorithm to minimize the distance between the corresponding marker centroids grew when rotations were attempted, but never produced RMS values over 0.5mm.

Table 2-1 – RMS values for marker registrations using gradient images and the CMA-ES optimization method.

RMS Error Values (mm)				
Neutral1	**Neutral2**	**Neutral3**	**Neutral4**	**TransX**
0.000	0.007	0.005	0.007	0.047
TransY	**TransZ**	**RotX**	**RotY**	
0.059	0.069	0.272	0.300	

Further experimentation has yielded higher accuracy of the algorithm when working with translations and rotations of 2.5mm and 2.5°, respectively. The question then arises as to how small the movement must be to obtain the most accurate results. Work by Sharma, et al., from the University of Calgary indicate that use of higher resolution scanners can increase accuracy, which is to be expected. Furthermore, accuracy was seen to degrade at sub-millimeter levels. Movements of 1mm produced very accurate results, but less accuracy was observed at levels below 0.1mm, indicating that there is a limit to how small movements can be to be accurately predicted using the DLT. [80]

2.3.3 Fiducial Registration for Validation

The locations of the fiducial marker beads were obtained from both the unloaded pose and loaded pose WBCT images. Since it is the bone models from the MRI segmentation that are being used to produce contact results, they must first be registered to a load-bearing apposition. In order to assess the validity of the semi-automated registration algorithm, these bone models were first placed at the unloaded CT position by performing a Geomagic best-fit to the unloaded pose bone model. From here, movement of unloaded pose segmented marker beads and movement of MRI bone models can be directly compared. Since segmentations existed for both unloaded and loaded poses, a segmented marker centroid-to-segmented marker centroid analysis of the transformation of these markers between scenes allowed for measurement of the accuracy of our registration algorithm. Marker segmentations for WBCT were performed manually using ITK-SNAP software. Since the marker size (2.1mm diameter) and voxel spacing of the image (0.3x0.3x0.3mm) were known, a single sphere with a diameter of 7 pixels was used to label markers in the CT images.

Once markers were segmented, voxel coordinates were converted to physical space, and the centroid of each bead was computed (for both CT's). The method used to align these marker centroids was Singular Value Decomposition (SVD). This method minimizes the distances between two sets of corresponding marker centroids locations by minimizing the covariance matrix between the two. The fixation method of the fiducial markers supports the assumption that the markers would not move within the bones. Furthermore, bone models were defined as rigid, thus making a rigid transform performed using SVD appropriate. [81]

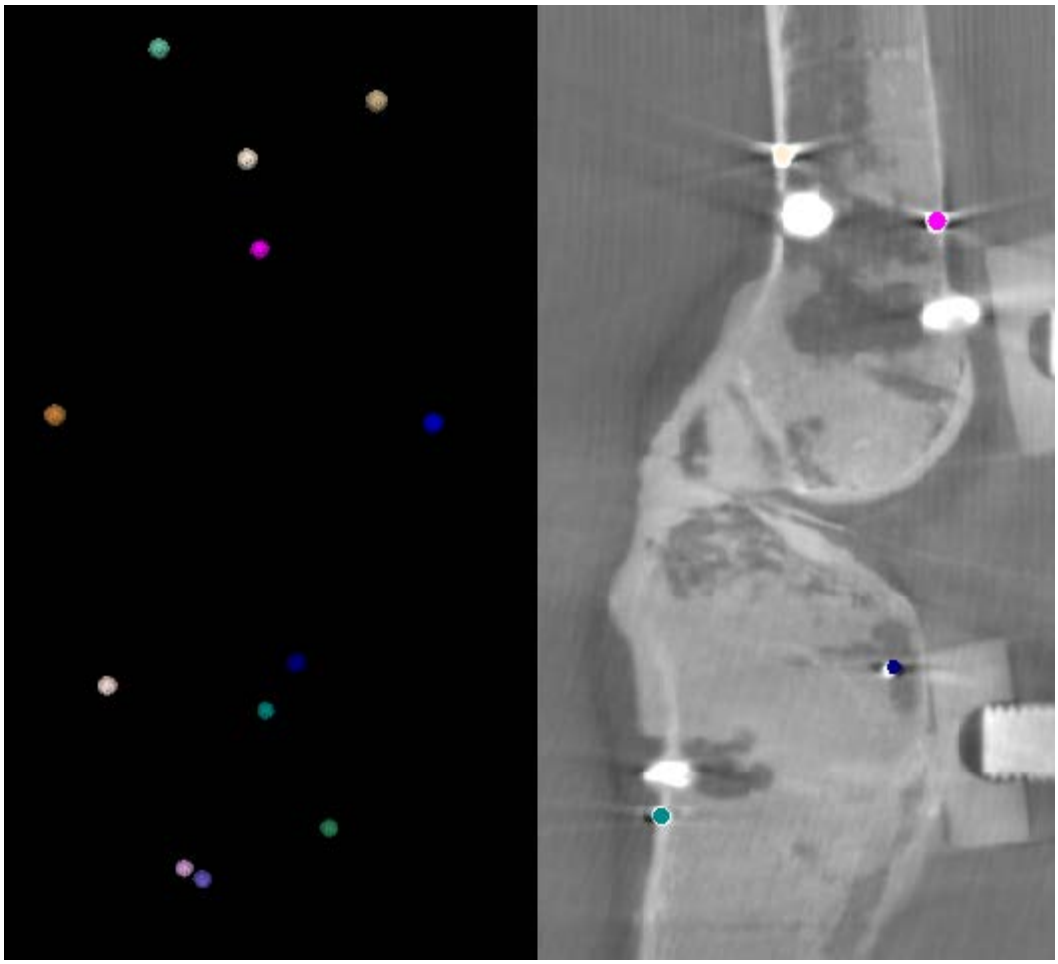

Figure 2-13 – Results of segmenting bone markers from WBCT images. Left shows a 3D visualization and right shows one slice during segmentation. Each marker is assigned a label #1-12 and corresponds to a marker in the MRI image's segmented marker set.

2.3.4 Meniscal Movement Component

Meniscal tube segmentations obtained manually from unloaded WBCT and loaded WBCT using ITK-SNAP software allow for the tracking of meniscal movement under loading. This produced two tube segmentations for each meniscus, hereafter referred to as "unloaded" and "loaded" states. Accounting for both medial and lateral segmentations yielded a total of four meniscal tube segmentations per specimen. A skeletonization algorithm was employed to compute the 3D centerline of each tube from

the resulting meniscal tube segmentations. The algorithm used a multistencil fast marching (MSFM) method obtained from the Mathworks forum (Dirk-Jan Kroon's implementation of work done by Van Uitert, et al., 2007) [82]. This algorithm takes as its arguments the tube segmentation (in the form of a binary voxel mask), as well as a distance field of the segmented tube that evaluates the distance from every point in the tube segmentation to its boundary. From here, the centerline is computed at a subvoxel level, resulting in more precision than frequently used "voxel-precise" skeletonization algorithms. Subsequently, cubic spline curves were fit to each tube centerline, and 100 equally spaced points were interpolated for each medial and lateral tube segment. Therefore, each point along the tube segmentation in the unloaded position has a corresponding point in the loaded position.

The previous step allows for change in length of the tube, as a silastic tube has tremendous deformability. However, the meniscus surface model was being treated as an in-line rigid body for DEA computation, and thus currently can only be transformed rigidly. Using rigid SVD, the best rigid 3D transform for the meniscal tube was computed between unloaded and loaded positions. The majority of the meniscal movement was anterior/radial translation with some rotation and inferior/superior translation aspects. Values for movements are presented in Chapter 3. Rotation about the inferior-superior axis was the only rotation that was not negligible, and was seemingly due to the rigid treatment of the SVD. Application of this type of load-induced transform to a meniscal model in DEA allows for re-positioning of the undeformed meniscus model to its "best-fit deformed *location* under load, although not its deformed *shape*. This skeletonization of tube centerlines is very useful for visualization of tube deformation but is not as useful in *quantifying* it. Vector plots were produced for each knee to get a general feeling for the amount of meniscal movement and deformation. Ideally, a deformed meniscus model could be obtained through segmentation of the loaded image. In this case, the loaded image was acquired using WBCT, which lacks the soft tissue discrimination needed to

accurately identify meniscus and cartilage surfaces. Because the tube deforms and the current DEA model does not include any method for explicitly deforming the segmented meniscus model, a reasonable estimate of the combined meniscal movement/deformation must be chosen based on available measurement methods. Movement of the meniscus for DEA is described in further detail in Section 2.3.6 Meniscal Modeling in DEA Computation).

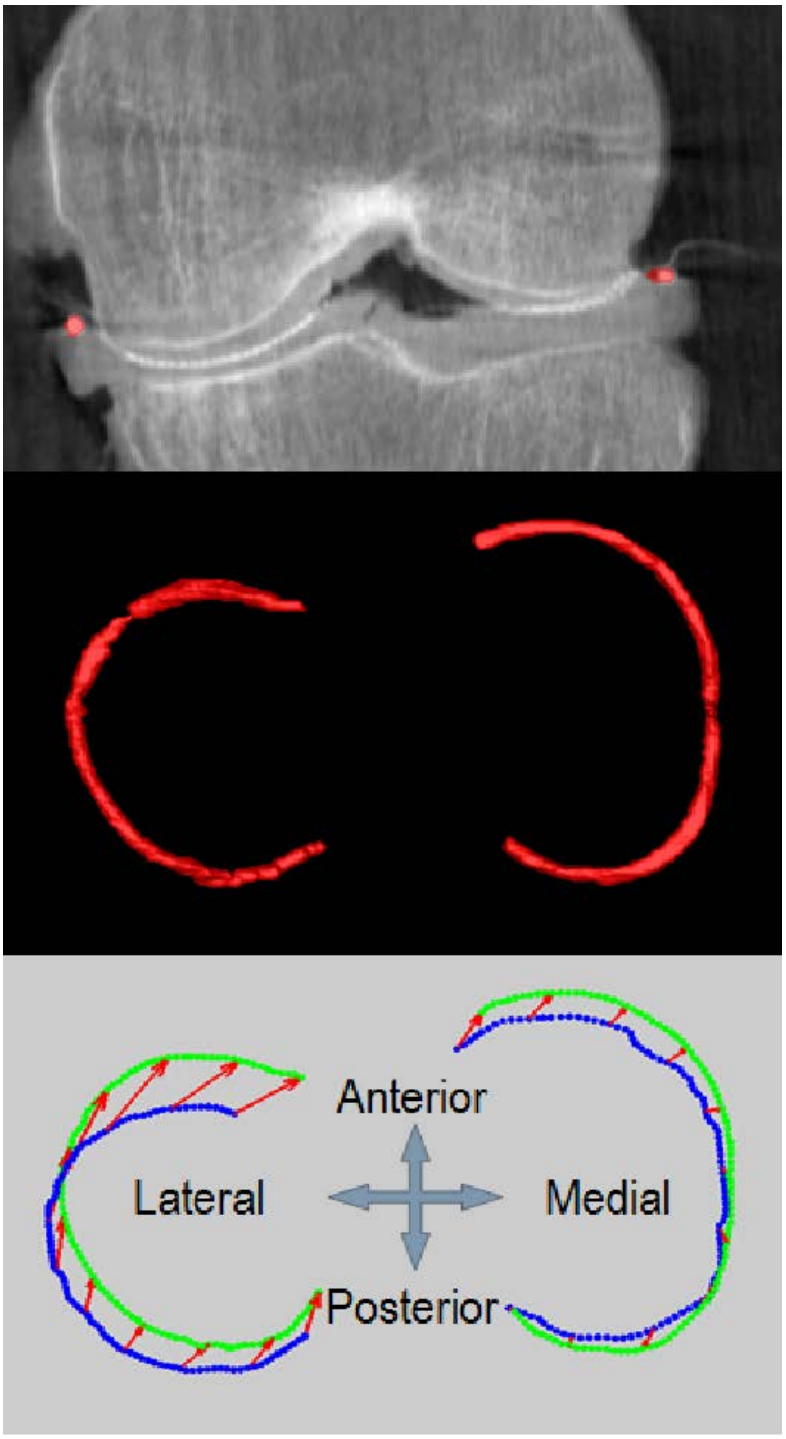

Figure 2-14 – Image of tubes during segmentation in ITK-SNAP (top). Superior-to-inferior 3D view of segmentation of meniscal tubes from loaded CT (middle). A very strong signal was given off by the contrast solution, allowing for accurate segmentations of tubes in unloaded and loaded positions. Tube movement from unloaded (blue) position to loaded (green) position. Point-to-point movement of the meniscus is shown with red arrows (bottom).

2.3.5 Tekscan data processing

The first step in processing the Tekscan readings was to convert all raw values from the sensor to stresses in MPa. This was done using the calibration curve computed before data collection. The result of this conversion was a 22x26 matrix of stress values for each of two condylar sensors, resulting in 1144 sensels for the sensor as a whole. As mentioned previously, the Tekscan sensor had been segmented directly from the loaded CT image. This direct segmentation allowed for visualization of the exact sensor location in relation to the bone/cartilage models and the DEA stress map. Since the number of sensels was known, a grid with this 22x26 element layout was fit to each segmented sensor surface model. Tekscan values were mapped into that grid for visual comparison of Tekscan data to DEA. This mapping to the sensor segmentation is shown in Figure 2-17.

Tekscan readings for intact meniscus and meniscectomy cases are shown in Figure 2-15 and Figure 2-16 . Stress values shown are on a 0-5 MPa scale, and represent the readings before as retrieved from the Tekscan software.

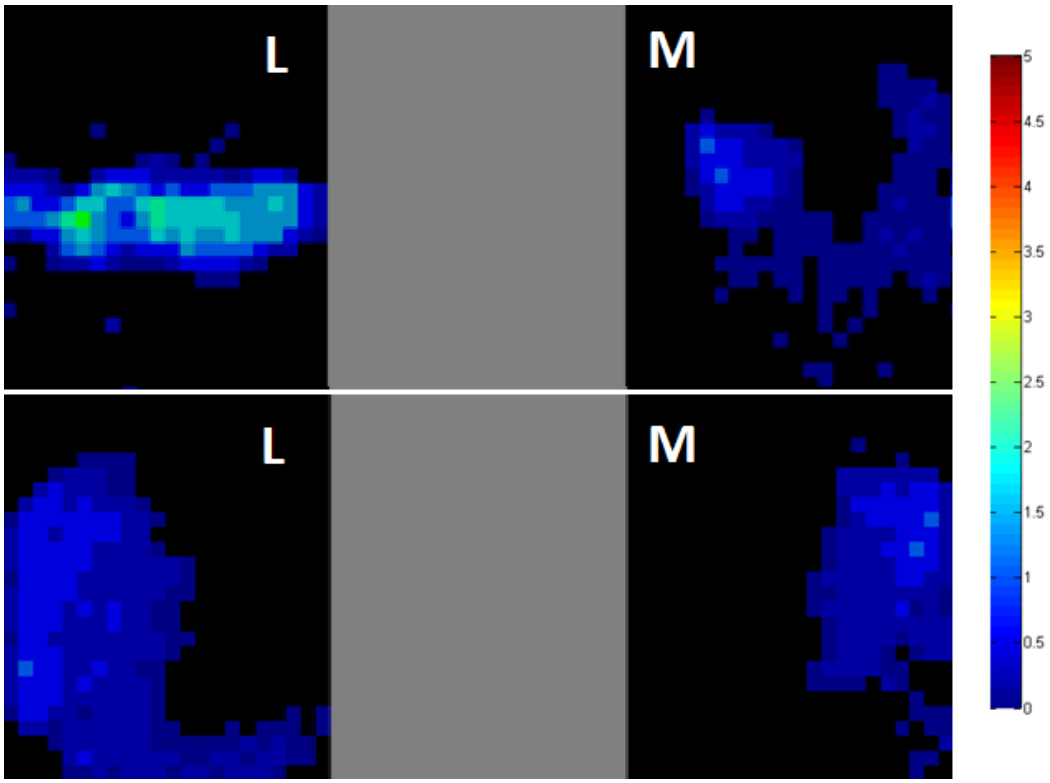

Figure 2-15 – Tekscan readings for knees before performing meniscectomy. Contact patches were much more spread out and indicated lower stress than those readings taken after meniscectomy.

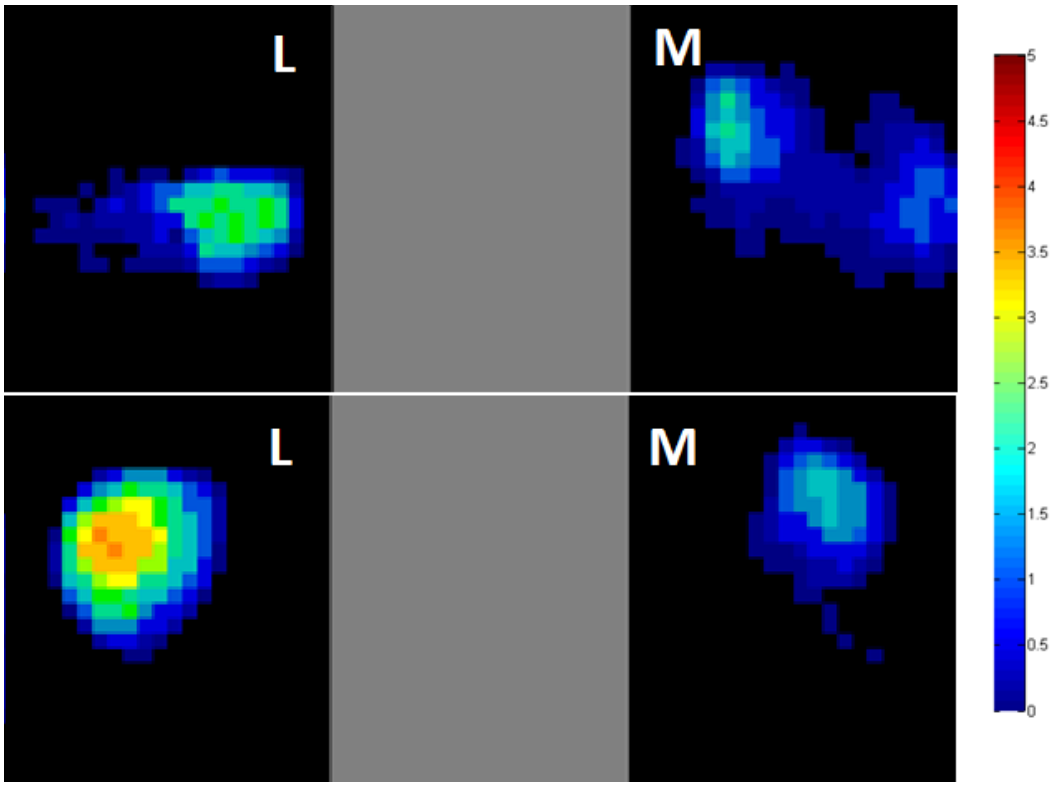

Figure 2-16 – Tekscan readings for knees after performing meniscectomy. Contact patches were much more clearly defined and higher stresses observed than in readings taken with an intact meniscus.

After scaling, the DEA map was then interpolated onto the segmentation of the sensor grid, for direct comparison to the grid output by the Tekscan software. To do this, femoral cartilage facets determined to be in contact with either tibial or meniscal surface models were grouped with other facets based on their nearest neighbor inferiorly/ superiorly on the Tekscan grid. An average value for each group was then assigned to each element of the grid. From the two grids, peak and mean stress values were compared, and difference maps were computed. Interpolations of DEA data onto the sensor grids, as well as the difference maps are shown in Figure 2-18. Lastly, load recovery was examined for Tekscan, as well. With a known load of 100 lbs being applied to the knee, we would expect to see 100 lbs recovered, assuming all load is passing

directly through the Tekscan and the Hartmann effect is minimal. However, contact patches for knees with an intact meniscus showed minor load transfer beyond the sensor boundary, indicating that not all load would be recovered. This outcome could be due to poor sensor alignment within the joint (a particular challenge for Knee 1, as the joint space was very small) or changing contact patches under loading, and this would result in incomplete load recovery. The amount of the contact seeming to be beyond the sensor edges was deemed to be small enough to not play a significant role in load recovery. On a similar note, the Tekscan sensor was observed to degrade in sensitivity over time. In order to address this, Tekscan sensor data were scaled linearly under the assumption that all load passed through the sensor. The usefulness of this step is limited in those contact readings that are not completely on the sensor, but much more helpful in those where contact is clearly centered on the Tekscan sensors. Load recovery and the effects of scaling are discussed in the next chapter.

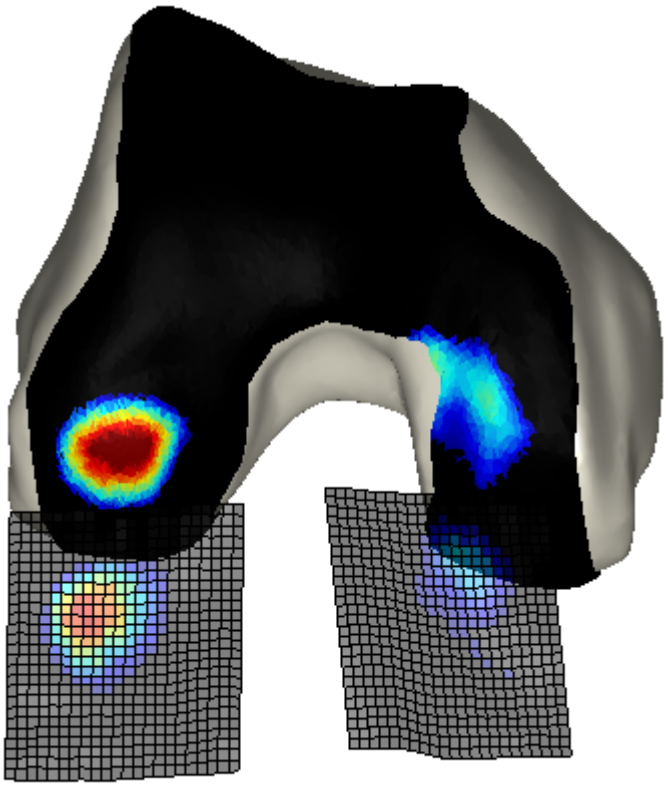

Figure 2-17 – DEA map (on black cartilage surface) plotted with Tekscan sensor grid interpolated from the sensor segmentation (semi-transparent offset from condyles). Mapped onto the grid is the Tekscan data collected during loading. This figure is solely to demonstrate the data mapping that occurred, and does not portray accurate DEA results for this study.

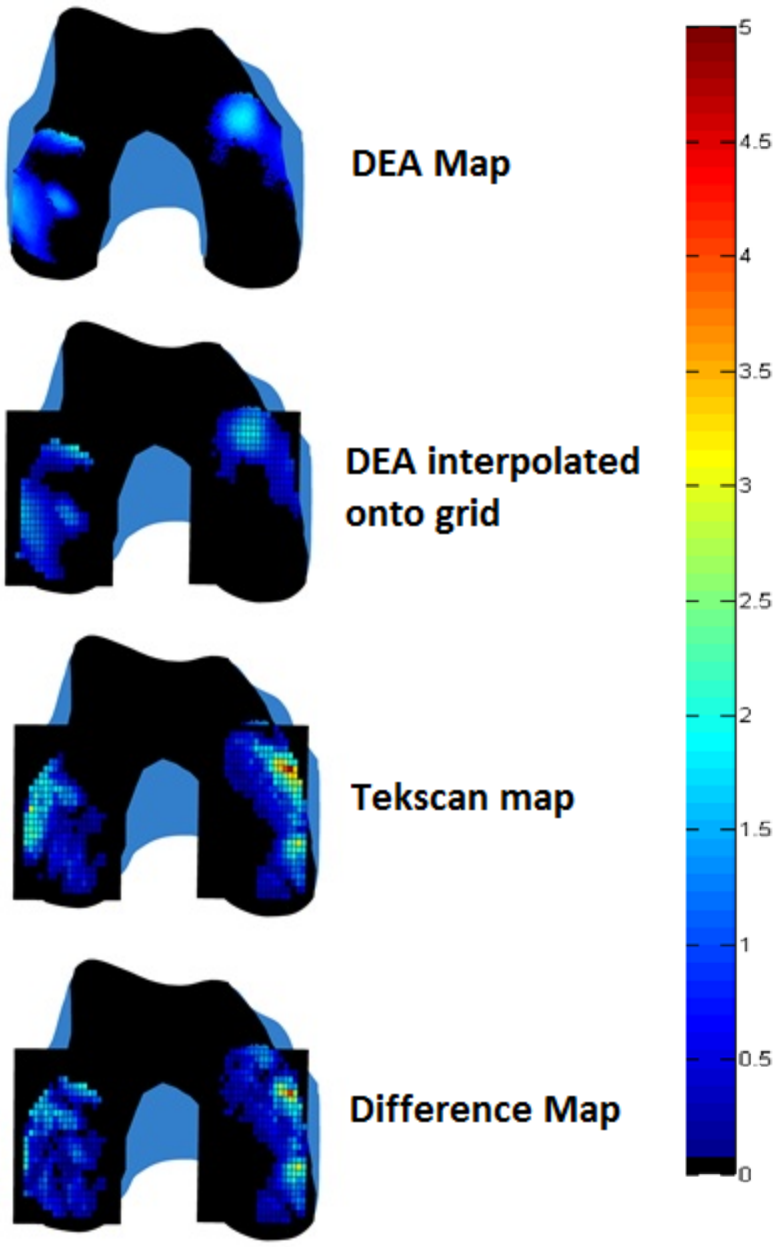

Figure 2-18 – Demonstration of interpolation of DEA values to Tekscan grid, as well as resulting difference map.

2.3.6 Meniscal Modeling in DEA Computation

As discussed in Chapter 1, the meniscus was included in the knee DEA model as an in-line addition to the stress computation. A Young's modulus of 20 MPa and

Poisson's ratio of 0.3 were used in computing stiffness of meniscal thicknesses. [75, 83] Cartilage material properties were E=4 MPa and v=0.42, as described in Section 1.4.3. Also mentioned was the ability of the human meniscus to translate substantially under load, mainly anteriorly with some radial deformation. Initially, DEA was run without moving the meniscus at all to gain insight as to how much the rigid meniscus models would need to deform to obtain readings comparable to those measured by Tekscan with an intact meniscus. These stress maps are shown below in Figure 2-19.

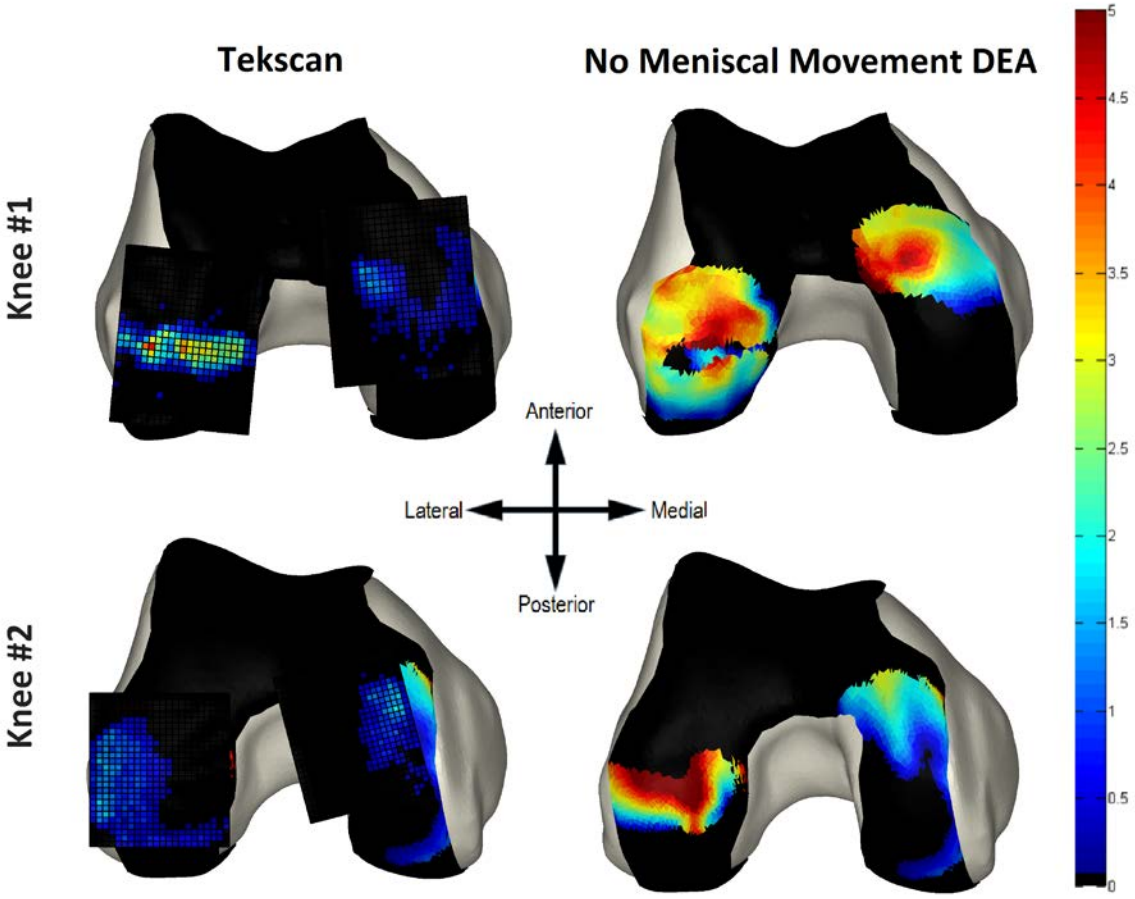

Figure 2-19 – Comparison of Tekscan data with intact meniscus (left) and DEA maps using a no-meniscal movement approach to meniscal modeling.

Results comparing DEA with no meniscal movement to Tekscan from intact meniscus readings showed no qualitative relationship. If considered in the context of tube movement (which was found to be mainly anteriorly translational), it can be expected that the posterior aspect of a rigid meniscal model's superior rim will be pulled anteriorly and contact, thus creating large amounts of overclosure and inaccurate stress results.

Based on these observations, the evident next step was to incorporate motion in the meniscal modeling. To attempt to accommodate some of this movement (still in a rigid manner), using SVD as previously discussed, the meniscal tube movement was tracked and recorded in terms of a 4x4 roto-translation matrix. Using this information, the meniscus model can be moved accordingly in the DEA computation. This placed the undeformed meniscus in its "best fit" position based on the loaded tube position. Because the tube was attached to the superior rim of the meniscus, the tube was in fact measuring this movement, and not the overall deformation.

Once fiducial and 3D-2D model registrations were obtained for each knee specimen, DEA was run for the knees in displacement control for both 3D-2D registrations and fiducial registrations in both intact meniscus and meniscectomized scenarios. Assuming that registrations were perfect, displacement control would be expected to place the bone models in their exact physical-space position during loading (as defined by the final WBCT position), and result in the best measure of cartilage and meniscal overclosure. Likewise, assuming 3D-2D feature-based registrations were perfect, we would expect to see the exact same DEA result for fiducially registered bone models and feature registered bone models.

The four cases described previously (fiducial/3D-2D x intact meniscus/no meniscus) were run in order to examine the effect of feature-based registration error on DEA contact stress values and contact areas. Maximum and mean contact stress values were recorded for each DEA model, and are reported in the results section. In addition to contact stress information, the total load recovered in the DEA was calculated. The

contact stresses and areas of each element in the DEA determined to be in contact were known, and using this information the load on each element was computed. When running DEA in displacement control, the load recovered is based purely on the registered location of the bone models, and how much cartilage-cartilage and cartilage-meniscus overclosure there is. If applying 100 lbs to the knee in the frame, it would be expected to see ~100 lbs recovered from the DEA stress map in displacement control.

CHAPTER 3: RESULTS & DISCUSSION

3.1 Registration

3.1.1 Fiducial Registration and Error

Several types of error are seen when performing a rigid marker-based registration. First, fiducial localization error (FLE) is seen based on how well the user can locate the marker beads. FLE is defined as the root mean square (RMS) distance between the user-defined marker center and actual marker center. FLE is generally treated as negligible under the assumption any errors in localization are small in comparison to those involved in pose-to-pose model-based registrations.

Because one imaging modality was used to obtain the fiducial marker segmentations, one could expect less variance of FLE than when using multiple modalities. If the markers are identified consistently across images, FLE will be consistent, but not necessarily zero. If assumed to be zero, what little FLE exists is manifested as higher apparent fiducial registration error, which is discussed next.

Fiducial Registration Error (FRE) is the second type of error, and it is defined as the RMS distance between corresponding points (registered and registered-to) after registration. The fiducial SVD registration used should produce the most accurate transform for registering the 3D model to the 2D CT slices, and it provides a gold standard against which to compare our 3D-2D registration algorithm. Sources of this type of error include FLE, as well as any unintended movement of markers after implantation. Marker movement should not be a factor, but if fixation technique is not precise for each subject, it can provide altered marker spacing between images. If detected inter-marker spacings are consistent between corresponding marker centroid sets, this would suggest that the markers did not move between sequential image acquisitions.

The last type of error that can be observed is called Target Registration Error (TRE). It is defined as the distance between corresponding points after registration, when

the points are not fiducial markers per se. This error reflects the distance between something such as bony landmark locations, or perhaps the difference in registered and registered-to marker centroid clouds. In our case, the most relevant error to examine is this TRE, since our intended applications all use model-based target registrations. A diagram of error types is shown in Figure 3-1 (image from Fitzpatrick et al., 2001). Once we had our model-based 3D to 2D registrations and fiducial registrations, we computed the error between the two registered marker centroid sets. This measure indicates how accurately our registration algorithm predicts the loaded position of the bone model. RMS error values were calculated for both FRE and TRE and examined. [84-87]

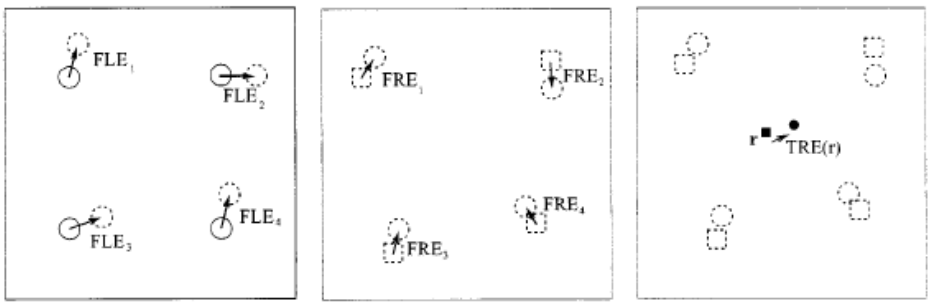

Figure 3-1 – Depiction of the various types of error seen when performing a rigid point-to-point registration. Such a rigid transform is performed during singular value decomposition.

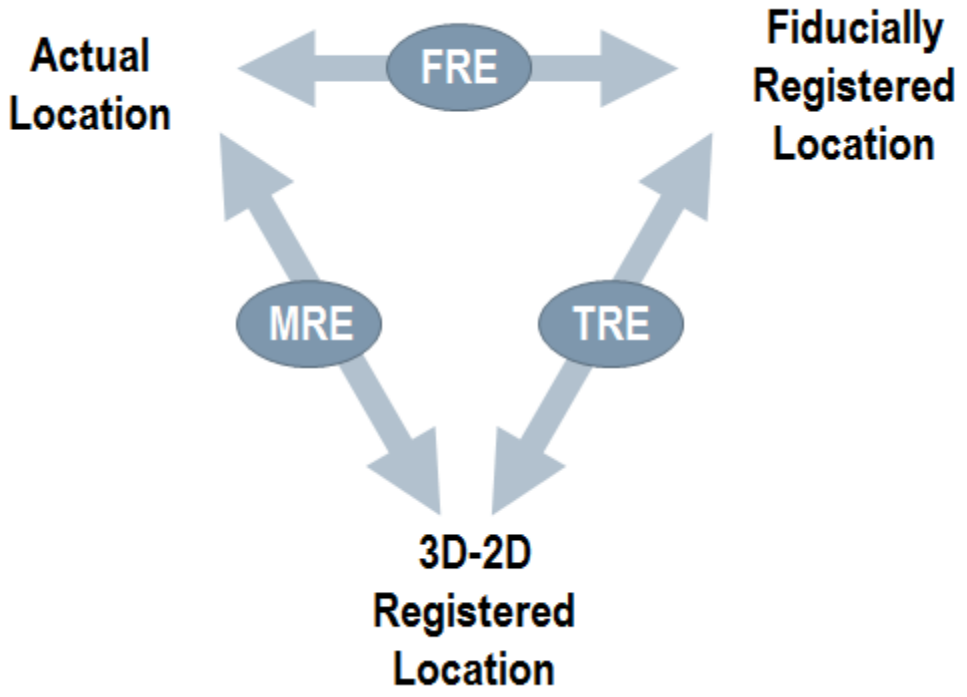

Figure 3-2 – Relationships between point locations and types of error.

The values obtained for FRE are expected to be relatively small if the FLE is minimal and assuming the bones move rigidly. Assuming the marker spacing is consistent across imaging modalities, the FRE should be nearly zero. If any amount of bone flexure is occurring during loading, this can also contribute to FRE. Bone flexure is assumed to be zero, but might be measured by producing deviation maps to show differences in bone shape for unloaded and loaded bone models. Cursory analysis of bone flexure by creating Geomagic deviation maps between models was performed that indicated average deviation values between surfaces of 0.1 - 0.2mm. This is potentially enough flexure to affect FRE results. For registrations such as these, even millimeters of error can cause substantial changes in DEA computed contact stresses in the knee model, since the cartilage is only a few millimeters thick. In this case, it is desirable to have sub-

millimeter accuracy. An error of 0.3 mm would indicate average segmentation error of one voxel. Segmentation methods being consistent between scans, a few voxels difference may not be noticed to the naked eye. It is for this reason that care must be taken to carefully define and utilize consistent segmentation methods. All of the errors measured fall into this sub-millimeter category. Therefore, errors from fiducial marker segmentation difference or changes in contact shape are minimal, and should thus have minimal effect on contact stress estimates.

Table 3-1 presents FRE values for the validation knees. Values average 0.44mm RMS error, and are generally higher for the femur. If flexure plays a part in these error values, the femur could potentially be affected more by flexure, as more femur bone was available for flexing. Equation 3 below defines how calculation of the RMS error is performed to obtain fiducial registration error types. The error is computed by taking the square root of the average squared distance between corresponding point sets (x_i and y_i) after applying the fiducial rotational transform (R) and translational transform (t). N represents the number of points in each point set. This example is for FRE, but other error types are computed in the same fashion.

$$FRE^2 \equiv \frac{1}{N}\sum_{i=1}^{N}|Rx_i + t - y_i|^2$$

Equation 3 – Equation for computing the FRE. The RMS is taken for each corresponding point pair and averaged across the point set. (Taken from Fitzpatrick et al., 1998)

In the same method as FRE and TRE are computed, we can also create a measure of how close the 3D-2D registration algorithm gets to the actual location segmented from the WBCT. Thus in the way that FRE measures closeness of the fiducial transform, this

measure, referred to hereafter as Model Registration Error (MRE), measures the closeness of the 3D-2D transform.

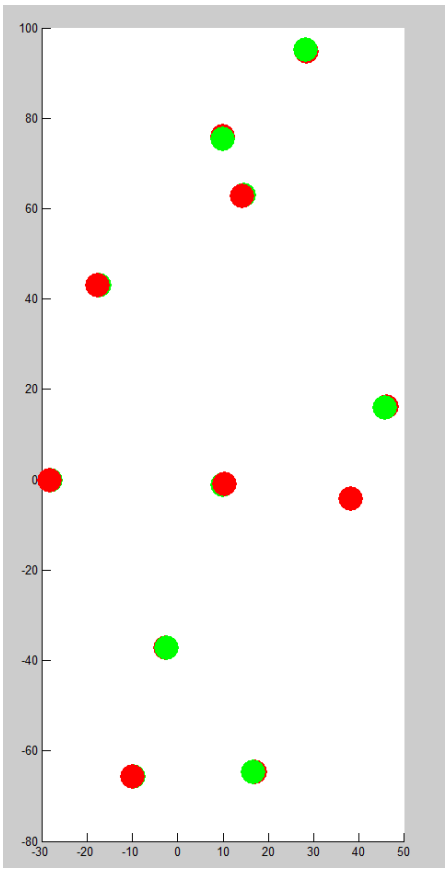

Figure 3-3 – Fiducial marker centroids for Knee 2. Red indicates the fiducially registered centroids, and green indicates the centroids being registered to (loaded position).

Table 3-1 – FRE values (in mm) for validation registrations.

Fiducial Registration Error (mm)				
	Knee 1		Knee 2	
	Meniscus	No meniscus	Meniscus	No meniscus
Femur	0.48	0.62	0.37	0.64
Tibia	0.33	0.29	0.38	0.44

3.1.2 3D-2D Feature-Based Registration

The3D-2D model registrations run in a mostly automated fashion, but they are not deterministic. This means that sequential runs can yield different final registrations. The results of each run were judged as either acceptable or as needing a re-run of the registration algorithm based on visual inspection of the closeness of the bone model silhouette to the bone edge in the WBCT images used for registration. Assuming that the bone model geometry closely matches that of the actual bone, these silhouettes should in theory be capable of reaching a pose that perfectly matches the edges of the bone in the WBCT scan. Figure 3-4 shows one of the 360 single-degree-separated projection images obtained using WBCT after it was converted to a gradient image for registration. This type of visualization is used for determining 3D-2D registration acceptability. A 3D-2D registration silhouette is shown alongside its fiducially registered counterpart to emphasize the subtle differences between the two. Both of these would likely be considered acceptable if produced on different runs of the registration algorithm.

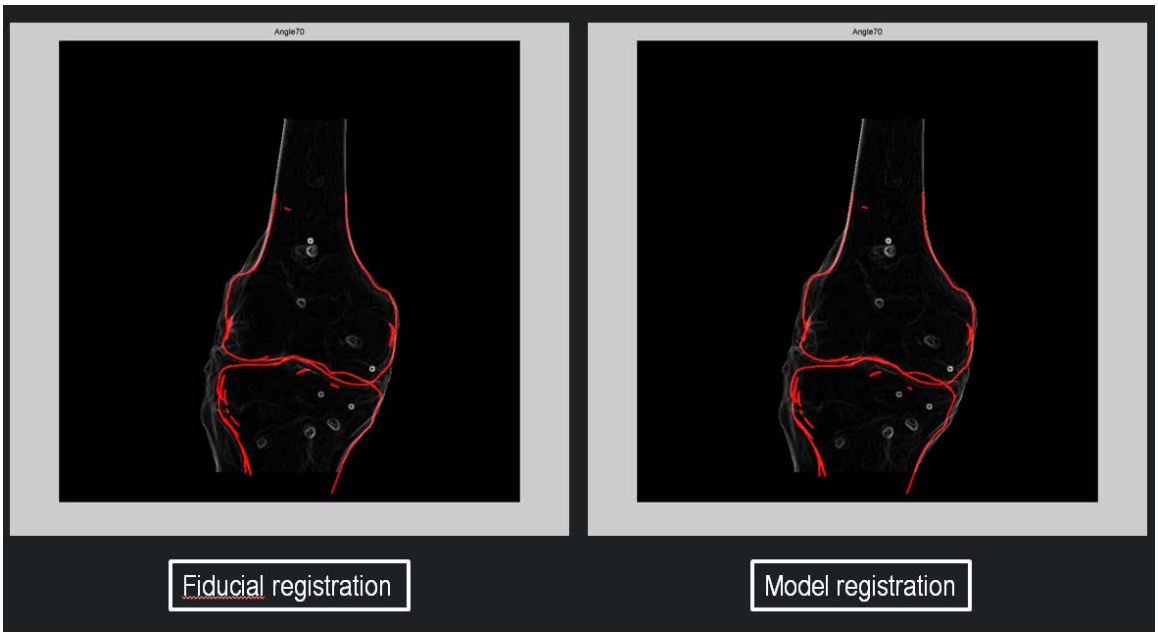

Figure 3-4 – Comparison of feature-based model registration silhouette to fiducially registered model silhouette. Registration acceptability is determined by examining images such as these, to find those with best agreement between silhouette and radiographic bone edge.

The spatial transform computed to move the bone model from MRI to WBCT space is recorded in the form of three translations and three rotations (x,y,z). Fiducial registrations provide the gold standard registration with which we can work toward DEA results. Fiducial registrations using SVD are recorded in the form of a 4x4 roto-translation matrix. Due to the difficulty of comparing these transforms directly, comparison can be made through the measurement of target registration error (TRE). Marker centers for the tibia and femur are each transformed by their fiducial and model registration, and lastly the RMS distances between corresponding markers is calculated between the two positions. TRE values shown below in Table 3-2 indicate that the model-based 3D-2D registration produced results that average within 0.8mm Euclidian distance of the fiducial “best possible” registration. Based on the argument presented earlier pointing out the impact of the image resolution on segmentation accuracy, this

error was deemed acceptable. The effect of this distance on contact is arguably more pronounced if errors are normal to the joint surface, although the largest error was manifested through rotation about the superior-inferior axis.

Table 3-2 – TRE values (in mm) for validation registrations.

Target Registration Error (mm)				
	Knee 1		Knee 2	
	Meniscus	No meniscus	Meniscus	No meniscus
Femur	0.39	0.43	0.72	0.49
Tibia	0.42	0.46	0.44	0.37

Because the values computed for TRE are very similar to those for FRE, it stands to reason that differences in the DEA-computed contact stresses will be minimal when comparing results for the two registrations. One mal-aligned marker can affect TRE values substantially, even if the rest have a fairly good fit. Even a slight adjustment to the 3D-2D registration could dramatically affect the error value. These TRE values are in essence a direct reflection of the accuracy of the current 3D-2D registration algorithm. It should be noted, that in the DLT computation, results were reported stating that this method is inherently very accurate. This accuracy of the DLT algorithm may be facilitated in part by the use of very regularly shaped objects (metal spheres). As a consequence, there is negligible ambiguity in visual assessment of model alignment. When registering the irregular shapes produced by projection of a bone model silhouette, more room for error exists. Furthermore, quality of WBCT scans was seemingly affected by the removal of soft tissue around the cadaveric knees, the thought being that x-ray beams over-penetrated the specimen, making bone edges more difficult to discern. The implementation of user-defined bone edge tracings provided the remedy for registration to sections of bone exposed to air, providing a gradient to register to these locations. For

each slice, extraneous gradients from the loading frame or Tekscan shoe cord were meticulously cropped out to avoid registration to these items. Effects of TRE error on DEA stress maps are examined later with the stress computation results.

Lastly, the computed Model Registration (MRE) measures the average distance from registered position to actual after applying the 3D-2D registration. These numbers are slightly higher than those found for FRE, meaning that the registration placed the marker centers slightly further away from the actual location. Intuition would suggest differing contact results between the two registration methods, but these differences are minimized with lower TRE.

Table 3-3 – MRE values (in mm) for validation registrations.

Model Registration Error (mm)				
	Knee 1		Knee 2	
	Meniscus	No meniscus	Meniscus	No meniscus
Femur	0.61	0.76	0.75	0.72
Tibia	0.53	0.54	0.58	0.63

3.2 Meniscal Movement

Recall that each meniscal tube centerline was divided into 100 discrete points for examination. Due to the assumption that what meniscal movement occurs under loading is primarily translational, we initially gauged movement of the entire meniscus by only the translational components of our SVD measure. In Table 3-5, translational movement values for the menisci are given for all knees. These values are computed by taking the average of translational movements for each of the 100 point-to-point comparisons. Even more indicative of the movement are the images shown in Figure 3-5 and Figure 3-6 that depict the movement of the tube centerline. It can be seen that the meniscal tube (superior rim) moved primarily anteriorly, with some radial expansion. In the first figure, tube

centerline movements are shown from fully relaxed-pose in the MRI (20 degrees of flexion) to loaded WBCT pose (~15 degrees of flexion). Due to this change in knee flexion, some of the meniscal tube movement may be attributed solely to flexion of the knee. In the second figure, tube centerline movements are shown from unloaded pose to loaded WBCT pose. These comparisons will allow for better understanding of meniscal movement due to knee extension plus loading (Figure 3-5), and meniscal movement due solely to loading of the knee in the same amount of extension (Figure 3-6).

Once again, it should be noted that such a characterization of the movement does not capture deformation of the tube, only general movement direction.

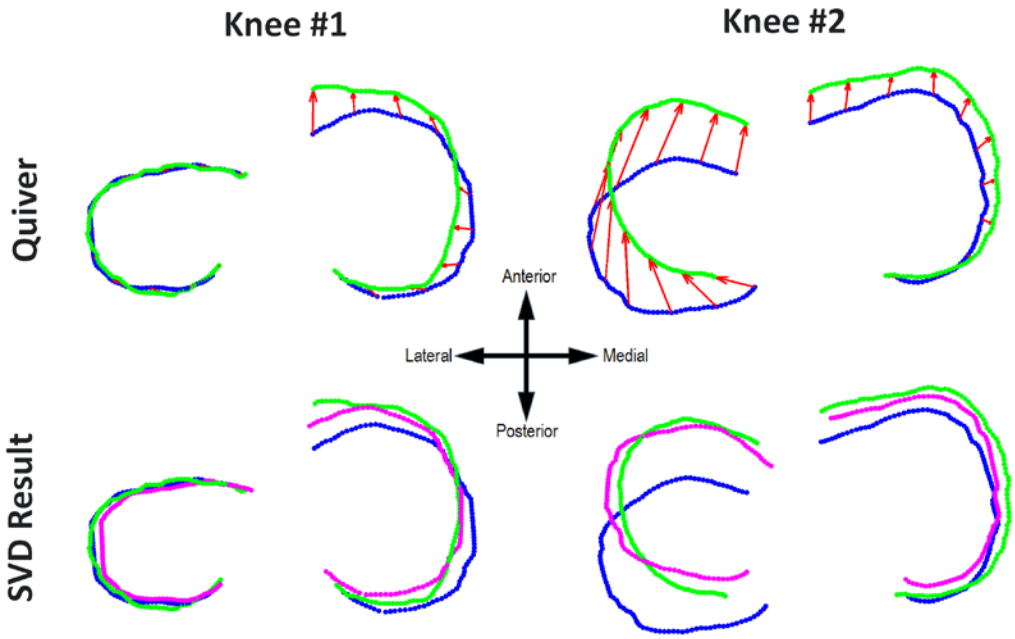

Figure 3-5 – Depiction of meniscal tube movement from fully relaxed to loaded position (top row) and resulting meniscal placement after SVD registration of centerlines (bottom row). All images depict a inferior-superior view. Tube centerlines were discretized into 100 points along their length and the point to point movements were analyzed. Blue indicates the relaxed meniscal position and green indicates the loaded position. Arrow vectors are included to show the general movement along the length of the tube centerline. Pink indicates the resulting meniscal placement through display of its centerline.

Table 3-4 – Meniscal excursion values from fully relaxed (MRI) position to loaded position in the WBCT.

Meniscal Movement Values – Fully relaxed to Loaded (mm)		
	Knee 1	Knee 2
Medial – ML	-1.86	0.87
Medial – AP	0.30	2.61
Medial – IS	-1.77	-3.14
Lateral – ML	2.27	0.99
Lateral – AP	2.76	13.59
Lateral – IS	-2.55	-4.37

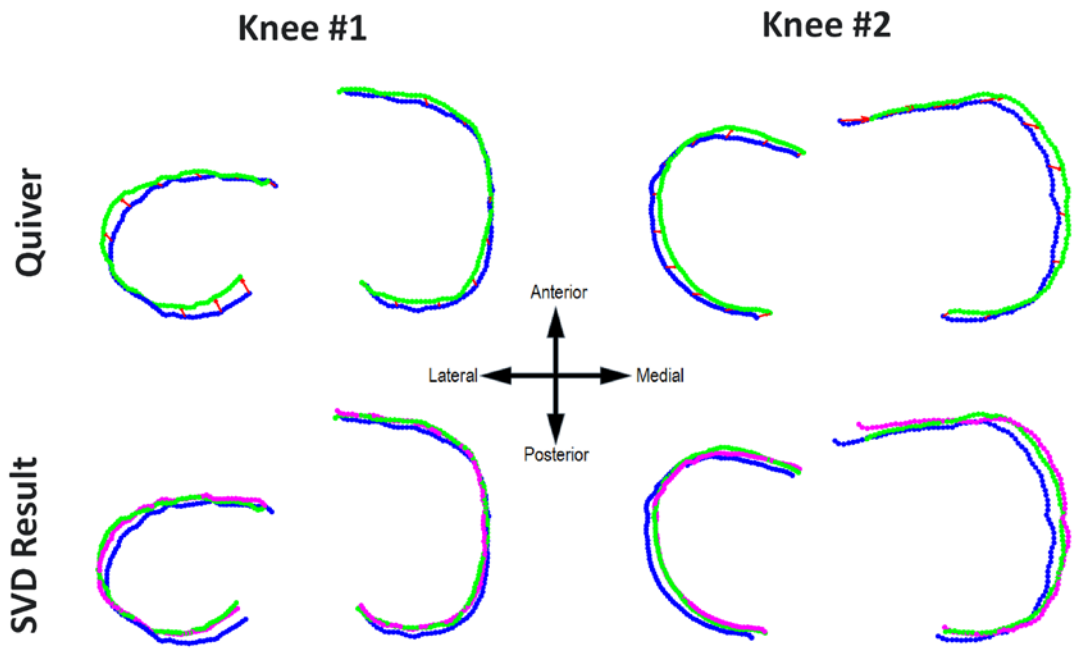

Figure 3-6 – Depiction of meniscal tube movement from unloaded to loaded position (top row) and resulting meniscal placement after SVD registration of centerlines (bottom row). All images depict a inferior-superior view. Tube centerlines were discretized into 100 points along their length and the point to point movements were analyzed. Blue indicates the relaxed meniscal position and green indicates the loaded position. Arrow vectors are included to show the general movement along the length of the tube centerline. Pink indicates the resulting meniscal placement through display of its centerline.

Table 3-5 – Meniscal excursion values from unloaded position to loaded position in the WBCT.

Meniscal Movement Values – Unloaded to Loaded (mm)		
	Knee 1	Knee 2
Medial – ML	1.46	3.32
Medial – AP	1.49	0.57
Medial – IS	-0.97	-2.14
Lateral – ML	0.57	1.82
Lateral – AP	1.44	0.66
Lateral – IS	-0.97	-0.86

Amounts of the entire tube centerline translation are shown in Table 3-4. Values are computed as a component of a 3D transform computed using SVD. Positive AP values indicate anterior movement, and positive ML values indicate medial movement of the tube centerlines. Positive IS values indicate superior movement of the centerlines. The amounts of anterior translation of the meniscus are comparable to findings of Vedi, et al. (1999) in living subjects. Maximum anterior translation in the validation was 13.59 mm in the lateral compartment for Knee 2. In a completely extended, weight-bearing knee, Vedi saw an average of 9.5mm anterior translation of the anterior horn of the lateral meniscus in 14 male volunteers when standing and flexing their knees to 90° of flexion. [76] Also reported were changes in height of the anterior and posterior horns of the menisci between relaxed-flexed and loaded-extended appositions. Such horn height changes were between extremes of 2.0 and 4.0 mm, averaging between 0.95 and 1.75 mm. Preparatory release of the anterior and posterior meniscal horns likely contributed substantially to meniscal movement, as up to 13mm of anterior meniscal excursion was seen in knees in near-full extension. Measurements were obtained in using an open MRI machine for a load-bearing full extension pose as well as a sitting non-weight bearing pose. Results for this study are more clearly depicted in Figure 1-14. Data obtained in order to track meniscal movement during validation was compared to the findings of Vedi, et al., indicating the need for a meniscal position somewhere between un-moved and SVD. Based on manual movement results described later in this paper, a best-possible meniscal contact scenario does exist, but lies in between other options.

Meniscal tube length was also monitored from unloaded to loaded positions. Given the centerline of each, the arclengths could be computed and compared. Results for tube length measurements are given in Table 3-6.

Table 3-6 – Tube length between unloaded and loaded conditions.

Tube Length Measurements (mm)						
	Knee 1			Knee 2		
	Unloaded	Loaded	Expansion	Unloaded	Loaded	Expansion
Medial	77.1	84.5	+7.4	85.8	94.5	+8.7
Lateral	85.1	86.6	+1.5	81.5	82.3	+0.8

It can be seen from these tube measurements that the tube lengthened up to 8.7mm under loading, indicating radial expansion of the superior rim of the meniscus. Once again, this does not indicate the overall deformation, but provides a useful tool in examining the shape change of the superior rim of the meniscus. If nearly a centimeter of lengthening occurs, the contact area and contact location radius of curvature are almost certainly changing.

The chosen best option for rigid meniscal movement in DEA was the 6 DOF movement afforded by rigid SVD. It is possible to perform point-set registrations using a deformable method, and this would provide a more accurate registration of unloaded tube to loaded tube. However, since radial meniscal deformation was not in the DEA formulation, the shape of the meniscal model stays the same as segmented, and its loaded location is determined by obtaining a best-fit for the undeformed meniscal tube geometry to that of the loaded meniscal tube. This method is clearly not sufficient for providing definitive meniscal movement, as it is generally used for movement measurement of rigid bodies. For menisci in which minimal deformation occurred, it is quite reasonable to use this method, although minimal deformation was seen very infrequently.

In some cases (e.g. lateral Knee 2), movement of the meniscal tube represents internal rotation of the meniscus. The resulting placement of the undeformed meniscus model is then much nearer to the tibial spine than might be expected under load. This is a

limitation of using the rigid SVD method to measure a more complex movement/ deformation. Meniscal movement effect on DEA results is discussed in the next section.

3.3 DEA Contact Stress Computation

DEA contact stress results were obtained in displacement control for both knees for four different loading/registration combinations (no meniscus/meniscus, fiducial registration/3D-2D registration). Over the course of repeated data acquisitions using the Tekscan sensor, a linear degradation of sensitivity was observed. In order to accommodate this degradation, the remaining Tekscan maps were scaled to 100 lbs of recovered load. This is based on the assumption that all load applied to the knee passed through the sensor during measurement. From visual inspection, it is seen that most or all of the loading is within the boundaries of the sensor, thus making a scaling like this reasonable. It is the scaled data that were examined alongside DEA contact maps for all loading and registration conditions in the following sections. Much of the data presented hereafter will be reported in tables and supplemented with images for demonstration.

3.3.2 DEA Results – Intact Meniscus

DEA results for validation knees with *intact* menisci are discussed in this section. Run in displacement control for both fiducial and 3D-2D registration methods, this DEA produced contact patches with larger contact area and lower stress levels. Methods for meniscal movement were chosen based on that which produced the most congruent contact in the joint. For the rigid model, SVD was the chosen option. Comparison of scaled Tekscan data and DEA data is shown in Figure 3-7 and Figure 3-8 for fiducially registered models and 3D-2D registered models, respectively. Difference maps were not included for this analysis, as results did not adequately resemble those of the Tekscan readings.

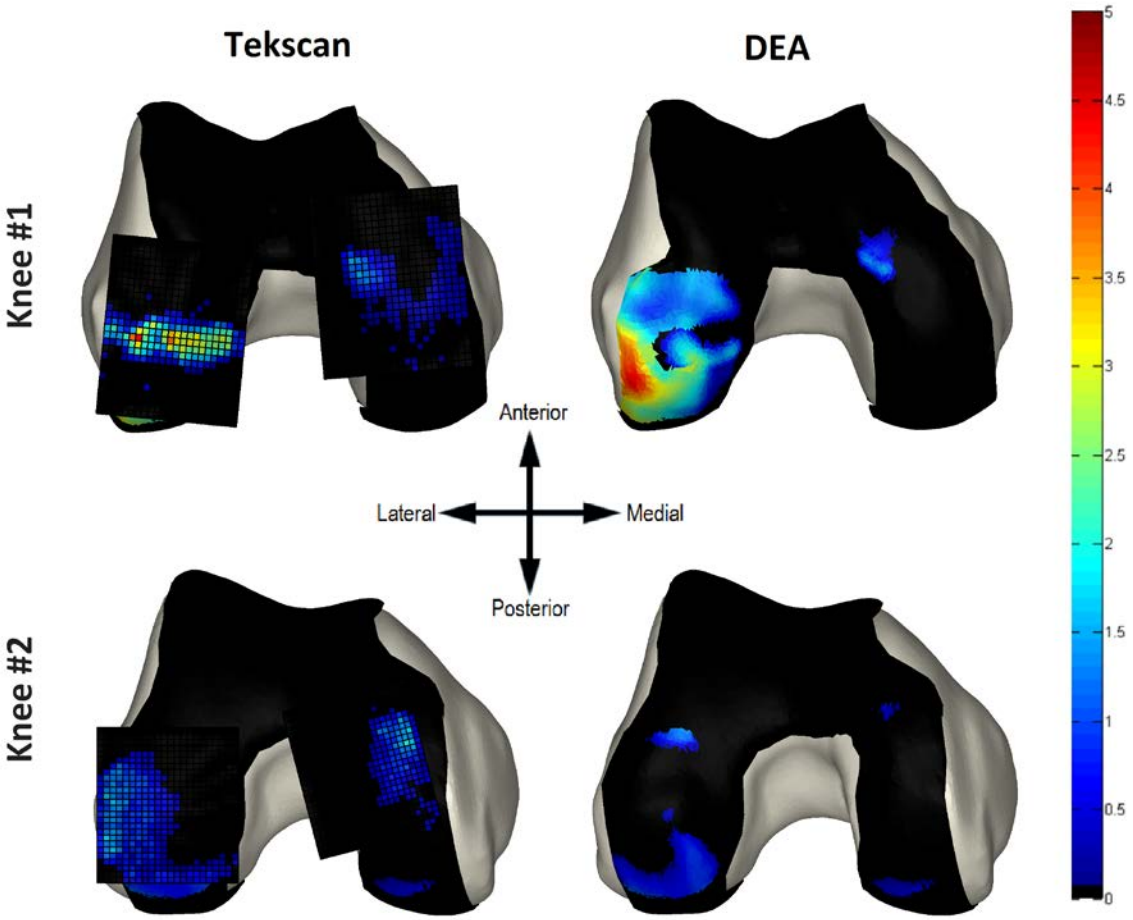

Figure 3-7 – FIDUCIAL REGISTRATION (INTACT MENISCUS): DEA Results displaying the inferior view of the femur. Tekscan pressure results (left) and DEA results (right) are shown for each validation knee.

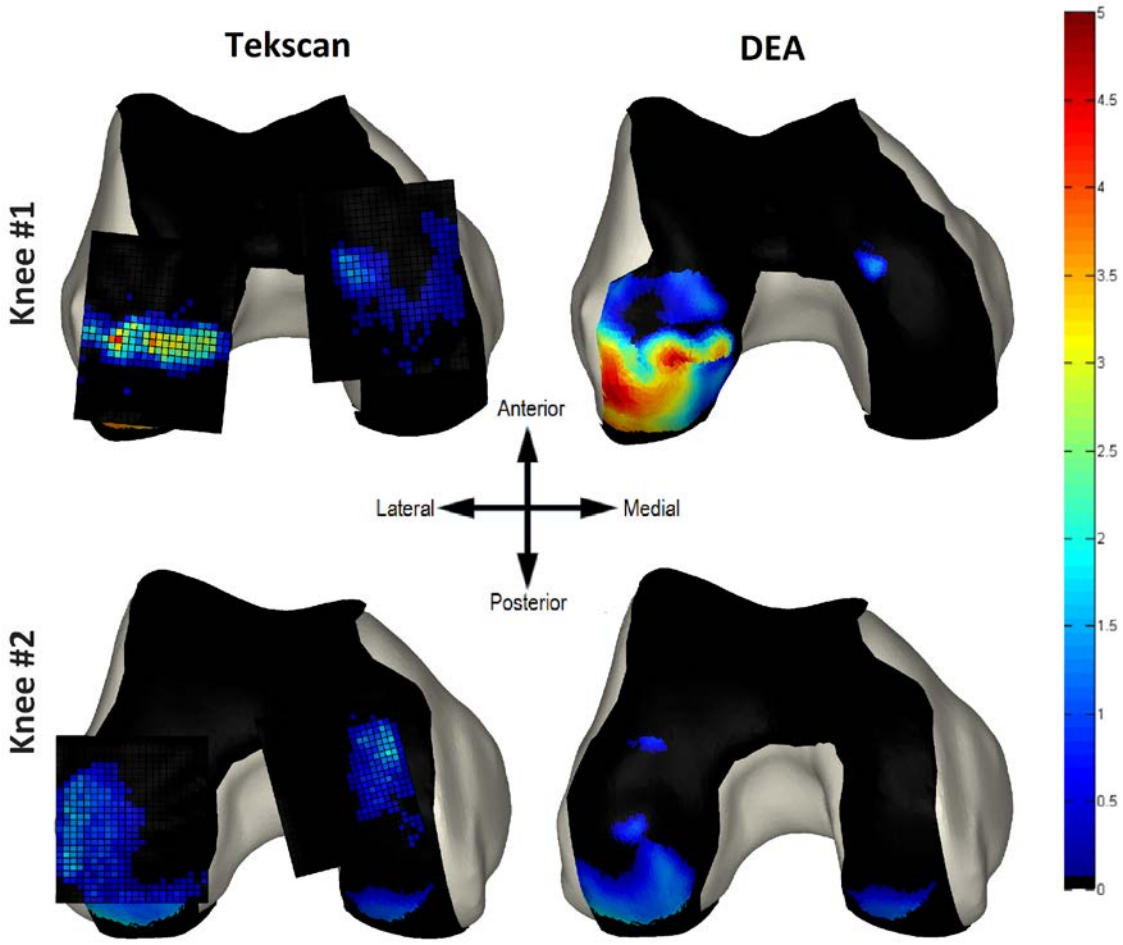

Figure 3-8 – 3D-2D REGISTRATION (INTACT MENISCUS): DEA Results displaying the inferior view of the femur. Tekscan pressure results (left) and DEA results (right) are shown for each validation knee.

Table 3-7 and Table 3-8 provide comparison for stress values and contact areas for the Tekscan and DEA maps displayed previously.

Table 3-7 – INTACT MENISCUS: Mean and peak stress values for Tekscan and DEA maps (two different registration methods).

Contact Stress (MPa)		Lateral Compartment		Medial Compartment	
		Mean	Peak	Mean	Peak
Knee 1	Tekscan	1.43	4.43	0.35	1.50
	DEA (Fiducial)	1.68	4.51	0.69	1.46
	DEA (3D-2D)	2.27	4.78	0.50	1.47
Knee 2	Tekscan	0.71	1.72	0.65	1.93
	DEA (Fiducial)	0.44	1.39	0.21	2.70
	DEA (3D-2D)	0.75	2.00	0.35	1.27

Table 3-8 – INTACT MENISCUS: Contact areas for validation knees from Tekscan and DEA maps using two different types of registration.

Contact Area (mm^2)		Lateral	Medial
Knee 1	Tekscan	245	269
	DEA (Fiducial)	661	54
	DEA (3D-2D)	696	25
Knee 2	Tekscan	416	226
	DEA (Fiducial)	255	59
	DEA (3D-2D)	353	105

Table 3-9 – INTACT MENISCUS: Recovered loads for validation knees from Tekscan and DEA maps using two different types of registration.

Load Recovery (lbs) – Intact meniscus				
	Raw Tekscan	Scaled Tekscan	DEA (Fiducial)	DEA (3D-2D)
Knee 1	54	100	264	328
Knee 2	44	100	24	40

Results for DEA incorporating the meniscus produced values that did not correspond between Tekscan and DEA except for peak stress in Knee 1 (at most an 8% difference from measured). The majority of the data show no relationship between DEA and measured contact, whatsoever. The inability to deform the meniscus model based on tube movement is a likely reason for this. The flatter geometry of the bone and cartilage model in the more extended loaded position contributes to excessive loading being identified along the superior rim of the meniscus. Tube movement shown previously depicts a large amount of anterior translation and radial expansion, resulting in a deformed geometry that was not captured by MRI. Using the undeformed meniscus after moving using SVD puts the meniscus in a "best-fit" location, but SVD is meant for registering two objects with the same shape and fiducial point spacing. As SVD has been deemed the best way to move the meniscus rigidly (using measured tube movements), the results presented above should provide an idea of meniscal DEA using the undeformed meniscus model. Clearly, deformation needs to be accounted for in order to model DEA with an intact meniscus accurately.

Based on these ambiguous meniscal DEA findings, it was proposed to search for an alignment of the superior meniscal surface that produced the closest resemblance to the result observed on Tekscan. This manual measure is obviously not a reasonable method for determining actual meniscal position, but serves to inform further work involving meniscus implementation. Model positioning and results are shown in Figure 3-9 and Figure 3-10.

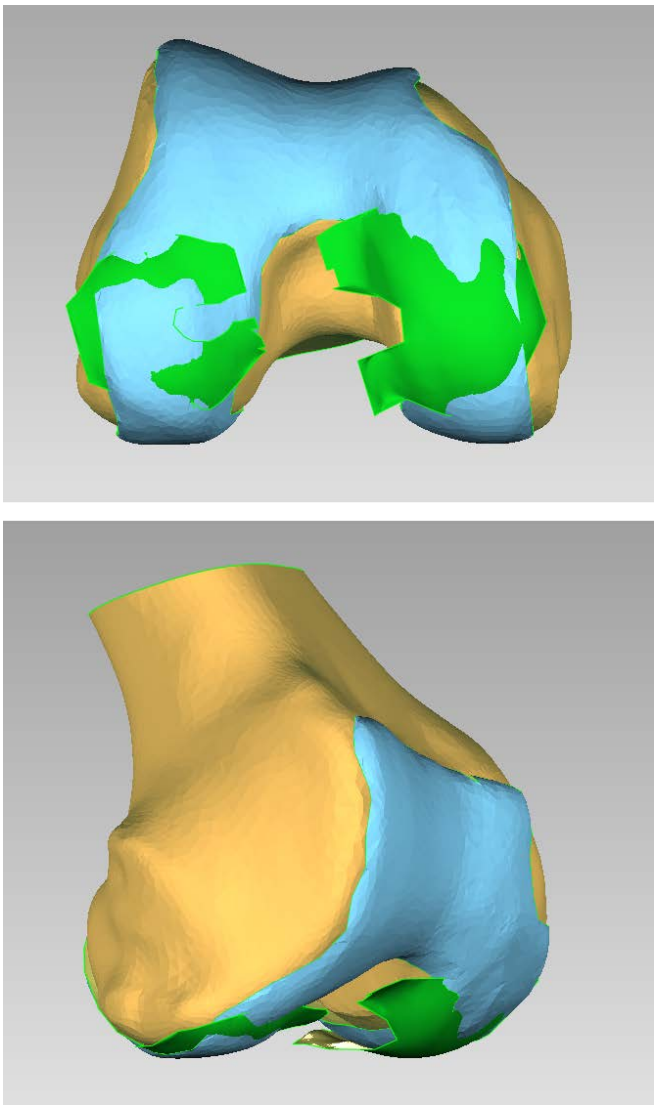

Figure 3-9 – Depiction of amount and locations of overclosure for manually positioned superior meniscus model.

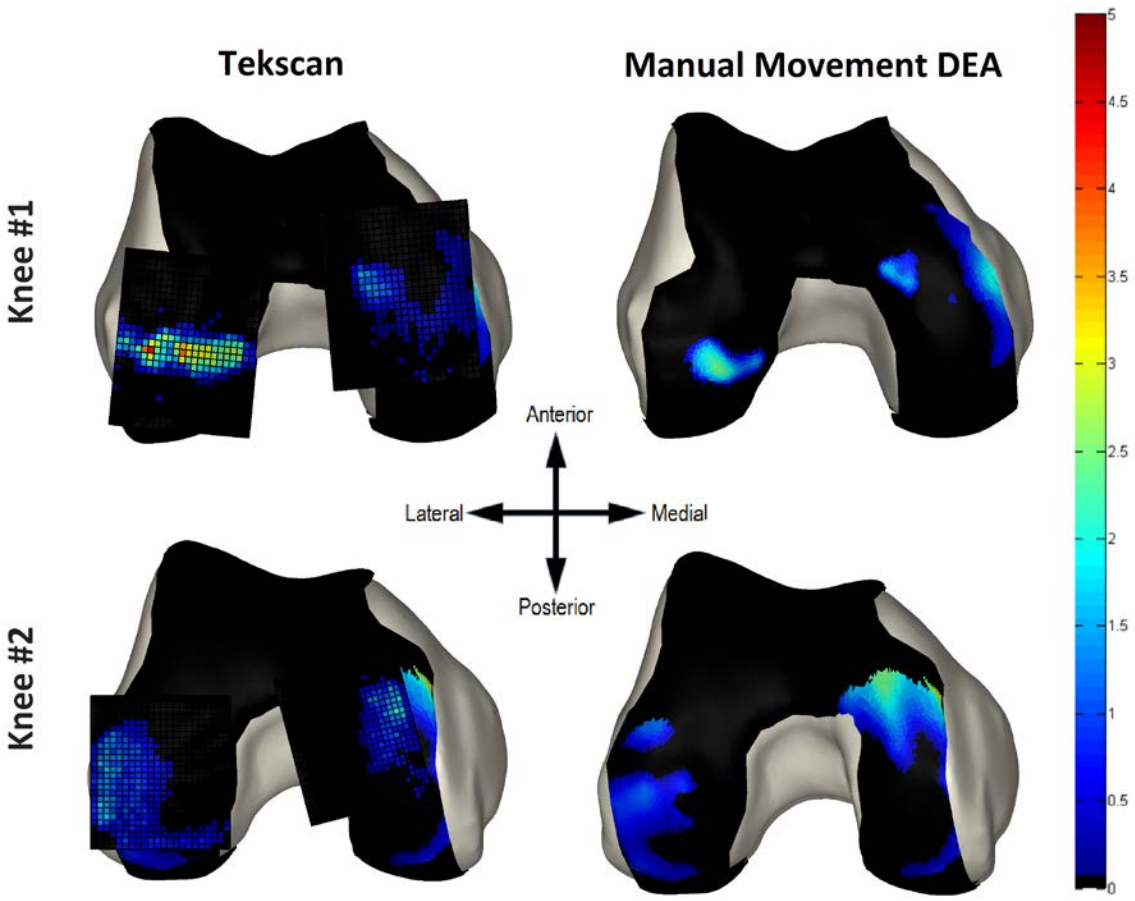

Figure 3-10 – Comparison between intact meniscus Tekscan measurements and DEA using a manually positioned cartilage model.

Table 3-10 – INTACT MENISCUS: Recovered loads for manually positioned meniscal models.

Load Recovery (lbs) – No meniscus		
	Tekscan	Manual Positioning
Knee 1	100	61
Knee 2	100	98

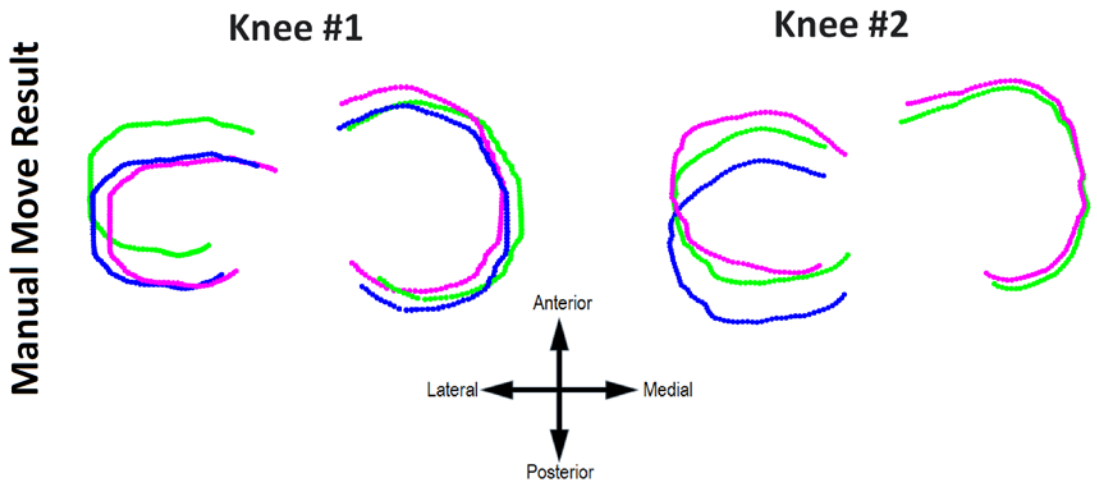

Figure 3-11 – Comparison between no meniscal movement (blue), SVD meniscal movement (magenta), and manual meniscal movement (green).

Qualitatively, manual positioning of the meniscus model had a clear impact on contact shape and location on the femoral cartilage surface. Because the results were obtained in displacement control, there is also cartilage – cartilage contact present (generally the higher stress patches). These results indicate that there is a better, more congruent position for the meniscal model than that provided by SVD, though even these are not perfect representations of meniscal contact in Tekscan. This is not surprising due to the rigid nature of SVD. This position is generally a compromise between SVD and no

movement positions. In Figure 3-11, tube movement using manual manipulation is shown. In the case of the lateral meniscus in Knee #1, the anterior translation shown for manual translation is more than that of SVD. However, contact between the meniscal surface and femoral cartilage is non-existent in this case, meaning a manual movement was not found that improved the DEA result in terms of comparability to the Tekscan readings. Also, the medial meniscal movement of Knee #2 was not required to find DEA results comparable to Tekscan readings, as the resulting position (green) and stating position (blue) differed in no way. However, a systematic method to find this manual position was not apparent during user manipulation. Although the stress maps are in somewhat better agreement than when using other meniscal movement methods, local changes in the curvature of the model are unable to be determined from tube movement. Therefore, the likelihood of obtaining perfectly accurate stress results without a deformed model is minimal.

It was stated previously that the superior rim of the meniscus (via the attached tube) moved the most during the extension of the knee to the loaded position. Though the loading frame was designed to have the same knee flexion angle as the MRI from which the bone models were obtained, substantially less flexion was seen under loading. This would imply that the meniscal model required for more accurate stress estimation would have already undergone substantial deformation. Ideally, to consider a validation complete, one would expect to see fairly comparable load recovery, contact area, and contact location from the modeling method and measured value. This result for manual movement is obviously not perfect, especially because these numbers do not match up for estimated and measured data.

A useful tool in studying contact stresses and areas is the area-engagement histogram. From them, trends can be identified that support related findings. Area-engagement histograms were generated for medial and lateral compartments under a variety of meniscal inclusion/movement parameters. By binning the total contact area

falling within 0.5 MPa intervals, it is easy to examine the distribution of stress in the joint without viewing a stress plot. For example, it can be seen in Figure 3-12 and Figure 3-13 that both of the knees experienced edge loading of the superior rim of the lateral meniscus when no meniscal movement was included in the DEA calculation. Once SVD was implemented, there was a shift in contact area toward lower stress values, as the contact faces were more congruent (or moved out of contact). Also, it appears that Tekscan picks up more far more contact at lower stresses, which in terms of DEA means small amounts of overclosure. This higher sensitivity might be measuring stress between patches of minimal deformation to which DEA is not sensitive.

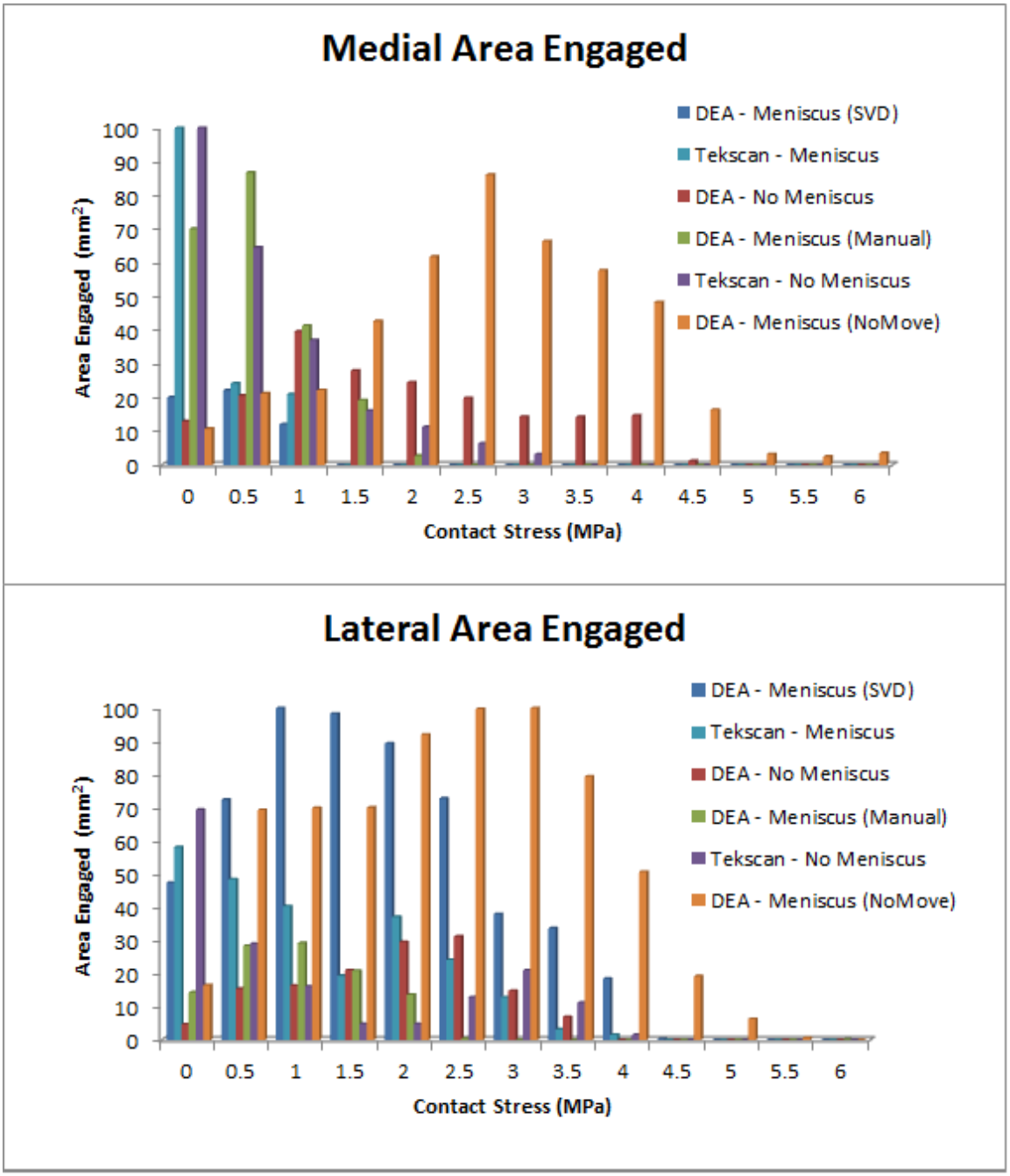

Figure 3-12 – KNEE 1: Area engagement histograms for medial and lateral engagement.

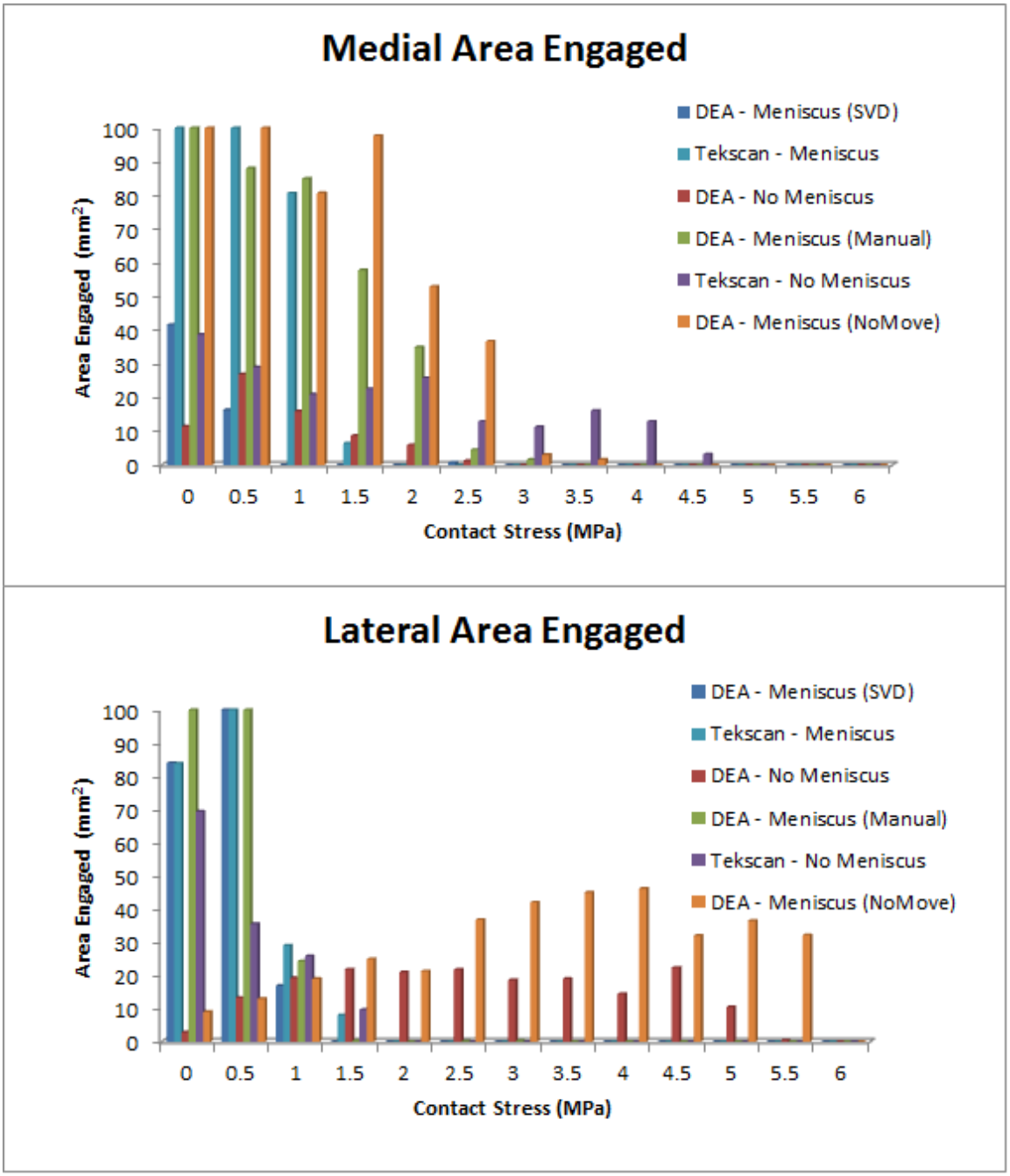

Figure 3-13 – KNEE 2: Area engagement histograms for medial and lateral engagement.

3.3.1 DEA Results – Meniscectomy

DEA results for validation knees with the menisci *removed* are discussed in this section. Run in displacement control for both fiducial and 3D-2D registration methods, this DEA produced very clear contact patches between cartilage surfaces. Tekscan readings are shown in Figure 2-16. Stress values shown are on a 0-5 MPa scale, and represent the readings before scaling of the data took place. Comparisons of scaled Tekscan data and DEA data are shown in Figure 3-14 and Figure 3-15 for fiducially registered models and 3D-2D registered models, respectively.

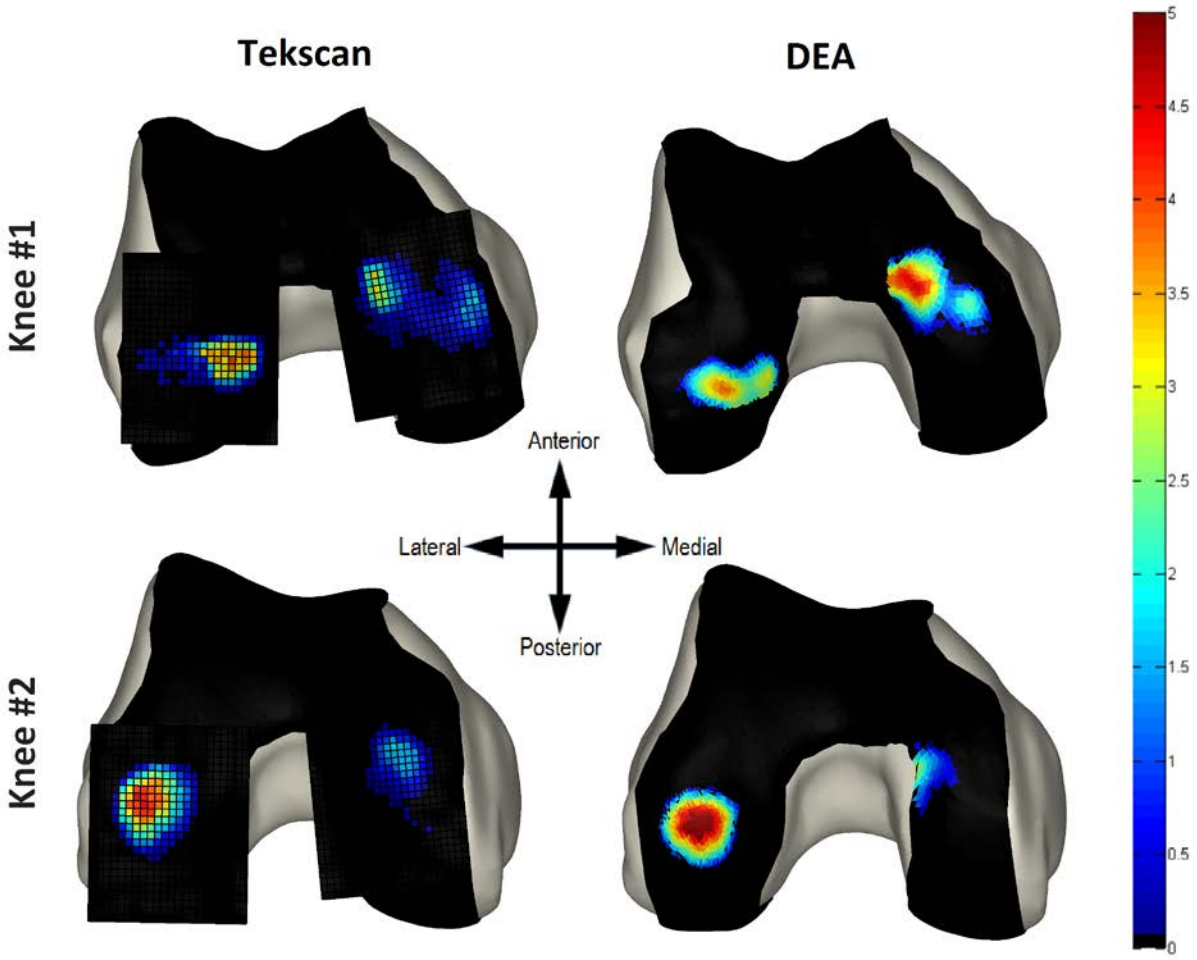

Figure 3-14 – FIDUCIAL REGISTRATION (NO MENISCUS): DEA Results displaying the inferior view of the femur. Tekscan pressure results (left) and DEA results (right) are shown for each validation knee (in MPa).

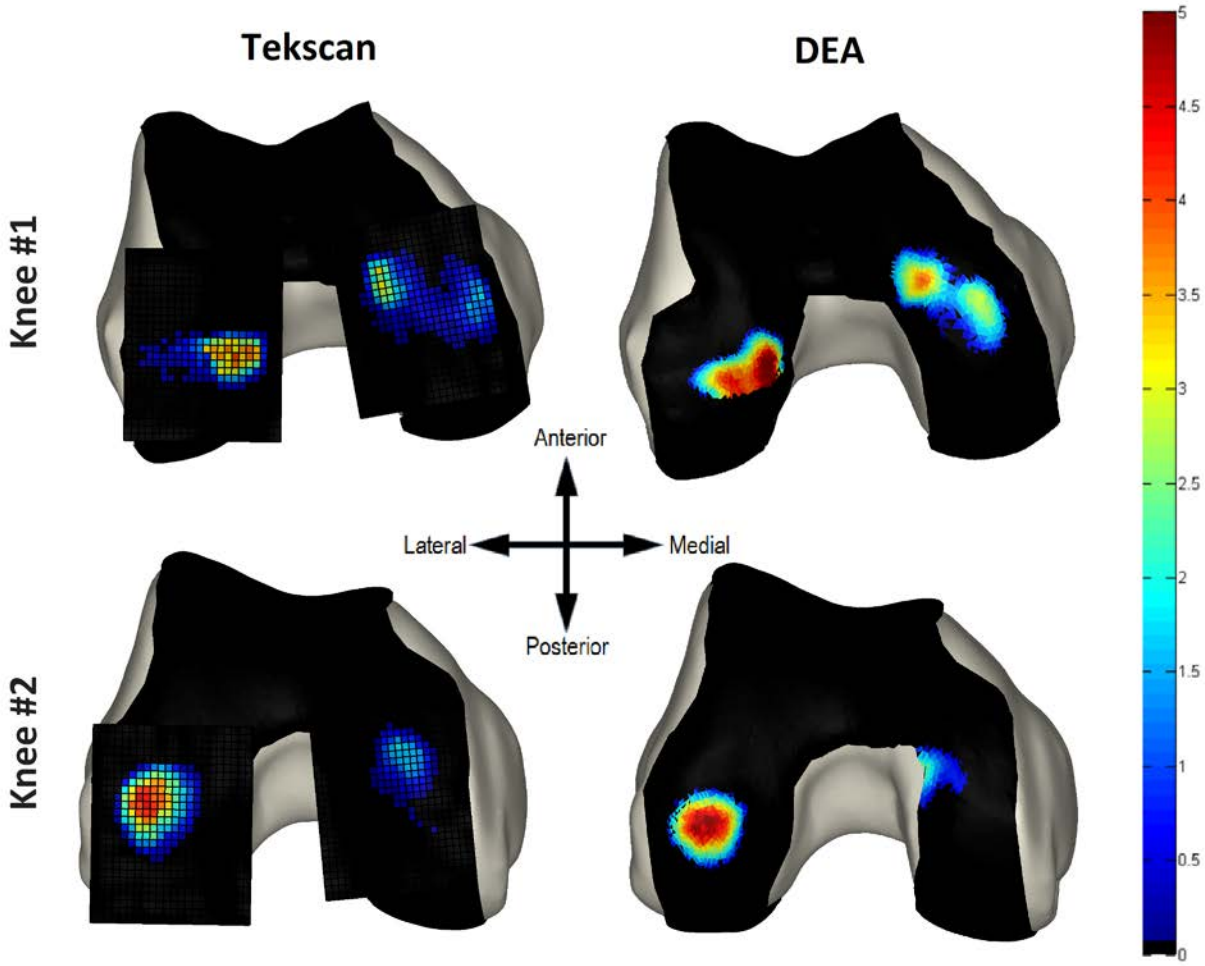

Figure 3-15 – 3D-2D REGISTRATION (NO MENISCUS): DEA Results displaying the inferior view of the femur. Tekscan pressure results (left) and DEA results (right) are shown for each validation knee (in MPa).

Contact patch shapes for both knees look very similar using either registration method, and are also quite similar to Tekscan contact patches based on visual inspection.. Knee 1 experienced the greatest change in contact stress and shape between the two registration methods, indicating that even with such low target registration error reported, slight errors in registration can cause visible changes to contact. However, locations for DEA contact in Knee 1 are very consistent though their stress and shape change slightly. Knee 2 experienced minimal contact change between registration methods, indicating

fairly accurate registrations. More detailed quantification of these results is given in the tables that follow.

Table 3-11 and Table 3-12 provide comparison for stress values and contact areas for the Tekscan and DEA maps displayed previously. Table 3-13 displays results for load recovery in the DEA and Tekscan. The order of Tekscan acquisition was Knee 2, followed by Knee 1, making apparent the degradation in the sensor based on the load being completely on the sensor. Thus, scaling made sense, and DEA values should be compared to it.

Table 3-11 – MENISCECTOMY: Mean and peak stress values for Tekscan and DEA maps (two different registration methods).

Contact Stress (MPa)		Lateral Compartment		Medial Compartment	
		Mean	Peak	Mean	Peak
Knee 1	Tekscan	1.34	4.01	0.70	3.28
	DEA (Fiducial)	2.12	3.88	2.34	4.62
	DEA (3D-2D)	3.02	5.57	1.88	3.92
Knee 2	Tekscan	1.83	4.60	0.65	1.83
	DEA (Fiducial)	3.07	5.55	1.04	2.57
	DEA (3D-2D)	2.90	5.14	0.99	2.53

Table 3-12 – MENISCECTOMY: Contact areas for validation knees from Tekscan and DEA maps using two different types of registration.

Contact Area (mm^2)		Lateral	Medial
Knee 1	Tekscan	171	308
	DEA (Fiducial)	140	190
	DEA (3D-2D)	138	213
Knee 2	Tekscan	193	140
	DEA (Fiducial)	185	70
	DEA (3D-2D)	177	68

Table 3-13 – MENISCECTOMY: Recovered loads for validation knees from Tekscan and DEA maps using two different types of registration.

Load Recovery (lbs) – No meniscus				
	Raw Tekscan	Scaled Tekscan	DEA (Fiducial)	DEA (3D-2D)
Knee 1	61	100	144	163
Knee 2	92	100	112	104

A few trends can be observed when examining the preceding tables. Primarily, prediction of contact stress follows the pattern of over-predicting contact stress in both compartments, resulting in higher mean and peak stresses recorded. Accordingly, this resulted in higher recovered load for DEA maps than for those of Tekscan maps. Contact areas for DEA were also consistently smaller than those for Tekscan, This smaller contact area is to be expected when working with DEA, as recruitment of surrounding facets is by definition not possible unless they too are found to be in contact. In direct relation to this is the fact that smaller contact area will produce higher contact stress if the same force is being placed on the models. In the cadaveric knee, force is likely distributed across the surrounding cartilage as well. The majority of load is also seen in the lateral compartment for both knees. This is counter-intuitive to what might be expected in-vivo,

but may be explained by the assumed “settled” position in the frame being slightly prone to valgus alignment of the bones.

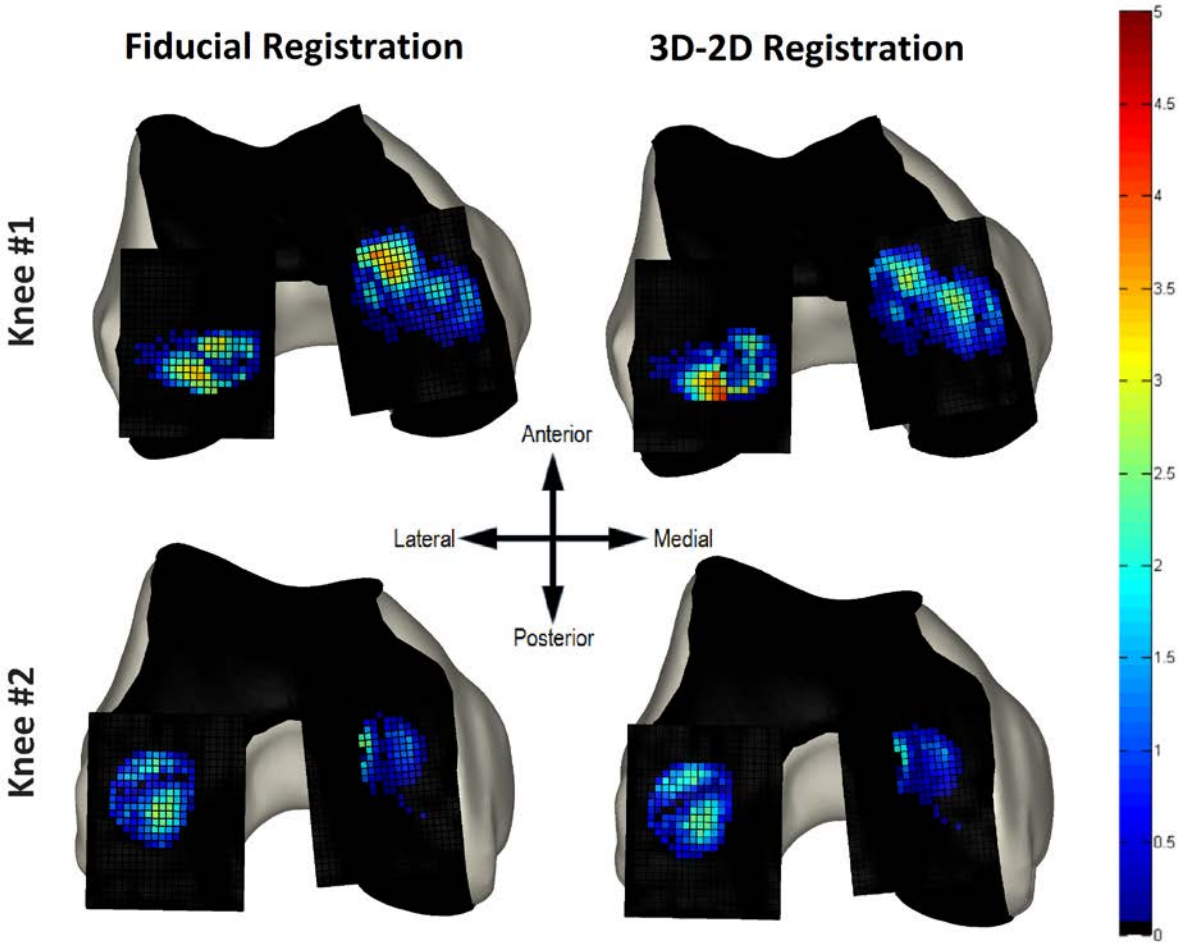

Figure 3-16 – MENISCECTOMY: Absolute difference maps between Tekscan and DEA.

Difference maps between the Tekscan and interpolated DEA grids (Figure 3-16) provide a valuable tool in assessing the accuracy of the DEA algorithm both in contact location and stress levels. Examining the figure, it can be seen that Knee 1 showed the largest discrepancies between estimated and measured values. These locations of higher difference occur throughout the contact patch, but the majority of the difference values

fall below 1.5 MPa. Given DEA's tendency to over-estimate contact stress values, it could be argued that such differences are reasonable. Knee 2 produced much lower difference map values, with most values falling below 1 MPa. As suggested by Anderson, et al., areas of higher difference might be explained by imperfect segmentation of cartilage and bone surfaces, resulting in incorrect cartilage thicknesses or shapes in DEA modeling. Furthermore, it is suggested that insertion of the Tekscan sensor into the joint may disrupt the natural congruity of the cartilage surfaces. [22] Reported fiducial registration errors of around 0.5 mm could also contribute to these higher stresses if error is concentrated in the inferior direction. Lastly, use of a 4 MPa Young's Modulus for cartilage is already a reduced estimate based on lowering of the accepted instantaneous loading modulus. This lowered modulus should better represent the articular cartilage in a state of mechanical equilibrium. Linear scaling of the modulus would scale the DEA results linearly as well, and the true stiffness of cartilage in prolonged knee flexion incorporated by the validation protocol is unknown. To examine the effects of differing Young's modulus for cartilage, the modulus was reduced to 3MPa and 2MPa and DEA was run. These were run using only the fiducial or "gold-standard" registration to demonstrate this point.

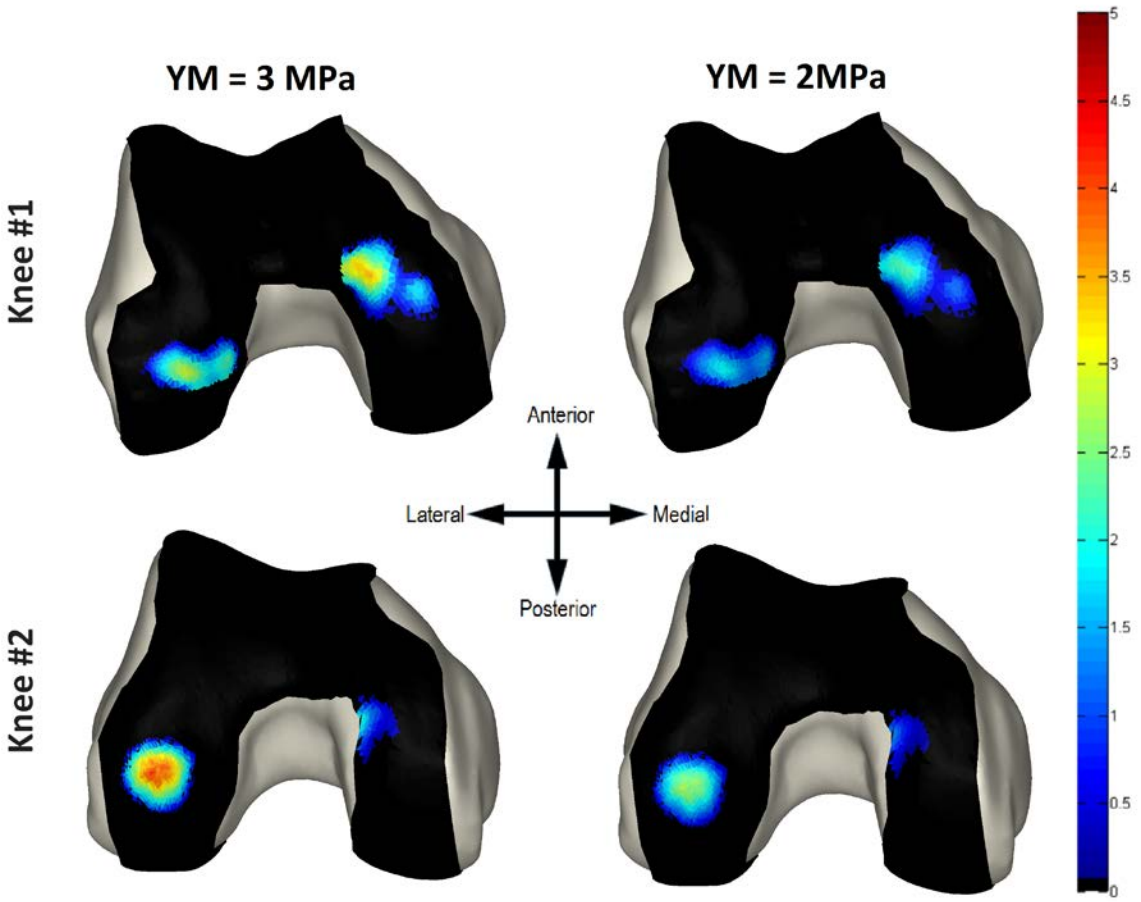

Figure 3-17 – Cartilage stiffness scaling for both validation knees.

Table 3-14 – Cartilage Scaling: Mean and peak stress values for Tekscan and DEA maps (two different registration methods).

Contact Stress (MPa)		Lateral Compartment		Medial Compartment	
		Mean	Peak	Mean	Peak
Knee 1	Tekscan	1.34	4.01	0.70	3.28
	DEA (3MPa)	1.59	2.91	1.76	3.47
	DEA (2MPa)	1.06	1.94	1.17	2.31
Knee 2	Tekscan	1.83	4.60	0.65	1.83
	DEA (3MPa)	2.31	4.17	0.78	1.93
	DEA (2MPa)	1.54	2.78	0.52	1.28

Table 3-15 – Cartilage Scaling: Recovered loads for validation knees from Tekscan and DEA maps using two different types of registration.

Load Recovery (lbs) – No meniscus				
	Raw Tekscan	Scaled Tekscan	DEA (3MPa)	DEA (2MPa)
Knee 1	61	100	115	78
Knee 2	92	100	95	63

Dropping the Young's modulus of cartilage to 3MPa produced even more consistent results between Tekscan and DEA maps. A total of 75% of the mean and peak stress estimations were within 1 MPa of the measured Tekscan values, and the bulk of those were within 0.5 MPa of measured. Based on these results, cartilage under static load for this study could in actuality have a stiffness of ~3MPa rather than 4.

CHAPTER 4: SUMMARY & CONCLUSIONS ON THE VALIDITY DEA METHODS

The benefits to using DEA for stress estimation in the knee are numerous. The knee is the single joint in the body most commonly affected by OA, and elevations in contact stress are implicated in OA development. Registration of subject-specific bone models to functional poses through 2D or 3D weight-bearing imaging modalities provides the joint apposition that is needed to compute contact stress through resulting cartilage model overclosure. Results obtained in this validation study show that registrations of 3D models to 2D slices of a weight-bearing CT scan are accurate within 0.5 mm of a registration obtained using fiducial markers. Varying degrees of registration assistance are needed depending on what artifact-producing items are included in the CT volume (e.g. braces, loading fixtures), but if only the knees are present it is possible to register to only gradients extracted from the CT slice. In this case, manual gradient edge tracings were utilized to the same effect, and produced very accurate 3D-2D registrations. Even sub-millimeter errors for registration can make a difference in knee contact. In Knee 1, the maximum stress computed was in opposite compartments based on which registration was used, and peak values differed by up to 1.5 MPa.

Prior work has validated the DEA formulation in the ankle, lending support to its use in other joints. For the knee more than other joints, limitations exist that must be carefully addressed to produce a useful result. Specifically, contact in a healthy human knee involves a meniscus, whereas most other joints of the body do not. The stability of the knee is almost completely provided by soft tissue surrounding the knee, whereas joints such as the hip have primarily bony stability. Because of the deformable nature and more complex geometry of the meniscus, great care must be exercised when implementing it into the model to accommodate differences in shape and location caused by loading.

It is feasible to measure meniscal movement through the attachment of a silastic tube to the superior rim of the meniscus. This was performed for both validation knees to track meniscal movement from a fully relaxed position to a loaded position. Segmentation of the tubes and subsequent skeletonization of the tube centerlines allowed a point to point analysis of movement. Using SVD, the translations and rotations required to obtain a best-fit to the loaded tube centerline were obtained. The translations were examined on their own to get a general idea for meniscal movement, indicating movement in the anterior and inferior directions. Based on vector plots along the length of the centerlines, some rotation and radial expansion can be seen.

Meniscal DEA can be computed using a rigid model, provided the meniscus does not deform substantially. More specifically, it requires the radius of curvature of the contacting femoral cartilage area to be consistent from segmentation (MRI) to loaded pose (CT). Therefore, the argument for segmenting a deformed meniscus for use in the DEA algorithm can also be made, or simply maintaining a strict methodology to keep knee flexion constant from segmentation pose to loaded pose. This implementation would promote more congruent surface curvatures, but result in altered meniscal material properties. Furthermore, implementation of a deformed meniscus in the DEA model would require the use of load control to compute contact, as a deformed meniscus model as segmented would lie flush with the femoral cartilage and thus produce no overclosure of models to define contact.

DEA results using a meniscal model were produced using the rigid transform produced by SVD, with no correspondence between measured Tekscan values and the estimated DEA values. The need for a deformable meniscus model is clearly apparent based on these results. In order to further explore meniscal movement and deformation and their effect on contact stress for these models, the menisci were manually positioned to obtain similar contact patterns to those of Tekscan readings. The results from this experiment provided much closer matches to Tekscan than SVD movement did, although

not as clearly consistent as contact between cartilage surfaces. The fact that such an alignment is possible to provide a good qualitative assessment, and the load recovered from DEA is 98% of Tekscan loading bodes well for meniscal DEA. If such an alignment exists, the next step is to find a way to reach it in an automated fashion. Local deformations in the meniscus that cannot be captured with anything less than a segmentable weight-bearing image, cannot be taken into account even in a manual alignment method. Modeling of a deformable meniscus has been performed by Guess et al. with reasonable success. Their method for accomplishing this is depicted in Figure 1-13, whereby the meniscus is radially sectioned and allowed to deform based on springs assigned to the shared section boundaries. Using such a method, meniscal movement RMS errors were found to be less than 0.1 mm for both condyles when compared to an FE model of the same knee. Moving forward, methods of this nature should be considered in attempting to accommodate meniscal deformability in DEA models of the knee. Given the recorded accuracy of the Guess model, implementation of this method may be the best option to bring deformability to an otherwise rigid modeling procedure.

After producing DEA results for meniscal contact, the menisci were removed from each knee and Tekscan readings were obtained again. DEA results were far more accurate in predicting the actual contact stress and area seen in Tekscan. In these results, contact area was consistently predicted as slightly lower in DEA and stress was predicted as slightly higher (around 1 MPa). These results were obtained using the same registrations as for the meniscal DEA, ruling out the possibility of initial bone model registration causing meniscal DEA issues.

Overall, it was seen that in knees with no meniscus, contact stress can accurately be predicted based on comparison to live loadings of cadaveric knees, provided the method in which bone models are registered to a loaded apposition is accurate as well. Accuracy of mean and peak stress may be increased if the Young's modulus of cartilage is decreased. Around 3 MPa causes the DEA to recover within 15% of the load that is

applied in the cadaveric setting. This method would work well in knees with no meniscus, but for living human subjects, this will often not be the case. A method for modeling meniscal expansion under loading must be devised and implemented to account for meniscal deformation through the knee's range of motion and under loading. Once this task has been accomplished, *if* it can be accomplished, it is feasible that large-scale subject-specific studies can be conducted to examine contact stress of the human knee. In the future, it is likely that something similar to the Guess model will be implemented to account for meniscal movement and deformation, providing the next crucial piece to modeling knees using DEA. Current studies can make use of the meniscus in DEA, but only in studies where the meniscus underwent minimal shape change between acquisition of MRI for segmentation and acquisition of the functional apposition being studied.

REFERENCES

1. Hootman, J.M. and C.G. Helmick, *Projections of US prevalence of arthritis and associated activity limitations.* Arthritis Rheum, 2006. **54**(1): p. 226-9.

2. Felson, D.T., et al., *Osteoarthritis: new insights. Part 1: the disease and its risk factors.* Ann Intern Med, 2000. **133**(8): p. 635-46.

3. Anderson, D.D., et al., *Post-traumatic osteoarthritis: improved understanding and opportunities for early intervention.* J Orthop Res, 2011. **29**(6): p. 802-9.

4. Sharma, L., et al., *The role of knee alignment in disease progression and functional decline in knee osteoarthritis.* JAMA, 2001. **286**(2): p. 188-95.

5. Flandry, F. and G. Hommel, *Normal anatomy and biomechanics of the knee.* Sports Med Arthrosc, 2011. **19**(2): p. 82-92.

6. Blackburn, T.A. and E. Craig, *Knee anatomy: a brief review.* Phys Ther, 1980. **60**(12): p. 1556-60.

7. Goldblatt, J.P. and J.C. Richmond, *Anatomy and biomechanics of the knee.* Operative Techniques in Sports Medicine, 2003. **11**(3): p. 172-186.

8. Hunter, D.J., et al., *Increase in bone marrow lesions associated with cartilage loss - A longitudinal magnetic resonance imaging study of knee osteoarthritis.* Arthritis and Rheumatism, 2006. **54**(5): p. 1529-1535.

9. Segal, N.A., et al., *Elevated tibiofemoral articular contact stress predicts risk for bone marrow lesions and cartilage damage at 30 months.* Osteoarthritis Cartilage, 2012. **20**(10): p. 1120-6.

10. Felson, D.T., et al., *The association of bone marrow lesions with pain in knee osteoarthritis.* Annals of Internal Medicine, 2001. **134**(7): p. 541-549.

11. Cotofana, S., et al., *Cartilage thickening in early radiographic knee osteoarthritis: a within-person, between-knee comparison.* Arthritis Care Res (Hoboken), 2012. **64**(11): p. 1681-90.

12. Yamada, K., et al., *Subchondral bone of the human knee joint in aging and osteoarthritis.* Osteoarthritis Cartilage, 2002. **10**(5): p. 360-9.

13. Sharma, L., *The role of varus and valgus alignment in knee osteoarthritis.* Arthritis Rheum, 2007. **56**(4): p. 1044-7.

14. Neogi, T., et al., *Magnetic Resonance Imaging-Based Three-Dimensional Bone Shape of the Knee Predicts Onset of Knee Osteoarthritis: Data From the Osteoarthritis Initiative.* Arthritis and Rheumatism, 2013. **65**(8): p. 2048-2058.

15. Nagura, T., et al., *Tibiofemoral joint contact force in deep knee flexion and its consideration in knee osteoarthritis and joint replacement.* Journal of Applied Biomechanics, 2006. **22**(4): p. 305-313.

16. Perry, J., D. Antonelli, and W. Ford, *Analysis of knee-joint forces during flexed-knee stance.* J Bone Joint Surg Am, 1975. **57**(7): p. 961-7.

17. Brown, T.D. and D.T. Shaw, *In vitro contact stress distribution on the femoral condyles.* J Orthop Res, 1984. **2**(2): p. 190-9.

18. Segal, N.A., et al., *Baseline articular contact stress levels predict incident symptomatic knee osteoarthritis development in the MOST cohort.* J Orthop Res, 2009. **27**(12): p. 1562-8.

19. Huiskes, R. and E.Y. Chao, *A survey of finite element analysis in orthopedic biomechanics: the first decade.* J Biomech, 1983. **16**(6): p. 385-409.

20. Brekelmans, W.A., H.W. Poort, and T.J. Slooff, *A new method to analyse the mechanical behaviour of skeletal parts.* Acta Orthop Scand, 1972. **43**(5): p. 301-17.

21. Anderson, D.D., et al., *Intra-articular contact stress distributions at the ankle throughout stance phase-patient-specific finite element analysis as a metric of degeneration propensity.* Biomech Model Mechanobiol, 2006. **5**(2-3): p. 82-9.

22. Anderson, D.D., et al., *Physical validation of a patient-specific contact finite element model of the ankle.* J Biomech, 2007. **40**(8): p. 1662-9.

23. Li, G., et al., *A validated three-dimensional computational model of a human knee joint.* J Biomech Eng, 1999. **121**(6): p. 657-62.

24. Grosland, N.M., et al., *IA-FEMesh: an open-source, interactive, multiblock approach to anatomic finite element model development.* Comput Methods Programs Biomed, 2009. **94**(1): p. 96-107.

25. Anderson, D.D., et al., *A dynamic finite element analysis of impulsive loading of the extension-splinted rabbit knee.* J Biomech Eng, 1990. **112**(2): p. 119-28.

26. Chao, E.Y., et al., *Discrete element analysis in musculoskeletal biomechanics.* Mol Cell Biomech, 2010. **7**(3): p. 175-92.

27. Schuind, F., et al., *Force and pressure transmission through the normal wrist. A theoretical two-dimensional study in the posteroanterior plane.* J Biomech, 1995. **28**(5): p. 587-601.

28. Elias, J.J., et al., *Evaluation of a computational model used to predict the patellofemoral contact pressure distribution.* J Biomech, 2004. **37**(3): p. 295-302.

29. Kwak, S.D., L. Blankevoort, and G.A. Ateshian, *A Mathematical Formulation for 3D Quasi-Static Multibody Models of Diarthrodial Joints.* Comput Methods Biomech Biomed Engin, 2000. **3**(1): p. 41-64.

30. Li, G., M. Sakamoto, and E.Y. Chao, *A comparison of different methods in predicting static pressure distribution in articulating joints.* J Biomech, 1997. **30**(6): p. 635-8.

31. Blankevoort, L., et al., *Articular contact in a three-dimensional model of the knee.* J Biomech, 1991. **24**(11): p. 1019-31.

32. Huiskes, R., et al., *Analytical stereophotogrammetric determination of three-dimensional knee-joint geometry.* J Biomech, 1985. **18**(8): p. 559-70.

33. Lobo-Guerrero, S., Vallejo, L., *Discrete Element Method Evaluation of Granular Crushing Under Direct Shear Test Conditions.* Journal of Geotechnical and Geoenvironmental Engineering. **131**(10).

34. Kern, A.M., *Large population evaluation of contact stress exposure in articular joints for prediction of osteoarthritis onset and progression.* University of Iowa, 2011.

35. Rosset, A., L. Spadola, and O. Ratib, *OsiriX: an open-source software for navigating in multidimensional DICOM images.* J Digit Imaging, 2004. **17**(3): p. 205-16.

36. Moro-Oka, T., et al., *Can magnetic resonance imaging-derived bone models be used for accurate motion measurement with single-plane three-dimensional shape registration?* Journal of Orthopaedic Research, 2007. **25**(7): p. 867-872.

37. McWalter, E.J., et al., *Use of novel interactive input devices for segmentation of articular cartilage from magnetic resonance images.* Osteoarthritis and Cartilage, 2005. **13**(1): p. 48-53.

38. Kothari, M., et al., *Fixed-flexion radiography of the knee provides reproducible joint space width measurements in osteoarthritis.* Eur Radiol, 2004. **14**(9): p. 1568-73.

39. Fregly, B.J., H.A. Rahman, and S.A. Banks, *Theoretical accuracy of model-based shape matching for measuring natural knee kinematics with single-plane fluoroscopy.* J Biomech Eng, 2005. **127**(4): p. 692-9.

40. Banks, S.A. and W.A. Hodge, *Accurate measurement of three-dimensional knee replacement kinematics using single-plane fluoroscopy.* Ieee Transactions on Biomedical Engineering, 1996. **43**(6): p. 638-649.

41. Canny, J., *A computational approach to edge detection.* IEEE Trans Pattern Anal Mach Intell, 1986. **8**(6): p. 679-98.

42. Markelj, P., et al., *A review of 3D/2D registration methods for image-guided interventions.* Med Image Anal, 2012. **16**(3): p. 642-61.

43. Markelj, P., et al., *Robust gradient-based 3-D/2-D registration of CT and MR to X-ray images.* IEEE Trans Med Imaging, 2008. **27**(12): p. 1704-14.

44. Grood, E.S. and W.J. Suntay, *A joint coordinate system for the clinical description of three-dimensional motions: application to the knee.* J Biomech Eng, 1983. **105**(2): p. 136-44.

45. Anderson, D.D., et al., *Reliability of semiautomated computational methods for estimating tibiofemoral contact stress in the Multicenter Osteoarthritis Study.* Comput Math Methods Med, 2012. **2012**: p. 767469.

46. Mao, W., et al., *CT image registration in sinogram space.* Med Phys, 2007. **34**(9): p. 3596-602.

47. Barker, M.K. and B.B. Seedhom, *The relationship of the compressive modulus of articular cartilage with its deformation response to cyclic loading: does cartilage optimize its modulus so as to minimize the strains arising in it due to the prevalent loading regime?* Rheumatology (Oxford), 2001. **40**(3): p. 274-84.

48. Jin, H. and J.L. Lewis, *Determination of Poisson's ratio of articular cartilage by indentation using different-sized indenters.* J Biomech Eng, 2004. **126**(2): p. 138-45.

49. Friedman, J.H., F. Baskett, and L.J. Shustek, *Algorithm for Finding Nearest Neighbors.* Ieee Transactions on Computers, 1975. **24**(10): p. 1000-1006.

50. Kremmer, M. and J.F. Favier, *A method for representing boundaries in discrete element modelling - part I: Geometry and contact detection.* International Journal for Numerical Methods in Engineering, 2001. **51**(12): p. 1407-1421.

51. Pandy, M.G., K. Sasaki, and S. Kim, *A Three-Dimensional Musculoskeletal Model of the Human Knee Joint. Part 1: Theoretical Construct.* Comput Methods Biomech Biomed Engin, 1998. **1**(2): p. 87-108.

52. Williams, J.R. and R. O'Connor, *Discrete element simulation and the contact problem.* Archives of Computational Methods in Engineering, 1999. **6**(4): p. 279-304.

53. Bei, Y. and B.J. Fregly, *Multibody dynamic simulation of knee contact mechanics.* Med Eng Phys, 2004. **26**(9): p. 777-89.

54. Anderson, D.D., et al., *Implementation of discrete element analysis for subject-specific, population-wide investigations of habitual contact stress exposure.* J Appl Biomech, 2010. **26**(2): p. 215-23.

55. Boyse, J.W., *Interference Detection among Solids and Surfaces.* Communications of the Acm, 1979. **22**(1): p. 3-9.

56. Fitzpatrick, C.K., M.A. Baldwin, and P.J. Rullkoetter, *Computationally efficient finite element evaluation of natural patellofemoral mechanics.* J Biomech Eng, 2010. **132**(12): p. 121013.

57. Fregly, B.J., et al., *Sensitivity of knee replacement contact calculations to kinematic measurement errors.* J Orthop Res, 2008. **26**(9): p. 1173-9.

58. Leach, R.E., T. Gregg, and F.J. Siber, *Weight-bearing radiography in osteoarthritis of the knee.* Radiology, 1970. **97**(2): p. 265-8.

59. Lazennec, J.Y., et al., *Pelvis and total hip arthroplasty acetabular component orientations in sitting and standing positions: measurements reproductibility with EOS imaging system versus conventional radiographies.* Orthop Traumatol Surg Res, 2011. **97**(4): p. 373-80.

60. Karrholm, J., S. Brandsson, and M.A. Freeman, *Tibiofemoral movement 4: changes of axial tibial rotation caused by forced rotation at the weight-bearing knee studied by RSA.* J Bone Joint Surg Br, 2000. **82**(8): p. 1201-3.

61. Patel, V.V., et al., *Magnetic resonance imaging of patellofemoral kinematics with weight-bearing.* J Bone Joint Surg Am, 2003. **85-A**(12): p. 2419-24.

62. Powers, C.M., et al., *Patellofemoral kinematics during weight-bearing and non-weight-bearing knee extension in persons with lateral subluxation of the patella: a preliminary study.* J Orthop Sports Phys Ther, 2003. **33**(11): p. 677-85.

63. Gold, G.E., et al., *Weight-bearing MRI of patellofemoral joint cartilage contact area.* J Magn Reson Imaging, 2004. **20**(3): p. 526-30.

64. Shapiro, L.M. and G.E. Gold, *MRI of weight bearing and movement.* Osteoarthritis Cartilage, 2012. **20**(2): p. 69-78.

65. Johal, P., et al., *Tibio-femoral movement in the living knee. A study of weight bearing and non-weight bearing knee kinematics using 'interventional' MRI.* J Biomech, 2005. **38**(2): p. 269-76.

66. Jinkins, J.R., J.S. Dworkin, and R.V. Damadian, *Upright, weight-bearing, dynamic-kinetic MRI of the spine: initial results.* Eur Radiol, 2005. **15**(9): p. 1815-25.

67. Souza, R.B., et al., *Femur rotation and patellofemoral joint kinematics: a weight-bearing magnetic resonance imaging analysis.* J Orthop Sports Phys Ther, 2010. **40**(5): p. 277-85.

68. Hill, P.F., et al., *Tibiofemoral movement 2: the loaded and unloaded living knee studied by MRI.* J Bone Joint Surg Br, 2000. **82**(8): p. 1196-8.

69. Anderson, I.A., et al., *A novel method for measuring medial compartment pressures within the knee joint in-vivo.* J Biomech, 2003. **36**(9): p. 1391-5.

70. Afoke, N.Y., P.D. Byers, and W.C. Hutton, *Contact pressures in the human hip joint.* J Bone Joint Surg Br, 1987. **69**(4): p. 536-41.

71. Akbar, M., et al., *A detailed and validated three dimensional dynamic model of the patellofemoral joint.* J Biomech Eng, 2012. **134**(4): p. 041005.

72. Pena, E., et al., *A three-dimensional finite element analysis of the combined behavior of ligaments and menisci in the healthy human knee joint.* J Biomech, 2006. **39**(9): p. 1686-701.

73. Pena, E., et al., *Finite element analysis of the effect of meniscal tears and meniscectomies on human knee biomechanics.* Clin Biomech (Bristol, Avon), 2005. **20**(5): p. 498-507.

74. Li, Z., et al., *Three-dimensional finite element models of the human pubic symphysis with viscohyperelastic soft tissues.* Ann Biomed Eng, 2006. **34**(9): p. 1452-62.

75. Guess, T.M., et al., *A subject specific multibody model of the knee with menisci.* Med Eng Phys, 2010. **32**(5): p. 505-15.

76. Vedi, V., et al., *Meniscal movement. An in-vivo study using dynamic MRI.* J Bone Joint Surg Br, 1999. **81**(1): p. 37-41.

77. Thompson, W.O., et al., *Tibial meniscal dynamics using three-dimensional reconstruction of magnetic resonance images.* Am J Sports Med, 1991. **19**(3): p. 210-5; discussion 215-6.

78. Donahue, T.L., et al., *A finite element model of the human knee joint for the study of tibio-femoral contact.* J Biomech Eng, 2002. **124**(3): p. 273-80.

79. Hartmann, J.M., et al., *Compliance-dependent load allocation between sensing versus non-sensing portions of a sheet-array contact stress sensor.* Iowa Orthop J, 2009. **29**: p. 43-7.

80. Sharma, G., Kuntze, G.,Held, N.,Ronsky, J., *A Dual Fluoroscopy Approach For Quantifying Minimal Detectable 3D Tibiofemoral Displacement: Relevance For In-Vivo Soft Tissue Deformation Assessment.* ORS Abstract, 2014(Poster # 0798).

81. Klema, V.C. and A.J. Laub, *The Singular Value Decomposition - Its Computation and Some Applications.* Ieee Transactions on Automatic Control, 1980. **25**(2): p. 164-176.

82. Van Uitert, R. and I. Bitter, *Subvoxel precise skeletons of volumetric data based on fast marching methods.* Med Phys, 2007. **34**(2): p. 627-38.

83. Zielinska, B. and T.L. Donahue, *3D finite element model of meniscectomy: changes in joint contact behavior.* J Biomech Eng, 2006. **128**(1): p. 115-23.

84. Danilchenko, A. and J.M. Fitzpatrick, *General approach to first-order error prediction in rigid point registration.* IEEE Trans Med Imaging, 2011. **30**(3): p. 679-93.

85. Fitzpatrick, J.M. and J.B. West, *The distribution of target registration error in rigid-body point-based registration.* IEEE Trans Med Imaging, 2001. **20**(9): p. 917-27.

86. Fitzpatrick, J.M., J.B. West, and C.R. Maurer, Jr., *Predicting error in rigid-body point-based registration.* IEEE Trans Med Imaging, 1998. **17**(5): p. 694-702.

87. Pawiro, S.A., et al., *Validation for 2D/3D registration. I: A new gold standard data set.* Med Phys, 2011. **38**(3): p. 1481-90.